SANDIA REPORT

SAND98–2628
Unlimited Release
Printed December 1998

Inversion of Passive Electromagnetic Fields to Locate Weapons of Mass Destruction

Gregory A. Newman and David M. Day

Prepared by
Sandia National Laboratories
Albuquerque, New Mexico 87185 and Livermore, California 94550

Sandia is a multiprogram laboratory operated by Sandia Corporation, a Lockheed Martin Company, for the United States Department of Energy under Contract DE-AC04-94AL85000.

Sandia National Laboratories

Issued by Sandia National Laboratories, operated for the United States Department of Energy by Sandia Corporation.

Available to DOE and DOE contractors from
Office of Scientific and Technical Information
P.O. Box 62
Oak Ridge, TN 37831

Prices available from (615) 576-8401, FTS 626-8401

Available to the public from
National Technical Information Service
U.S. Department of Commerce
5285 Port Royal Rd
Springfield, VA 22161

NTIS price codes
Printed copy: A04
Microfiche copy: A01

SAND98-2628
Unlimited Release
Printed December 1998

INVERSION OF PASSIVE ELECTROMAGNETIC FIELDS TO LOCATE WEAPONS OF MASS DESTRUCTION

Gregory A. Newman
Geophysical Technology Department

David M. Day
Applied Mathematics Department

Sandia National Laboratories
P.O. Box 5800
Albuquerque, NM 87185-0750

Abstract

A resolution study, employing a 3D nonlinear optimization technique, has been undertaken to study the viability of magnetotelluric (MT) measurements to detect and characterize buried facilities that make weapons of mass destruction. A significant advantage of the MT method is that no active source is required because the method employs passive field emissions. Thus measurements can be carried out covertly. Findings indicate it is possible to image WMD facilities, including depth of burial and lateral extent if a sufficient number of measurements are taken on the perimeter of the facility. Moreover if a station measurement can be made directly over the facility then the resolution is improved accordingly. In all cases it was not possible to image the base of the facility with any confidence as well as provide any precise inferences on the facility electrical conductivity. This later finding, however, is really not that critical since knowledge of facility geometry is far more important than knowledge of its conductivity. For the WMD problem it is recommended that MT measurements be made solely with the magnetic field ratios. In this context it would then be possible to deploy with far greater ease small coils about a suspected facility and would allow for the measurements to be conducted in a more covert manner. Before testing such a measurement system in the field, however, it would be necessary to carry out a similar resolution analysis as was done with MT measurements based on electric and magnetic fields. This is necessary to determine sensitivity of the proposed measurement to underground facilities along with needed data coverage and quality. Such a study is indispensable in producing useful reconstructions of underground facilities.

INTRODUCTION

Weapons of mass destruction (WMD) pose grave threats to the security of the United States and the rest of the free world. Identifying and locating these facilities are therefore of great importance. Because many facilities are buried at depths greater than several 10's of meters, remote sensing methods may be necessary for their detection. Here we focus on very low frequency (VLF) electromagnetic fields (<10kHz) to detect, locate and characterize WMD facilities. The use of VLF fields is required since the earth is a high loss medium, and higher frequency fields such as synthetic aperture radar cannot effectively penetrate to the required depths. While passive seismic monitoring methods are currently under investigation for the WMD problem, the use of VLF fields are also now receiving attention, as evidenced by this report.

Two types of VLF passive measurements are most promising for detecting WMD facilities. The first, which this report address, uses natural VLF emissions or magnetotelluric (MT) fields that arise from interaction of the solar wind with the earth's ionosphere. The second employs emissions from powerlines directly feeding the facility.

A major obstacle in employing passive VLF fields to image WMD facilities has been the inability to interpret data. The observed VLF field depends on both the facility and local geology. To accurately locate and characterize the facility we must also characterize the geology. Unfortunately, the facility response is coupled to the geology in a nonlinear fashion and the geology and topography, of WMD sites is often complex and rugged. The minimal amount of data sufficient to reliably characterize and locate WMD facilities is also unknown. Data sets with high spatial sampling are desirable, but not practical to collect.

To resolve these questions we have carried out a resolution study, employing a nonlinear inversion technique designed for MT fields. We define inversion as a mathematical process to find the electrical conductivity model of the earth that fits the measurements to within observational errors. The model yields estimates on facility location and geometry as well as site geology. More importantly, the inversion process, quantifies the uncertainties of these estimates in terms of the observational error levels and data coverage at the site. While the inversion methodology is designed to analyze field data, it is better first to determine the method's potential through a resolution study, before proceeding with the analysis of actual field measurements arising from suspected WMD facilities.

A significant advantage of using MT data to characterize WMD facilities is that no active source is required to generate the fields. Since the method employs passive field emissions, measurements can be carried out covertly. An important obstacle that has limited the applicability of the method to the WMD problem, however, has been the lack of 3D inversion schemes capable of simultaneously resolving both the facility and complex geology. Only in the last few years have full solutions to the 3D MT inverse problem have started to emerge (cf. Newman and Alumbaugh, 1998; Madden and Mackie, 1993). In this report we will use the Newman and Alumbaugh (1998) scheme to provide some critical experiment design information that would be needed to detect, locate and characterize WMD facilities. Since the details of this scheme are not yet available in the published literature (the work is currently submitted for publication) we will first present its theoretical basis before proceeding with the resolution analysis of the

WMD problem. Also included in this report (Appendices C and D) is a new preconditioning technique that we have developed to reduce computation time needed in the 3D MT forward problem. The forward problem is needed to compute predicted responses and functional gradients for the inverse problem. Because of time constraints we could not full implement these procedures in this report.

OVERVIEW OF THE MT METHOD

To help ease the reader into the more difficult technical aspects of the report we shall first give a brief review of the MT method. In the magnetotelluric method, the quantities that are measured are horizontal electric and magnetic fields and sometimes the vertical magnetic field, (Figure. 1). Because these fields are time series resulting from pulsation of the earth's magnetosphere, several pre-processing steps are necessary before inferences can be made about the subsurface conductivity. The first is to Fourier transform the time series into the frequency domain and form field ratios to eliminate the unknown source characteristics. These ratios are often referred to impedances and are the data type used in the analysis of MT fields. A good overview of the MT method can be found in the monograph of Vozoff (1986) which contains numerous papers on different aspects of method. More recent developments in the method can be found in the current geophysical literature.

THE 3D MAGNETOTELLURIC FORWARD PROBLEM

An important consideration in solving the 3D MT inverse problem is that the forward-modeling solution simulate responses arising from realistic 3D geology. Hundreds of thousands of cells are required for these types of numerical simulations and finite difference modeling techniques are very efficient for the task and will be employed here.

Assuming a time harmonic dependence of $e^{i\omega t}$ where $i=\sqrt{-1}$, a vector equation for the electric field is written as

$$\nabla \times \mu_o/\mu \nabla \times \mathbf{E} + i\omega\mu_o\sigma \mathbf{E} = \mathbf{S}. \qquad (1)$$

In this expression the electrical conductivity and magnetic permeability are denoted by σ and μ respectively, where μ_o is the magnetic permeability of free space. Specification of the source vector **S**, which includes the appropriate Dirichlet boundary conditions, defines the source field polarization. To simulate natural fields, **S** is set to zero everywhere, except at points where tangential electric-field boundary values are specified. These boundary values arise from plane waves propagating in layered or 2D geologic media assigned at the boundaries of the 3D problem.

When equation (1) is approximated with finite differences using a Yee (1966) staggered grid (Figure 2) and symmetrically scaled (cf., Newman & Alumbaugh, 1995; Alumbaugh et al., 1996), a linear system results where,

$$\mathbf{K}\,\mathbf{E} = \mathbf{S}'. \qquad (2)$$

The matrix $\mathbf{K}$ is complex-symmetric and sparse with 13 non-zero entries per row and $\mathbf{S}'$ is a scaled representation of $\mathbf{S}$. This system can be efficiently solved using the quasi minimum residual (qmr) method, which belongs to the class of Krylov sub-space techniques that are highly efficient in iteratively solving sparse linear systems. The reader is referred to Newman & Alumbaugh (1995) and Alumbaugh et al. (1996) for the details on how the solver is implemented. Once the electric fields are determined, the magnetic fields can be determined from Faraday's law by numerically approximating the curl of the electric field at various nodal points and interpolating either the electric or magnetic field nodal values to the point of interest.

Even with the benefits of a staggered grid, which implicitly enforces the auxiliary divergence condition on the on the fields, it is often necessary to explicitly enforce these conditions, where

$$\nabla \cdot \sigma \mathbf{E} = \mathbf{0} \tag{3}$$

and

$$\nabla \cdot \mathbf{E} = \mathbf{0} \tag{4}$$

in the earth and air respectively. This is accomplished in the numerical solution through a static-divergence correction as frequencies approach the static limit. This correction, developed by Smith (1996), can drastically reduce the time needed to solve equation (2). It is implemented by adding a term to the electric field such that equations (3) and (4) are identically satisfied, and is alternated with a series of qmr iterations in equation (2).

THE 3D MAGNETOTELLURIC INVERSE PROBLEM

Regularized least squares

All least squares solutions begin by minimizing the difference between observed and predicted data, often subject to a constraint, which is employed to stabilize the inversion process. In the problem considered here, the inverse solution is constrained by Tikhonov regularization to remove its ill posed nature (Tikhonov & Arsenin, 1977). Regularization imposes an additional constraint on the data fit: reconstructions are required to be smoothed versions of the earth's electrical conductivity, at the expense of an increase in the error (the difference between the measured and predicted data). Let's divide the earth into M cells and assign to each cell an unknown conductivity value; the magnetic permeability is assumed to be constant and set to its free space value from here on. Further let $\mathbf{m}$ be a vector of length M that describes these values. We now form a cost functional which combines the data error and model smoothness constraint in the following fashion:

$$\varphi = \sum_{n=1}^{2N} \{ (Z_n^{obs} - Z_n)/\varepsilon_n \}^2 + \lambda \, \mathbf{m}^T \mathbf{W}^T \mathbf{W} \, \mathbf{m}, \tag{5}$$

where T denotes the transpose operator. In equation (5), the terms that describe the observed and predicted data (magnetotelluric impedances), Z_n^{obs} and Z_n, are split into their real and imaginary parts. The summation is over the first N data points are for the real parts of the impedance and the summation over the last N data points are for the imaginary parts. The impedance can be any particular component of the impedance tensor at any given measurement location, where the tensor is given by

$$\mathbf{Z} = \begin{matrix} Z_{xx} & Z_{xy} \\ Z_{yx} & Z_{yy} \end{matrix} . \qquad (6)$$

Components of the tensor, which depend on the subsurface conductivity, relate the measured electric and magnetic fields with each other. For example, $E_y = Z_{yx} H_x + Z_{yy} H_y$, gives the contribution to the y-component of electric field arising from the x and y components of magnetic field. We also weight the data misfit in equation (5) by ε_n so that noisier data are given smaller weight when forming φ.

The parameters that dictate model smoothness are the regularization matrix **W**, which consists of a finite difference approximation to the Laplacian (∇^2) operator, and the regularization parameter λ, which is used to control the amount of smoothness to be incorporated into the reconstruction. Care needs to be taken in selecting this parameter. Large parameters will produce highly smooth models, however these models show poor dependence on the data. Small parameters give superior data fits but the resulting models can be too rough and non-physical. Our strategy is to run the inversion using several fixed values of λ and select the model that provides an acceptable match to the data within observational errors and yet yields the smoothest reconstruction. Because we plan to employ a nonlinear method to minimize the cost functional, λ should not be varied during the iteration procedure. To do so could result in a less efficient algorithm as the minimum of the cost functional is approached since desirable convergence properties of the method can no longer be assured. Note that this restriction on λ is not necessary when linearized update methods are applied to the problem, where λ can be varied between updates.

In small scale inverse problems it may be feasible to determine the minimum of equation (5) with a brute force search in parameter space. For large scale problems, as considered here, this is not an option. Instead, what is typically done is to set the gradient of the cost functional, $\nabla\varphi$, with respect to the model parameters to zero and find by some economical means those model parameters that satisfy the critical point. To insure that $\nabla\varphi=0$ actually defines a minimum instead of a saddle point, second derivative tests are also necessary to verify that the Hessian of the cost functional is symmetric positive definite. Because the predicted impedances depend on the model, **m**, in a nonlinear fashion, we are required to solve $\nabla\varphi=0$ using an iterative method. From our prior discussions, the nonlinear conjugate gradient method is ideal for this task.

Nonlinear conjugate gradients

The method of steepest descent is the easiest understood and simplest to implement of the gradient methods. Unfortunately it usually converges very slowly in

practice. A better approach is the method of nonlinear conjugate gradients, first proposed by Fletcher & Reeves (1964) for nonlinear optimization, and later improved by Polyak & Ribière (1969). The method is closely related to the linear CG method of Hestenes & Stiefel (1952) and is in fact identical if the objective functional is quadratic and exact line searches are made with the NLCG algorithm. Listed below is an outline of the Polyak & Ribière algorithm that will be used in the analysis:

(1) choose $\mathbf{m}_{(1)}$ and select $\mathbf{r}_{(1)} = -\nabla\varphi(\mathbf{m}_{(1)})$

(2) set $\mathbf{u}_{(1)} = \mathbf{M}_{(1)}^{-1}\mathbf{r}_{(1)}$

(3) find $\alpha(i)$ that minimizes $\varphi(\mathbf{m}_{(i)} + \alpha_{(i)}\mathbf{u}_{(i)})$

(4) set $\mathbf{m}_{(i+1)} = \mathbf{m}_{(i)} + \alpha_{(i)}\mathbf{u}_{(i)}$ and $\mathbf{r}_{(i+1)} = -\nabla\varphi(\mathbf{m}_{(i+1)})$

(5) Stop when $|\mathbf{r}_{(i+1)}|$ is sufficiently small, otherwise go to step (6).

(6) set $\beta_{(i+1)} = (\mathbf{r}_{(i+1)}^{T}\mathbf{M}_{(i+1)}^{-1}\mathbf{r}_{(i+1)} - \mathbf{r}_{(i+1)}^{T}\mathbf{M}_{(i)}^{-1}\mathbf{r}_{(i)})/\mathbf{r}_{(i)}^{T}\mathbf{M}_{(i)}^{-1}\mathbf{r}_{(i)}$

(7) set $\mathbf{u}_{(i+1)} = \mathbf{M}_{(i+1)}^{-1}\mathbf{r}_{(i+1)} + \beta_{(i+1)}\mathbf{u}_{(i)}$

(8) Go to step (3)

For now we define $\mathbf{M}_{(i)}^{-1}$ and $\mathbf{M}_{(i+1)}^{-1}$ as identity matrices for all i, with units of $(S/m)^2$ given that the cost functional in equation (5) is dimensionless. We will redefine these matrices later when preconditioning is discussed. To use the NLCG method sensibly requires that we carefully implement two calculations of the procedure efficiently. These are (1) calculate the gradient of the cost functional and (2) minimize φ along a specified ray economically, that is, find the value of α that minimizes the expression $\varphi(\mathbf{m} + \alpha\mathbf{u})$ for specified model parameters $\mathbf{m}$ and a given conjugate search direction $\mathbf{u}$.

Computation of the gradients

The gradient of the cost functional in equation (5) is formally written as

$$\nabla\varphi = \nabla\varphi_d + \lambda\nabla\varphi_m, \tag{7}$$

where φ_d , φ_m are functionals that relate to the data misfit and the model smoothness constraint, respectively. Evaluation of $\nabla\varphi_m$ leads immediately to

$$\nabla\varphi_m = 2\mathbf{W}^{T}\mathbf{W}\mathbf{m}\,, \tag{8}$$

where T denotes the transpose operator.

To compute a specific element of $\nabla\varphi_d$, we redefine the weighted impedance in equation (5) to be a complex quantity, where

$$\Delta Z_n = \text{cmplx}\{\text{Re}(Z_n^{obs} - Z_n)/\text{Re}(\varepsilon_n), \text{Im}(Z_{n+N}^{obs} - Z_{n+N})/\text{Im}(\varepsilon_{n+N})\}, \quad (9)$$

and for the k_{th} model parameter we have

$$\partial\varphi_d / \partial m_k = -2\,\text{Re}\sum_{n=1}^{N} (\Delta Z_n)^* \; \partial Z_n / \partial m_k, \quad (10)$$

where * stands for complex conjugation.

In Appendix A, model sensitivity elements of the impedance are shown to be

$$\begin{aligned}
\partial Z_{xxj} / \partial m_k &= -{}^1\boldsymbol{g}_j^{T}{}_{xx}\,\mathbf{K}^{-1}(\partial\mathbf{K}/\partial m_k\mathbf{E}_1) - {}^2\boldsymbol{g}_j^{T}{}_{xx}\,\mathbf{K}^{-1}(\partial\mathbf{K}/\partial m_k\mathbf{E}_2)\\
\partial Z_{xyj} / \partial m_k &= -{}^1\boldsymbol{g}_j^{T}{}_{xy}\,\mathbf{K}^{-1}(\partial\mathbf{K}/\partial m_k\mathbf{E}_1) - {}^2\boldsymbol{g}_j^{T}{}_{xy}\,\mathbf{K}^{-1}(\partial\mathbf{K}/\partial m_k\mathbf{E}_2)\\
\partial Z_{yxj} / \partial m_k &= -{}^1\boldsymbol{g}_j^{T}{}_{yx}\,\mathbf{K}^{-1}(\partial\mathbf{K}/\partial m_k\mathbf{E}_1) - {}^2\boldsymbol{g}_j^{T}{}_{yx}\,\mathbf{K}^{-1}(\partial\mathbf{K}/\partial m_k\mathbf{E}_2)\\
\partial Z_{yyj} / \partial m_k &= -{}^1\boldsymbol{g}_j^{T}{}_{yy}\,\mathbf{K}^{-1}(\partial\mathbf{K}/\partial m_k\mathbf{E}_1) - {}^2\boldsymbol{g}_j^{T}{}_{yy}\,\mathbf{K}^{-1}(\partial\mathbf{K}/\partial m_k\mathbf{E}_2).
\end{aligned} \quad (11)$$

These sensitivities quantify small changes in the tensor elements at location j due to small changes in the kth model parameter. $\mathbf{K}^{-1}$ denotes the inverse of the finite difference stiffness matrix employed in the solution of the forward problem in equation (2) and depends implicitly on frequency. The electric fields, $\mathbf{E}_1$ and $\mathbf{E}_2$, in equation (11), are also determined from the forward problem; they provide the two source polarizations necessary to define the impedance tensor at each frequency. The eight vectors $({}^1\boldsymbol{g}_j^{T}{}_{xx}, {}^2\boldsymbol{g}_j^{T}{}_{xx}, {}^1\boldsymbol{g}_j^{T}{}_{xy}, {}^2\boldsymbol{g}_j^{T}{}_{xy}, {}^1\boldsymbol{g}_j^{T}{}_{yx}, {}^2\boldsymbol{g}_j^{T}{}_{yx}, {}^1\boldsymbol{g}_j^{T}{}_{yy}, {}^2\boldsymbol{g}_j^{T}{}_{yy})$, specified in Appendix A, are linear combinations of vectors that interpolate electric and magnetic fields for the two source polarizations from the forward-modeling finite-difference grid to the receiver site at location j.

Combining equations (10) and (11) we have

$$\partial\varphi_d/\partial m_k = 2\,\text{Re}\Big\{\sum_{n=1}^{N} (\Delta Z_n)^*\, {}^1\boldsymbol{g}_n^{T}\,\mathbf{K}^{-1}(\partial\mathbf{K}/\partial m_k\mathbf{E}_1) + \sum_{n=1}^{N} (\Delta Z_n)^*\, {}^2\boldsymbol{g}_n^{T}\,\mathbf{K}^{-1}(\partial\mathbf{K}/\partial m_k\mathbf{E}_2)\Big\} \quad (12)$$

where the vectors, ${}^1\boldsymbol{g}_n^{T}$ and ${}^2\boldsymbol{g}_n^{T}$ are determined by selecting from equation (11) the component of the impedance that is being treated according to the summation index. For example, if we are treating Z_{xyj} as the n_{th} data point, then ${}^1\boldsymbol{g}_n^{T} = {}^1\boldsymbol{g}_j^{T}{}_{xy}$ and ${}^2\boldsymbol{g}_n^{T} = {}^2\boldsymbol{g}_j^{T}{}_{xy}$.

It is now possible to show that the number of forward solves needed to evaluate the gradient in equation (12) is only four per frequency. Two solves are required to obtain the electric fields $\mathbf{E}_1$ and $\mathbf{E}_2$ and two additional solves are needed to compute the fields arising from the following source distributions

$$ {}^1\mathbf{g}^T = -2 \sum_{n=1}^{N} (\Delta Z_n)^* \, {}^1g_n^T \tag{13} $$

and

$$ {}^2\mathbf{g}^T = -2 \sum_{n=1}^{N} (\Delta Z_n)^* \, {}^2g_n^T. \tag{14} $$

Thus if we set

$$ {}^1\mathbf{v}^T = {}^1\mathbf{g}^T \mathbf{K}^{-1} \tag{15} $$

and

$$ {}^2\mathbf{v}^T = {}^2\mathbf{g}^T \mathbf{K}^{-1}, \tag{16} $$

we then are required to solve the following two forward problems

$$ \mathbf{K}\,{}^1\mathbf{v} = {}^1\mathbf{g} \tag{17} $$

and

$$ \mathbf{K}\,{}^2\mathbf{v} = {}^2\mathbf{g}. \tag{18} $$

Here we utilized the fact that $\mathbf{K}^T = \mathbf{K}$. In solving these forward problems we also employ the static divergence correction to accelerate their solutions at the lower frequencies. Here equation (3) is modified to read $\nabla \cdot \sigma \mathbf{E} + \nabla \cdot \mathbf{J} = 0$, where $\mathbf{J}$ is the source current density and is given by either ${}^1\mathbf{g}$ or ${}^2\mathbf{g}$. Additional details on the modified static divergence procedure can be found in Newman & Alumbaugh (1996) and Alumbaugh & Newman (1996).

The line search

Because a line search is needed to minimize $\varphi(\mathbf{m} + \alpha\mathbf{u})$, this will require additional forward solutions. There are number of strategies to carry out the line search, where the number of forward modeling applications varies. An economical approach, employed here and presented in detail in Appendix B, is to find α such that $\varphi(\mathbf{m} + \alpha\mathbf{u})$ is sufficiently decreased along the search direction $\mathbf{u}$. Quadratic curve fitting is also employed in an attempt to refine α so that an even greater reduction in φ is possible. Here, we use functional and derivative information at one point and functional information at another, and then fit a quadratic through these points to estimate the step to the minimum. Since cost functional and gradient information is already available at the

descent point, $\mathbf{m}$, from the prior NLCG iteration, we only need to evaluate φ at the second point along the direction of descent. Thus the cost of the quadratic line search is two additional forward modeling applications per frequency. If the functional increases at the estimated minimum point, a backtracking strategy is invoked from this point until a sufficient decrease in the functional is observed. Backtracking can be done because $\mathbf{u}$ is a descent direction, since $\mathbf{u} \cdot \nabla\varphi < 0$ at $\varphi(\mathbf{m})$. We have found in practice that backtracking is typically not required in our scheme. While it may seem preferable to use higher order polynomial interpolation such as a cubic to refine the line search, this can be expensive since it incurs additional functional and possible gradient evaluations (cf., Acton, 1990). In fact a good preconditioner, without recourse to additional forward modeling, can help compensate for the approximate line search procedure employed here and is discussed below.

Preconditioning

The findings of Rodi & Mackie (1998) show that convergence rates for the 2D MT inverse problem using nonlinear conjugate gradients can be significantly improved with preconditioning. Nevertheless as Nocedal (1996) points out, the use of a preconditioner with a NLCG scheme can result in conjugate search direction no longer being a descent direction and requires reinitializing using the steepest descent direction, which severely impairs the algorithm's efficiency. In spite of these dangers, an effective and robust preconditioner is well worth pursuing, since it would have a tremendous impact in reducing solution run times for the 3D problem.

The convergence of the NLCG method can be accelerated by choosing a preconditioner $\mathbf{M}_{(i)}$ that approximates the Hessian of the cost functional, where $\mathbf{M}_{(i)}^{-1}$ requires minimal storage and $\mathbf{M}_{(i)}^{-1}\,\mathbf{r}$ is easy to compute. $\mathbf{M}_{(i)}$ can be fixed or updated at each iteration of the procedure. We prefer to update $\mathbf{M}_{(i)}$, since the Hessian is not constant, except for points near the minimum of the cost functional. When the Hessian is constant the cost functional can be represented by a quadratic functional in the model parameters.

While it is too expensive to compute or approximate the full Hessian, it is possible to compute its diagonal for use as a preconditioner. This information is accessible from computations involved in the NLCG iteration. Using a Quasi-Newton formula, known as the *Broyden-Fletcher-Goldfarb-Shanno* (BFGS) update (cf., Dennis & Schnabel, 1996) we can recur the diagonal of the Hessian even if its off-diagonal components are unknown, where

$$\mathbf{M}_{(i+1)} = \mathbf{M}_{(i)} + \nabla\varphi(\mathbf{m}_{(i)})\,\nabla\varphi(\mathbf{m}_{(i)})^{T} / \nabla\varphi(\mathbf{m}_{(i)})^{T}\,\mathbf{u}_{(i)} + \mathbf{y}_{(i)}\,\mathbf{y}_{(i)}^{T} / \alpha_{(i)}\,\mathbf{y}_{(i)}^{T}\,\mathbf{u}_{(i)}, \quad (19)$$

with $\mathbf{y}_{(i)} = \nabla\varphi(\mathbf{m}_{(i+1)}) - \nabla\varphi(\mathbf{m}_{(i)})$. The use of this update as a diagonal preconditioner in the NLCG inversion scheme is justified because in the quadratic case with exact line searches, identical search directions are generated by the BFGS and NLCG algorithms

(Gill et al., 1981). Additional justification that equation (19) should be an effective preconditioner comes from the optimization literature, where the Newton search direction, $\mathbf{s} = \mathbf{M}_{(i)}^{-1}\,\mathbf{r}$, if practical to compute, is the optimum choice for functional minimization. Since full evaluation of $\mathbf{M}_{(i)}^{-1}$ is not realistic, its evaluation using only diagonal entries is an obvious choice. Thus the effect of the preconditioner on the NLCG scheme is to attempt to make it behave more like Newton's method.

Logarithmic parameters

Inverting for log parameters is very desirable since it restricts the parameters to be positive quantities, which is a physical requirement for the electrical conductivity. Reformulation of the inverse problem for log parameters with lower bounds requires that elements of $\mathbf{m}$ be redefined as $m'_k = \ln\{(m_k - lb_k)/m_o\}$ in equations (5) and (8), where $m_k > lb_k$, with $lb_k > 0$ (Newman & Alumbaugh, 1997) and m_o equals 1 S/m. The gradient in equation (10) is also modified to read

$$\partial\varphi_d/\partial m'_k = -2\,\mathrm{Re}\sum_{n=1}^{N}(m_k - lb_k)/m_o\,(\Delta Z_n)^*\,\partial Z_n/\partial m_k. \qquad (20)$$

A corresponding modification applies as well to equation (12). Once m'_k is updated in the NLCG iteration, the parameter components that are of interest follow from the expression

$$m_k = m_o\,e^{m'_k} + lb_k, \qquad (21)$$

PARALLEL IMPLEMENTATION

In spite of the aforementioned efficiencies of the NLCG method in limiting the number of forward modeling applications at each iteration of the procedure, 3D forward modeling continues to be a bottleneck in achieving acceptable run times. The expensive components in the procedure, functional gradients and cost functional evaluations, are traced to the time required to solve the 3D forward problem. This is also compounded because multiple inversion runs are needed to determine the optimal tradeoff parameter and sometimes the correct data weighting. Therefore, any reduction in forward modeling run times would have a corresponding impact in reducing solution times for the inversion. Another difficulty with forward modeling is that to realistically model a full 3D MT survey over all frequencies and spatial locations may in some instances require a forward model parameterization of over a million cells, which is impractical on serial workstations.

To alleviate these difficulties we have implemented the inversion scheme to run on parallel computing platforms. These platforms allow for tens to thousands of processors to operate on the problem simultaneously and significantly reduce solution run times and greatly increase the complexity and realism of the geological models. Such platforms allow for an entire 3D MT data set to be analyzed concurrently, instead of partially. In using these machines the idea is to assign a given number of processors in

each coordinate direction (*nx* in *x*, *ny* in *y* and *nz* in *z*) of the model, where the total number of processors employed is equal to *nx* X *ny* X *nz*. Because each processor needs only to make calculations for a subset of the forward and inverse problems, and because the processors are making their calculations in parallel, the solution time is reduced by a factor approximately equal to the number of processors employed.

The papers of Newman & Alumbaugh (1997) and Alumbaugh et al. (1996) show how to implement inverse and forward problems on parallel platforms for controlled source applications. Generalization to the MT problem is a straightforward extension and the interested reader is referred to these papers for the additional details. Curently the MT inversion scheme has been implemented on the 9000-processor Tera-flop machine available at Sandia National Laboratories. Preliminary analysis of a large field data set shows the advantages of a parallel version of the scheme, where 28,224 model parameters were estimated using approximately 13,000 data points. A speed up of a factor of 42 was observed when 512 Pentium II processors were applied to the problem compared to a single processor IBM RS-6000 590 workstation (one inversion iteration required nearly 16 hours on the IBM). If 1,000 processors are employed the speed up approaches two orders of magnitude. Note that the processor speed on the IBM workstation is roughly comparable to eight Pentium II processors.

SYNTHETIC EXAMPLES

Two synthetic tests will be presented to demonstrate the benefits of preconditioning and to examine the solution by inverting a data set produced by the integral equation modeling code of Xiong (1992). This latter test is very important because it provides an independent check on the solution. Data simulated with an integral equation code are susceptible to different types of numerical errors compared to the finite difference technique, which is employed within the inverse solution.

Consider the 3D model in Figure 3, which represents a 0.1 S/m block embedded in a 0.01 S/m half-space. The horizontal and vertical dimensions of the body are 200 m on a side. Its depth of burial is 100 m. The mesh used in both the forward and inverse computations has been designed to increase with depth, approximately on a log scale, reflecting the loss of resolution with depth, which is an inherent limitation of the MT method. One hundred and twenty one MT soundings were simulated using the finite difference technique at 16 frequencies, from 4,000 Hz to 4 Hz, giving the total number of data points (real and imaginary) to be 15,488. Each sounding provides all four elements of the impedance tensor. For the data weights, we simply used one percent of the impedance of a 0.01 S/m half-space. To more clearly show the benefits of preconditioning at the later iterations, we did not to add random noise to the data in this particular example. While preconditioning is also effective when random noise is present, its benefits can be more dramatically demonstrated without it. Random noise will be considered in the second test example.

The inversion domain is a rectangular block, 600 m in the horizontal directions and 500 m in the vertical direction. It is a subset of the forward modeling domain used to compute functional gradients and predicted data, which is 1,000 m on a side. In this example 1,764 and 21,952 cells were used to represent the inversion and forward

domains. Approximately 1 hour per inversion iteration was required on an IBM RS6000 590 workstation and compares with eight minutes when 125 processors of the teraflop machine are dedicated to the problem.

The reconstruction shown in Figure 4 yields a smooth model, which compares favorably with the test model shown in Figure 3. The cross sections centered on x and y coordinate axis and the conductivity map, between 150 and 200 m depth demonstrate that the lateral geometry of the target is well resolved. In Figure 5 we show plots of the squared error against iteration count. A target misfit of one assumes a noise model based on one percent of the impedance of a 0.01 S/m half-space. It indicates that the solution matches the data to within observational errors if Gaussian noise was assumed. In this example we plot the results using a semi-log scale and ran the preconditioned solution below the hypothetical noise level to more clearly demonstrate the improvement in solution convergence obtained through preconditioning. From these results, it is clear that equation (19) is an effective preconditioner, where at the first iteration $\mathbf{M}_{(1)}$ is set to the identity matrix. Curvature information built up by equation (19) scales and steers the conjugate search direction to be a better prediction of the minimum. It is in the later stages of the inversion procedure that the benefits of preconditioning become obvious. This comes as no surprise, since equation (19) will converge to the Hessian of the cost functional in the neighborhood about the minimum. Nevertheless, our findings on effective preconditioners for the 3D inverse problem are preliminary. Rodi & Mackie (1998) have shown that for the 2D problem, a fixed preconditioner is very effective; we found this type of preconditioner ineffective for the 3D scheme presented here. Thus we believe additional research is needed on effective preconditioners for the 3D problem.

The second test model is shown in Figure 6, where two near surface bodies (conductive and resistive) have been added to demonstrate the inversion code's capability to invert data that are affected by static shifts. Here the depth of burial and extent for the near surface conductor are 10 m. For the resistor they are 15 and 35 m, respectively. Data for this model were simulated using the integral equation solution of Xiong (1992), where 1 percent Gaussian random noise was added to the data. The data weights we assumed in the inversion are the same as before: one percent of the impedance of a 0.01S/m half-space. Because of the near surface bodies, a fine mesh was employed in the near surface, where 2,548 and 28,224 cells were used to represent the respective inversion and forward modeling domains. Three separate inversion runs with preconditioning were carried out for three different tradeoff parameters of 30, 3 and 0.3 and the corresponding images are shown in Figures 7, 8 and 9. The inversion runs producing these images were also terminated at different iterations in Figure 10 to study how small error reductions at the later iterations affect the final image.

For the three different regularization parameters (30, 3 and 0.3) we were not able to drive the squared error to the assumed noise level in Figure 10. Nevertheless all final error levels are quite close to one and given that there is a component of numerical noise in the simulation of the data that is clearly non random and non Gaussian, we are not surprised that we could not achieve the expected fit. It was also found that the tradeoff parameter of 3 produced the model which that yielded the closest matched to the assumed noise level. It would be a mistake, however, to say that this image is optimal, given the non Gaussian nature of the noise. Finally, to successfully invert the data set required 6 hours of CPU time per inversion iteration on the IBM workstation. This compared with 30

minutes for 125 nodes on the Teraflop machine, which is more than an order of magnitude faster.

The reconstruction in Figure 7 (λ=30) shows that we have clearly recovered information on both near surface bodies. Not shown, however, is the image illustrating that the near surface bodies have been projected onto the earth's surface. Because the highest frequency component in the data set is only 4 kHz, this frequency is insufficient to resolve the true depths of the near surface bodies, since the skin depth is 79 m in 0.01 S/m material. We have also recovered information on the deeper conductor's geometry (depth of burial and depth and lateral extents). The maximum conductivity estimates are, however, about a factor of two too small.

The images employing the smaller tradeoff parameters (Figures 8 and 9) are not nearly as smooth and show more variability in the conductivity structure, as expected. Nevertheless, the images also show evidence of the near surface structures. The presence of the deeper conductor is also clearly indicated, but the maximum conductivity estimates are a factor two too large. An interesting difference between these two images is the estimated depth to the base of the deeper conductor. The image along the Y-Z cross section, based on $\lambda = 3$, shows the conductor to extend to 500 m depth compared to 400 m depth when $\lambda = 0.3$. This difference can be explained with the number of NLCG iterations employed to construct the respective images. Fifty iterations were used to construct the image in Figure 8, whereas 27 iterations were used in Figure 9. When 20 iterations are used to reconstruct the image for $\lambda = 3$, the base of the deeper conductor is better resolved as well as its conductivity (Figure 11). This indicates that the benefit of a small reduction in the error level at the later iterations can be offset by extraneous structure in the final image.

In Figure 12, we compare the convergence rate for the case $\lambda = 3$, with and without preconditioning. Preconditioning is found to be beneficial, as far fewer iterations are necessary to drive the squared error to a given level at the later iterations, compared with a solution that does not use it. The final error level for the solution without preconditioning required 33 iterations This same error level was achieved in only 20 iterations when the preconditioned form of the solution was employed. The image produced without preconditioning is shown in Figure 13 and should be compared directly with Figure 11. In this example, the image in Figure 11 resolves the deeper conductor somewhat better.

RESOLUTION ANALYSIS OF WMD FACILITIES

The resolution analysis for characterizing WMD facilities will be based on the model shown in Figure 6. The deeper conductor in that figure can be considered to be a hypothetical facility, which we desire to image in the presence of near surface geological variations. The previous results indicate that it is possible to image the facility with extensive data coverage. The question we pose here in this analysis is the number of sounding locations and spatial coverage necessary to characterize WMD facilities.

We now consider ten data sets where the spatial coverage varies and the number of sounding locations range from thirty six to one in Figures 14 through 23. The noise model we will employ in this analysis is again 1 percent Gaussian random noise with the data sets once more produced by the integral equation code of Xiong (1992). Finally a

tradeoff parameter of thirty will be used to invert the data; we selected a larger tradeoff parameter to help avoid over fitting the data sets and producing reconstructions that are non-physical. Plots of the squared error against iteration count for the different data sets are illustrated in Figures 24 to 33.

The reconstruction in Figure 14 shows that with thirty six soundings over the facility one can characterize the depth to the top of the facility and its lateral geometry. On the other hand, the conductivity of the facility is underestimated and its base depth is overestimated, as expected from previous results. In addition to the facility, the near surface conductivity structures have been imaged. The results are quite similar to the image in Figure 7, where the station density is more than three times greater. The plot of the squared error (Figure 23) shows that the predicted data match closely with the observations to within the assumed noise level. In Figure 15 the number of sounding locations has been reduced to twenty five, where spatial coverage is similar to that in Figure 14. Once again the facility has been imaged, including its depth of burial and lateral extent. Estimates of its base depth are not so good, however. It appears that the base facility extends to 500 m depth. The data fit for this example is also quite good (Figure 25).

In the next example (Figure 16) we consider nine sounding locations, with eight on the perimeter of the facility and one directly over it. In this instance it is still possible to infer information on the buried facility including its depth of burial and lateral extent. The plot of the squared error against iteration count indicated that at thirty iterations that the initial squared error has been reduced by more than a factor ten, but the final error level is still about fifty percent larger than the assumed noise level (Figure 26). Nevertheless the image in Figure 16 indicates that we can make clear inferences on the facility location. In actual practice it may not be possible to make a sounding directly over the facility. The next the next example, (Figure 17) we explore the resolving power of the method when soundings are taken only around the perimeter of the facility. In this situation it is still possible to infer the presence of the facility, including once more its depth of burial and lateral extent, even though we still cannot fit the data to within the assumed noise level (Figure 27). However, when fewer soundings are made on the facility perimeter (Figures 18, 19, 20 and 21) it is not possible to make any clear inferences about the facility. Plots of the squared error against iteration count for these examples are illustrated in Figures 28, 29, 30 and 31.

Though it may not be practical, it is worthwhile to investigate the resolving power of the MT method when a single MT sounding can be taken directly over the facility (Figure 22). If such a measurement can be made it appears that it is possible to infer the depth of burial of the facility as well as get a rough idea about the its lateral geometry. Making inferences about the base depth of the facility is not possible, however. The plot of the squared error in Figure 32 shows a significant reduction with iteration count compared with the examples in Figures 28, 29, 30 and 31. This is expected since the sounding location directly over the facility is greatly influenced by it, where as the sounding locations on the perimeter are to a much lesser degree. This indicates that when making these types of measurements it is critical, as well as obvious, to select sites where the measurements will show the greatest sensitivity to the facility, but yet can be made in a covert manner. To conclude this section, we consider the case where the single sounding site is slightly offset from the position directly over the facility (Figure 23). In

this event, the reconstruction of the facility is considerably degraded. One reason for the degradation is that the measurement site was selected directly over the near surface conductor and the image shows that while it is possible to infer the near-surface structure, its presence may have contributed to the difficulties in imaging the facility. A plot of the squared error against iteration count in Figure 33 also shows a steep decrease in the squared error as in Figure 32, but it appears here that the large initial error is caused more by the near-surface feature than the facility itself.

CONCLUSIONS AND RECOMMENDATIONS

The results of this analysis indicate the following: It is definitely possible to image WMD facilities, including depth of burial and lateral extent if a sufficient number of measurements are taken on the perimeter of the facility. Moreover if a station measurement can be made directly over the facility then the resolution is improved accordingly. In all cases it was not possible to image the base of the facility with any confidence as well as provide any precise inferences on the facility electrical conductivity. This later finding, however, is really not that critical since facility geometry is far more important quantity to have precise knowledge of than its conductivity. The results of the resolution analysis indicate that the MT method is capable of providing geometrical information.

A key concern that should be address if the MT method is ever to be used in characterizing WMD facilities is the logistics of field deployment. The field set up is quite cumbersome and involves measurements of horizontal electric and magnetic field. While the magnetic field measurements can be easily made with small induction coils, the electric field measurements are far more problematic. Extensive electrical wiring, tens of meters in length, is needed and this could make covert measurements next to impossible. For the WMD problem it is recommended that MT measurements be made solely with the magnetic field ratios. In this context it would then be possible to deploy with far greater ease small coils about a suspected facility and would allow for the measurements to be conducted in a more covert manner. Before testing such a measurement system in the field, however, it would be necessary to carry out a similar resolution analysis as was done with MT measurements based on electric and magnetic fields. It is necessary to determine sensitivity of the proposed measurement to underground facilities along with needed data coverage and quality. Such a study is indispensable in producing useful reconstructions of underground facilities. Another issue that needs to be addressed if MT measurements are to be used to characterize WMD facilities is the electromagnetic response generated by the facility. Since the MT method uses natural field emissions, the fields generated by the facility can be considered as a source of noise for the MT measurement. Fortunately the spectral nature of this noise will most likely be confined to the 50 Hz frequency band and signal processing steps could be used for its removal before processing and converting the MT measurements into impedances. On the other hand, direct measurement of this noise could be the basis of a new approach to characterize WMD facilities.

ACKNOWLEDGMENTS

The authors would like to thank Louis Romero for his help in developing estimates to gauge the performance of the new preconditioner developed in the Appendix C and Appendix D of this report. Thurlow Caffey is also acknowledged for his assistance in the model calculations. This work was performed at Sandia National Laboratories with funding provided by the Laboratory Directed Research Development Office. Sandia is a multi-program laboratory operated by the Sandia Corporation, a Lockheed Martin Company, for the United States Department of Energy under Contract DE-AC04-94AL85000.

REFERENCES

Acton, F. S., 1990, *Numerical Methods that Work*, The Mathematical Association of America, Washington D.C.

Alumbaugh, D. L., Newman G. A., Prevost L., & Shadid, J. N., 1996, Three-dimensional wideand electromagnetic modeling on massively parallel computers: Radio Science, **31**, 1-23.

Alumbaugh, D. L., & Newman G. A., 1996, Electromagnetic modeling of perfect conductors in an arbitrary host: Extended Abstract of the Society of Exploration Geophysicists Annual Meeting, Denver Colorado, 978-981.

Dennis, J. E., Jr., & Schnabel, R. B., 1996, *Numerical methods for unconstrained optimization and nonlinear equations*, Society for Industrial and Applied Mathematics, Philadelphia.

Druskin, V., Knizhnerman, L. & Lee, P., 1998, A new spectral Lanczos decomposition method for induction modeling in arbitrary 3D geometry: Geophysics, in press.

Druskin, V., & Knizhnerman, L., 1994, Spectral Lappraoch to solving three-dimensional Maxwell's diffusion equations in the time and frequency domains: Radio Science, **29** 937-953.

Druskin V., and Knizhnerman, L, 1988, A spectral semi-discrete method for the numerical solution of 3-D non-stationary problems in electrical prospecting: Izv. Acad. Sci. USSR, "Phys. Solid Earth", **8**, 63-74 (Russian; translated into English).

Fletcher R., & Reeves, C. M., 1964, Function minimization by conjugate gradients: Computer Journal 7, 149-154.

Gill, P. E., Murray, W., & Wright, M. H., 1981, *Practical Optimization*, Academic Press, London.

Greenbaum, A., 1997, *Iterative methods for solving linear systems*, Society for Industrial and Applied Mathematics, Philadelphia.

Hestenes, M. R. & Stiefel, E, 1952, Methods of conjugate gradients for solving linear systems: J. Res. Nat. Bureau, **49**, 409-436.

LaBrecque, D., 1995, A scalar-vector potential solution for 3D EM finite difference modeling: Proceedings on the International Symposium on Three-dimensional Electromagnetics, Schlumberger-Doll Research, Ridgefield, Connecticut, 143-152.

Mackie, R. L., & Madden T. R., 1993, Three-dimensional magnetotelluric inversion using conjugate gradients: Geophy. J. Int., **115**, 215-229.

Newman, G. A., & Alumbaugh, D. L., 1998, Three-dimensional magnetotelluric inversion using non linear conjugate gradients: Submitted Geophysical Journal International.

Newman, G. A., & Alumbaugh, D. L., 1997, Three-dimensional massively parallel electromagnetic inversion - I. Theory: Geophysical Journal International, **128**, 345-354.

Newman, G. A., & Alumbaugh, D. L., 1996, Electromagnetic modeling of subsurface 3D structures: Proceedings of the International Geoscience and Remote Sensing Symposium (IGARSS), Omaha, Nebraska, 1941-1944.

Newman, G. A., & Alumbaugh, D. L., 1995, Frequency-domain modeling of airborne electromagnetic responses using staggered finite differences: Geophysical Prospecting, **43**, 1021-1042.

Nocedal, J, 1996, Conjugate gradient methods and nonlinear optimization: In Linear and Nonlinear Conjugate Related Methods, Edited by L. Adams and J. L. Nazareth: Society for Industrial and Applied Mathematics, Philadelphia.

Polyak, E., & Ribiere, G., 1969, Note sur la convergence des méthods conjugées: Rev. Fr. Inr. Rech. Oper., **16**, 35-43.

Rodi, W., & Mackie R. L., 1998, Nonlinear Conjugate Gradients Algorithm for 2-D Magnetotelluric Inversion: submitted to Geophysics.

Smith, J. T., 1996, Conservative modeling of 3-D electromagnetic fields; Part II: Biconjugate gradient solution and an accelerator: Geophysics, **61**, 1319-1324.

Tikhonov, A. N. & Arsenin, V. Y., 1977, *Solutions to ill-posed Problems*, John Wiley and Sons, New York, NY.

Vozoff, K., 1986, *The Magnetotelluric.Methods, Edited by Keeva Vozoff, Geophsyical Reprint Series, No. 5,* Society of Exploration Geophysicists, Tulsa, OK.

Vozoff, K, 1972, The Magnetotelluric Method in the Exploration of Sedimentary Basins: Geophysics, **37**, 98-141.

Xiong, Z., 1992, Electromagnetic modeling of 3-D structures by the method of system iteration using integral equations: Geophysics, **57**, 1556-1561.

Yee, K. S., 1966, Numerical solution of initial boundary problems involving Maxwell's equations in isotropic media: IEEE Transactions on Antennas and Propagation, **AP-14**, 302-309.

FIGURE CAPTIONS

Fig. 1 Typical layout of the MT measurement configuration. Time series of the horizontal electric (E_x and E_y) and magnetic (H_x and H_y) fields are measured at the earth's surface. Sometimes the vertical magnetic field (H_z) is measured. After Fourier transformation to the frequency domain, the field quantities are used to from ratios, called impedances, which are then used to interpret the subsurface conductivity. Figure taken from Vozoff, (1972).

Fig. 2 Mesh and staggered grid imposed upon the earth model to simulate 3D MT fields. In the finite difference solution, the electric fields are sampled along cell edges and magnetic fields, implicitly along the cell faces, while conductivity and permeability values are assigned to each cell.

Fig. 3 Three-dimensional test model used in the first synthetic example. The top two panels show depth cross sections over the body, centered on x and y coordinate axis. In the lower panels, a map view of the model is illustrated between 150 and 200 m depth along with the station location map. In these panels, the red color indicates the 0.1 S/m block, 200 m on a side with a depth of burial of 100 m. The blue color represents the 0.01 S/m host.

Fig. 4 Three-dimensional reconstruction of test model in Figure 2, obtained with preconditioning. The color bar provides the range of the parameter estimates in the reconstruction, where conductivity estimates between 150 and 200 m depth approach that of the test body at its center.

Fig. 5 Plot of solution convergence for inversion runs with and without preconditioning (solid and dashed curves). The squared error is determined by equation (5), where the regularization term is not included in the calculation. A tradeoff parameter of twenty was used in the inversion tests.

Fig. 6 Three-dimensional test model used in the second synthetic example. The two top panels are X-Z and Y-Z cross sections centered between –75 and –50 m in the y coordinate and 25 and 50 m in the x coordinate. They show cuts through the near surface resistive body (violet) and conductive body (green), respectively as well as the deeper conductor (red) at depth. The lower panel, to the left, shows the lateral positions of the

near surface bodies between 12.5 and 18.75 m depth. The conductivity color bar scale is located to the right.

Fig. 7 The 3D reconstruction of test model in Figure 6 based on a tradeoff parameter of 30. The top two panels are images along the X-Z and Y-Z cross sections illustrated in Figure 6. The lower right-hand panel is a map view of the reconstructed conductivity between 150 and 200m depth and should be compared with the depth section in the lower right hand panel of Figure 3. The conductivity color bar scale for the reconstruction is shown in Figure 5.

Fig. 8 The 3D reconstruction of test model in Figure 6 based on a tradeoff parameter of 3. Conductivity estimates, indicated by the red color cells, range between 0.2 and 0.08 S/m.

Fig. 9 The 3D reconstruction of test model in Figure 6 based on a tradeoff parameter of 0.3. Once again, conductivity estimates indicated by the red color cells, range between 0.2 and 0.08 S/m.

Fig. 10 A plot of solution convergence for three different tradeoff parameters of 30, 3 and 0.3.

Fig. 11 The 3D reconstruction of test model in Figure 6 based on a tradeoff parameter of 3 at 20 iterations. Red color cells indicate that the conductivity ranges between 0.13 and 0.08 S/m.

Fig. 12 A plot of solution convergence with and without preconditioning for the test model in Figure 6, where the tradeoff parameter is set to 3.

Fig. 13 The 3D reconstruction of test model in Figure 6 based on a tradeoff parameter of 3 at 33 iterations without preconditioning. Red color cells indicate that the conductivity ranges between 0.13 and 0.08 S/m. This image should be compared with that in Figure 11 to show differences in the respective images at approximately the same data misfit.

Fig. 14 3D reconstruction of a hypothetical facility based on thirty six soundings. The image in the upper left-hand corner indicates near surface variability of the conductivity as well as the survey layout. The image in the right hand corner is the reconstruction between 150 and 200 m depth. The lower two images are cross-sectional images taken between –75 and –50 in the y coordinate direction and 25 and 50 m in the x coordinate. The conductivity color bar scale is located to the right.

Fig. 15 3D reconstruction of the facility based on twenty five soundings.

Fig. 16 3D reconstruction of the facility based on nine soundings

Fig. 17 3D reconstruction of the facility based on eight soundings located on the facility perimeter.

Fig. 18 3D reconstruction of the facility based on four soundings located on the facility perimeter.

Fig. 19 3D reconstruction of the facility based on two soundings located on the facility perimeter.

Fig. 20 3D reconstruction of the facility based on a single sounding located on the facility perimeter.

Fig. 21 3D reconstruction of the facility based on a single sounding located on the facility perimeter.

Fig. 22 3D reconstruction of the facility based on a single sounding located directly over the facility.

Fig. 23 3D reconstruction of the facility based on a single sounding offset 71 m from the site located directly over the facility.

Fig. 24 Plot of squared error against iteration count for the reconstruction in Figure 14. The assumed noise level is indicated by the dotted line.

Fig. 25 Plot of squared error against iteration count for the reconstruction in Figure 15.

Fig. 26 Plot of squared error against iteration count for the reconstruction in Figure 16.

Fig. 27 Plot of squared error against iteration count for the reconstruction in Figure 17.

Fig. 28 Plot of squared error against iteration count for the reconstruction in Figure 18.

Fig. 29 Plot of squared error against iteration count for the reconstruction in Figure 19.

Fig. 30 Plot of squared error against iteration count for the reconstruction in Figure 20.

Fig. 31 Plot of squared error against iteration count for the reconstruction in Figure 21.

Fig. 32 Plot of squared error against iteration count for the reconstruction in Figure 22.

Fig. 33 Plot of squared error against iteration count for the reconstruction in Figure 23

Fig. 34 Demonstration of the preconditioner effectiveness at 4 Hz. The test model is that of Figure 3. The plot shows the number of iterations and computation time needed to solve equation (C2) for a single source polarization using the qmr method for different types of preconditioning. Preconditioning based on the approximate solution technique at low induction numbers is far superior to Jacobi preconditioning. All times are for an IBM RS-6000 590 workstation.

Fig. 35 Demonstration of the preconditioner effectiveness at 400 Hz.

Appendix A

Model sensitivity elements for the MT impedance tensor

In order to derive the model sensitivities, we need the predicted impedance tensor, where two orthogonal source polarizations are required. Following Mackie & Madden (1993), let the electric and magnetic fields for the two polarizations be denoted by E_{x1}, E_{y1}, H_{x1}, H_{y1} and E_{x2}, E_{y2}, H_{x2}, H_{y2}. Thus

$$Z_{xx} = \frac{E_{x1} H_{y2} - E_{x2} H_{y1}}{H_{x1} H_{y2} - H_{x2} H_{y1}}, \quad Z_{xy} = \frac{E_{x2} H_{x1} - E_{x1} H_{x2}}{H_{x1} H_{y2} - H_{x2} H_{y1}}$$

$$Z_{yx} = \frac{E_{y1} H_{y2} - E_{y2} H_{y1}}{H_{x1} H_{y2} - H_{x2} H_{y1}}, \quad Z_{yy} = \frac{E_{y2} H_{x1} - E_{y1} H_{x2}}{H_{x1} H_{y2} - H_{x2} H_{y1}} \tag{A1}$$

Differentiating each tensor element in equation (A1) with respect to the kth model parameter, m_k, yields

$$\begin{aligned}\partial Z_{xx}/\partial m_k = &\{(H_{x1}H_{y2} - H_{x2}H_{y1})(H_{y2}\partial E_{x1}/\partial m_k + E_{x1}\partial H_{y2}/\partial m_k - H_{y1}\partial E_{x2}/\partial m_k - E_{x2}\partial H_{y1}/\partial m_k)\\ &-(E_{x1}H_{y2} - E_{x2}H_{y1})(H_{y2}\partial H_{x1}/\partial m_k + H_{x1}\partial H_{y2}/\partial m_k - H_{y1}\partial H_{x2}/\partial m_k - H_{x1}\partial H_{y1}/\partial m_k)\}/\\ &(H_{x1}H_{y2} - H_{x2}H_{y1})^2\end{aligned}$$

$$\begin{aligned}\partial Z_{xy}/\partial m_k = &\{(H_{x1}H_{y2} - H_{x2}H_{y1})(H_{x1}\partial E_{x2}/\partial m_k + E_{x2}\partial H_{x1}/\partial m_k - H_{x2}\partial E_{x1}/\partial m_k - E_{x1}\partial H_{x2}/\partial m_k)\\ &-(E_{x2}H_{x1} - E_{x1}H_{x2})(H_{y2}\partial H_{x1}/\partial m_k + H_{x1}\partial H_{y2}/\partial m_k - H_{y1}\partial H_{x2}/\partial m_k - H_{x2}\partial H_{y1}/\partial m_k)\}/\\ &(H_{x1}H_{y2} - H_{x2}H_{y1})^2\end{aligned} \tag{A2}$$

$$\begin{aligned}\partial Z_{yx}/\partial m_k = &\{(H_{x1}H_{y2} - H_{x2}H_{y1})(H_{y2}\partial E_{y1}/\partial m_k + E_{y1}\partial H_{y2}/\partial m_k - H_{y1}\partial E_{y2}/\partial m_k - E_{y2}\partial H_{y1}/\partial m_k)\\ &-(E_{y1}H_{y2} - E_{y2}H_{y1})(H_{y2}\partial H_{x1}/\partial m_k + H_{x1}\partial H_{y2}/\partial m_k - H_{y1}\partial H_{x2}/\partial m_k - H_{x2}\partial H_{y1}/\partial m_k)\}/\\ &(H_{x1}H_{y2} - H_{x2}H_{y1})^2\end{aligned}$$

$$\begin{aligned}\partial Z_{yy}/\partial m_k = &\{(H_{x1}H_{y2} - H_{x2}H_{y1})(H_{x1}\partial E_{y2}/\partial m_k + E_{y2}\partial H_{x1}/\partial m_k - H_{x2}\partial E_{y1}/\partial m_k - E_{y1}\partial H_{x2}/\partial m_k)\\ &-(E_{y2}H_{x1} - E_{y1}H_{x2})(H_{y2}\partial H_{x1}/\partial m_k + H_{x1}\partial H_{y2}/\partial m_k - H_{y1}\partial H_{x2}/\partial m_k - H_{x2}\partial H_{y1}/\partial m_k)\}/\\ &(H_{x1}H_{y2} - H_{x2}H_{y1})^2\end{aligned}$$

An easy check is available on these expressions for a 2D earth model. For both field polarizations we would have

$$\begin{aligned}(E_{x1}, H_{y1}) &\neq 0\\ (E_{y1}, H_{x1}) &= 0\end{aligned}$$

and (A3)

$$\begin{aligned}(E_{y2}, H_{x2}) &\neq 0\\ (E_{x2}, H_{y2}) &= 0.\end{aligned}$$

Thus equations (A2) reduce to

$$\partial Z_{xx}/\partial m_k = 0$$

$$\partial Z_{xy}/\partial m_k = \{H_{y1}\partial E_{x1}/\partial m_k - E_{x1}\partial H_{y1}/\partial m_k\}/\, H_{y1}^2$$

$$\partial Z_{yx}/\partial m_k = \{H_{x2}\partial E_{y2}/\partial m_k - E_{y2}\partial H_{x2}/\partial m_k\}/\, H_{x2}^2 \qquad \text{(A4)}$$

$$\partial Z_{yy}/\partial m_k = 0,$$

which are identical to expressions derived directly for the 2D MT problem.

The model sensitivities in equation (A2) involve partial derivatives of the electric and magnetic fields. Following the derivation of Newman & Alumbaugh (1997) we can relate these derivatives to the forward problem. Consider as an example the x-component of the magnetic field at location j for a given source polarization, which can be represented as

$$H_{xj} = {}^{h}\mathbf{g}^{T}_{j(x)}\mathbf{E}. \qquad \text{(A5)}$$

In this expression $\mathbf{E}$ is an electric field vector arising from a 3D earth model for a specific source polarization and has dimension of NTx1, where NT represents the number of electric field unknowns that are determined from the finite difference forward solution. The vector ${}^{h}\mathbf{g}^{T}_{j(x)}$ is an interpolator vector for the x-component of the magnetic field at the jth measurement point and is of dimension 1xNT (T here denotes the transpose operator). This vector will interpolate the sampled fields on the forward modeling grid to the measurement point and numerically includes a curl operator that is applied to the electric field. With this definition an element of the Jacobian matrix is written for x-component of magnetic field as

$$\partial H_{xj}/\partial m_k = {}^{h}\mathbf{g}^{T}_{j(x)}\,\partial\mathbf{E}/\partial m_k. \qquad \text{(A6)}$$

From the forward problem, the electric fields are determined from the linear system given by equation (2). Thus differentiating equation (2) with respect to m_k yields,

$$\partial\mathbf{E}/\partial m_k = -\mathbf{K}^{-1}(\partial\mathbf{K}/\partial m_k\mathbf{E}), \qquad \text{(A7)}$$

and an element of the Jacobian matrix for the x-component of magnetic field is written as

$$\partial H_{xj}/\partial m_k = -\,{}^{h}\mathbf{g}^{T}_{j(x)}\;\mathbf{K}^{-1}(\,\partial\mathbf{K}/\partial m_k\mathbf{E}). \qquad \text{(A8)}$$

Similar expressions can be derived for the other electric and magnetic field components.

Using the above results, terms involving the electric and magnetic field partial derivatives can be substituted for in equation (A2) to yield

$$\begin{aligned}
\partial Z_{xxj}/\partial m_k &= -{}^1\mathbf{g}_j^T{}_{xx}\,\mathbf{K}^{-1}(\partial\mathbf{K}/\partial m_k\mathbf{E}_1) - {}^2\mathbf{g}_j^T{}_{xx}\,\mathbf{K}^{-1}(\partial\mathbf{K}/\partial m_k\mathbf{E}_2)\\
\partial Z_{xyj}/\partial m_k &= -{}^1\mathbf{g}_j^T{}_{xy}\,\mathbf{K}^{-1}(\partial\mathbf{K}/\partial m_k\mathbf{E}_1) - {}^2\mathbf{g}_j^T{}_{xy}\,\mathbf{K}^{-1}(\partial\mathbf{K}/\partial m_k\mathbf{E}_2)\\
\partial Z_{yxj}/\partial m_k &= -{}^1\mathbf{g}_j^T{}_{yx}\,\mathbf{K}^{-1}(\partial\mathbf{K}/\partial m_k\mathbf{E}_1) - {}^2\mathbf{g}_j^T{}_{yx}\,\mathbf{K}^{-1}(\partial\mathbf{K}/\partial m_k\mathbf{E}_2)\\
\partial Z_{yyj}/\partial m_k &= -{}^1\mathbf{g}_j^T{}_{yy}\,\mathbf{K}^{-1}(\partial\mathbf{K}/\partial m_k\mathbf{E}_1) - {}^2\mathbf{g}_j^T{}_{yy}\,\mathbf{K}^{-1}(\partial\mathbf{K}/\partial m_k\mathbf{E}_2),
\end{aligned} \tag{A9}$$

where $\mathbf{E}_1$ and $\mathbf{E}_2$ are the two electric field polarizations needed to define the impedance tensor and

$$\begin{aligned}
{}^1\mathbf{g}_j^T{}_{xx} &= \{(H_{x1}H_{y2} - H_{x2}H_{y1})(-H_{y2}\,{}^e\mathbf{g}^T{}_{j(x)} + E_{x2}\,{}^h\mathbf{g}^T{}_{j(y)}) +\\
&\quad (E_{x1}H_{y2} - E_{x2}H_{y1})(-H_{x2}\,{}^h\mathbf{g}^T{}_{j(y)} + H_{y2}\,{}^h\mathbf{g}^T{}_{j(x)})\}/(H_{x1}H_{y2} - H_{x2}H_{y1})^2\\
{}^2\mathbf{g}_j^T{}_{xx} &= \{(H_{x1}H_{y2} - H_{x2}H_{y1})(-E_{x1}\,{}^h\mathbf{g}^T{}_{j(y)} + H_{y1}\,{}^e\mathbf{g}^T{}_{j(x)}) +\\
&\quad (E_{x1}H_{y2} - E_{x2}H_{y1})(-H_{y1}\,{}^h\mathbf{g}^T{}_{j(x)} + H_{x1}\,{}^h\mathbf{g}^T{}_{j(y)})\}/(H_{x1}H_{y2} - H_{x2}H_{y1})^2\\
{}^1\mathbf{g}_j^T{}_{xy} &= \{(H_{x1}H_{y2} - H_{x2}H_{y1})(-E_{x2}\,{}^h\mathbf{g}^T{}_{j(x)} + H_{x2}\,{}^e\mathbf{g}^T{}_{j(x)}) +\\
&\quad (E_{x2}H_{x1} - E_{x1}H_{x2})(-H_{x2}\,{}^h\mathbf{g}^T{}_{j(y)} + H_{y2}\,{}^h\mathbf{g}^T{}_{j(x)})\}/(H_{x1}H_{y2} - H_{x2}H_{y1})^2\\
{}^2\mathbf{g}_j^T{}_{xy} &= \{(H_{x1}H_{y2} - H_{x2}H_{y1})(-H_{x1}\,{}^e\mathbf{g}^T{}_{j(x)} + E_{x1}\,{}^h\mathbf{g}^T{}_{j(x)}) +\\
&\quad (E_{x2}H_{x1} - E_{x1}H_{y2})(-H_{y1}\,{}^h\mathbf{g}^T{}_{j(x)} + H_{x1}\,{}^h\mathbf{g}^T{}_{j(y)})\}/(H_{x1}H_{y2} - H_{x2}H_{y1})^2
\end{aligned} \tag{A10}$$

$$\begin{aligned}
{}^1\mathbf{g}_j^T{}_{yx} &= \{(H_{x1}H_{y2} - H_{x2}H_{y1})(-H_{y2}\,{}^e\mathbf{g}^T{}_{j(y)} + E_{y2}\,{}^h\mathbf{g}^T{}_{j(y)}) +\\
&\quad (E_{y1}H_{y2} - E_{y2}H_{y1})(-H_{x2}\,{}^h\mathbf{g}^T{}_{j(y)} + H_{y2}\,{}^h\mathbf{g}^T{}_{j(x)})\}/(H_{x1}H_{y2} - H_{x2}H_{y1})^2\\
{}^2\mathbf{g}_j^T{}_{yx} &= \{(H_{x1}H_{y2} - H_{x2}H_{y1})(-E_{y1}\,{}^h\mathbf{g}^T{}_{j(y)} + H_{y1}\,{}^e\mathbf{g}^T{}_{j(y)}) +\\
&\quad (E_{y1}H_{y2} - E_{y2}H_{y1})(-H_{y1}\,{}^h\mathbf{g}^T{}_{j(x)} + H_{x1}\,{}^h\mathbf{g}^T{}_{j(y)})\}/(H_{x1}H_{y2} - H_{x2}H_{y1})^2\\
{}^1\mathbf{g}_j^T{}_{yy} &= \{(H_{x1}H_{y2} - H_{x2}H_{y1})(-E_{x2}\,{}^h\mathbf{g}^T{}_{j(x)} + H_{x2}\,{}^e\mathbf{g}^T{}_{j(x)}) +\\
&\quad (E_{y2}H_{x1} - E_{y1}H_{x2})(-H_{x2}\,{}^h\mathbf{g}^T{}_{j(y)} + H_{y2}\,{}^h\mathbf{g}^T{}_{j(x)})\}/(H_{x1}H_{y2} - H_{x2}H_{y1})^2\\
{}^2\mathbf{g}_j^T{}_{yy} &= \{(H_{x1}H_{y2} - H_{x2}H_{y1})(-H_{x1}\,{}^e\mathbf{g}^T{}_{j(y)} + E_{y1}\,{}^h\mathbf{g}^T{}_{j(x)}) +\\
&\quad (E_{y2}H_{x1} - E_{y1}H_{x2})(-H_{y1}\,{}^h\mathbf{g}^T{}_{j(x)} + H_{x1}\,{}^h\mathbf{g}^T{}_{j(y)})\}/(H_{x1}H_{y2} - H_{x2}H_{y1})^2
\end{aligned}$$

The eight vectors in equation (A10) can be interpreted as generalized interpolator vectors, which involve linear combinations of vectors which interpolate the electric and magnetic fields from the forward modeling grid to the receiver at location j. These latter vectors are weighted by the combinations of electric and magnetic fields produced by the different source polarizations.

APPENDIX B

The line search algorithm

The line search procedure is to find α such that $\varphi(\mathbf{m} + \alpha\mathbf{u})$ is sufficiently decreased along the search direction, $\mathbf{u}$. Quadratic curve fitting is also employed in an attempt to refine α so that an even greater reduction in φ is possible. To determine α let us first normalize $\mathbf{u}$, so that

$$\mathbf{v} = \mathbf{u} / \| \mathbf{u} \|, \tag{B1}$$

where $\| \mathbf{u} \|$ is the Euclidean length and define $\alpha' = \|\mathbf{u}\| \alpha$. The parameter α' has the dimension of S/m, whereas α is dimensionless. We are now required to find α' such that $\varphi(\mathbf{m} + \alpha'\mathbf{v})$ is sufficiently decreased along the search direction, $\mathbf{v}$. Thus, the critical condition that α' must satisfy is

$$\varphi(\mathbf{m} + \alpha'\mathbf{v}) < \varphi(\mathbf{m}) + \delta\, \alpha'\, \nabla\varphi\,(\mathbf{m}) \cdot \mathbf{v}, \tag{B2}$$

where δ is a small positive constant that insures a sufficient decrease in $\varphi(\mathbf{m} + \alpha'\mathbf{v})$. The test in equation (B2) is necessary since the simpler test,

$$\varphi(\mathbf{m} + \alpha'\mathbf{v}) < \varphi(\mathbf{m}), \tag{B3}$$

can lead to the possibility of oscillation about the solution without convergence (Dennis & Schnabel, 1996). In choosing δ we follow recent optimization literature and set $\delta = 10^{-4}/\alpha'$. To launch the procedure we need to select a trial value for α' and carry out the test required by equation (B2).

Unlike Newton and quasi Newton methods, which accept a unit step ($\alpha' = 1$) most of the time, it is common to see step lengths that vary by one to two orders of magnitude with NLCG methods (Nocedal, 1996). Therefore, we resort to a heuristic approach, which works well in practice for our problem. For the the k_{th} model parameter, m_k, and its perturbed value, $m_k + \Delta m_k$, for some point along the descent direction, $\mathbf{v}$, we have from equation (21) that

$$m_k = m_o\, e^{m'_k} + lb_k \tag{B4}$$

and

$$m_k + \Delta m_k = m_o e^{m'_k + \Delta m'_k} + lb_k. \tag{B5}$$

Subtracting equation (B5) from (B4) produces

$$\Delta m_k = m_o e^{m'_k} (e^{\Delta m'_k} - 1), \tag{B6}$$

and solving for $\Delta m'_k$ yields

$$\Delta m'_k = \ln \{ (\Delta m_k / m_o) e^{-m'_k} + 1 \}, \tag{B7}$$

where "ln" denotes the natural logarithm. By selecting the model parameter, m_{max}, that corresponds to the largest component in **v** that satisfies the infinity norm,

$$\|\mathbf{v}\|_\infty = \max_{1 \le i \le M} |v_i|. \tag{B8}$$

we define the trial step based on equation (B7) to be

$$\alpha'_{trial} = \ln\{(1.6 m_{max}/m_o) e^{-m'_{max}} + 1\}, \tag{B9}$$

where, m_{max} changes by a factor of 1.6 . The factor 1.6 is empirical and is based upon the numerical experiments, which always demonstrated a sufficient decrease in the cost functional (equation (B2)).

If equation (B2) is satisfied with α'_{trial}, let $f_o = \varphi(\mathbf{m})$ and $f_1 = \varphi(\mathbf{m} + \alpha'_{trial}\mathbf{v})$ and employ a quadratic model to find an α' that leads to an even greater reduction in f. Four pieces of information are required to define the quadratic: the two functional values $\varphi(\mathbf{m})$ and $\varphi(\mathbf{m}+\alpha'_{trial}\mathbf{v})$, α'_{trial}, and the directional derivative $g_o = \nabla\varphi(\mathbf{m}).\mathbf{v}$. Note that the directional derivative and functional at the point **m** are available from the prior NLCG iteration at no additional cost. Thus, if f_{min} defines the functional minimum we are seeking, then

$$f(x) = f_{min} + b\,(x - \alpha')^2/\alpha'^2_{trial} \tag{B10}$$

where,

$$b = (f_1 - f_o) - g_o\,\alpha'_{trial}, \tag{B11}$$

then the candidate step is given by

$$\alpha' = -g_o\alpha'^2_{trial}/2b < \alpha'_{max}. \tag{B12}$$

Here α'_{max} sets an upper bound on the step, such that $\mathbf{m} + \alpha'\mathbf{v}$ leads to a realizable model and does not leave the domain of interest. For the step in equation (B12) to be acceptable two conditions must be meet. The first is $b>0$, which insures that the quadratic model has positive curvature and α' defines its minimum and not its maximum and the second that $f(\alpha')$ is in actually less than f_1 by explicitly computing $\varphi(\mathbf{m} + \alpha'\mathbf{v})$. If $b < 0$ or if $f_1 < f(\alpha')$, we set $\alpha' = \alpha'_{trial}$ and exit the line search algorithm since we have already determined that α'_{trial} leads to a sufficient decrease in $\varphi(\mathbf{m} + \alpha'\mathbf{v})$.

If at the trial step, f_1, fails to satisfy equation (B2), a quadratic backtracking strategy is invoked from α'_{trial} until a sufficient decrease in f is observed. Backtracking is effective because **v** is a descent direction since $g_o = \mathbf{v} \cdot \nabla\varphi < 0$ at $\varphi(\mathbf{m})$. The quadratic formula used to backtrack is given by

$$f(x) = f_o + g_o\,x + cx^2, \tag{B15}$$

where

$$c = (f_1 - f_o - g_o \alpha'_{trial})/\alpha'^2_{trial} \tag{B16}$$

and the candidate step is determined to be

$$\alpha' = \frac{-g_o \alpha'^2_{trial}}{2(f_1 - f_o - g_o \alpha'_{trial})}. \tag{B17}$$

Note that the curvature, c, in equation (B16) is always positive, hence the quadratic model will always interpolate to a minimum. For α' to be acceptable, we must verify that equation (B2) is satisfied. If not, we set $\alpha'_{trial} = \alpha'$ and continue backtracking until an acceptable step is found.

A danger of estimating α' using any type of polynomial approximation is that α' may be too near zero to be of much use in reducing φ and the inverse solution can stagnate as a result. Polynomial *safeguarding* prevents against this (cf., Dennis & Schnabel, 1996). When $\alpha' < 0.1\alpha'_{trial}$, in any of the quadratic modeling procedures discussed above, we always set $\alpha' = 0.1\ \alpha'_{trial}$.

APPENDIX C

Preconditioning for 3D EM scattering problems

A fast preconditioner has been developed at low induction numbers to accelerate the convergence rate for solving the electromagnetic (EM) scattering problems with finite difference methods using iterative Krylov methods. We demonstrate a reduction of up too two orders of magnitude in the number of iterations and an order of magnitude speed up in time needed to solve a series of test problems. The preconditioner is very effective over a wide class of EM measurement configurations ranging from magnetotellurics to induction logging. Simple relations have also been developed to show when the preconditioner will be effective.

Over the last ten years finite difference methods using iterative Kyrlov methods have become a popular method for solving large scale 3D electromagnetic induction problems (Druskin et. al., 1998; Druskin and Knizhnerman, 1988 and 1994; Newman and Alumbaugh, 1995; Smith 1996; Alumbaugh et al; 1996). From these works, it has been established that iterative solution becomes more computer intensive as frequency falls due to ill conditioning of the underlying linear system used to approximate the 3D electromagnetic (EM) wave equation. For magnetotelluric applications, Smith 1996, demonstrated that the ill conditioning could be overcome using a static divergence correction that periodically reinforces the conservation of current during the solution process. Recently Druskin et al. 1998, developed a new spectral Lanczos decomposion method with Krylov subspaces generated from the inverse powers of the Maxwell

operator to overcome the problem for well logging applications. Here we consider the problem from a preconditioning point of view to provide an alternative solution, which we believe is easier to understand than the previous approaches and leads to a deeper understanding of the problem. Our solution is also applicable to a wider class of induction modeling problems and we provide some simple measures when it will be effective.

The three dimensional electromagnetic wave equation

Our development begins with the 3D EM wave equation for the electric field, where

$$\nabla \mathbf{x} \nabla \mathbf{x} \mathbf{E} + i\omega \mu_o \sigma \mathbf{E} = -i\omega \mathbf{J}; \qquad \text{(C1)}$$

note that this equation will reduce to the standard Helmholtz equation when the electric field is divergence free. In equation (C1), the electrical conductivity, σ, is a three-dimensional function of the spatial coordinates, μ_o is the magnetic permeability of free space, ω is the angular frequency and $i = \sqrt{-1}$. For controlled source applications, **J** is the impressed source used to excite the fields, where Dirichlet boundary conditions are used to set the tangential component of the electric field, **E**, to zero on the boundaries of the modeling domain. For magnetotelluric applications, **J** is set to zero, and appropriate Dirichlet boundary conditions are the tangential electric-field boundary values defined by the source field polarization. These boundary values arise from plane waves propagating in layered or 2D geologic media assigned at the boundaries of the 3D problem. The modeling problem can be summarized as solving for the electric fields within prism in Figure 2, given appropriate boundary conditions and source field excitation **J**.

When equation (C1) is approximated with (non-uniform) finite differences using a Yee (1966) staggered grid a linear system results where,

$$\mathbf{K}\,\mathbf{E} = \mathbf{S}. \qquad \text{(C2)}$$

The matrix **K** is complex-symmetric and sparse with 13 non-zero entries per row and **S** comprises the right hand side in equation (C1) and also includes the appropriate boundary conditions on the discrete electric field. It has been determined that at the higher frequencies, this system can be efficiently solved using the quasi-minimum residual (qmr) method, which belongs to the class of Krylov sub-space techniques that are highly efficient in iteratively solving sparse linear systems. It is well known, however, (cf. Alumbaugh et al., 1996; Smith, 1996) that difficulties will be encountered when attempts are made to solve equation (C2) as frequencies approach the static limit. Similar difficulties have been reported by Druskin et al. (1998) when finite difference approximations and the spectral Lanczos methods are applied directly to equation (1) for multiple frequency responses.

Divergence and curl free projections of the electric field

Following, LaBrecque, (1995) and Druskin et. al. (1998), we assume that the electric field can be decomposed into curl free and divergence free projections using the Helmholtz theorem, where

$$\mathbf{E} = \zeta + \nabla\varphi, \tag{C3}$$

and

$$\nabla \cdot \zeta = 0. \tag{C4}$$

Upon substitution into equation (C1) we find that

$$-\nabla^2 \zeta + i\omega\,\mu_o\,\sigma(\zeta + \nabla\varphi) = -i\omega\,\mu_o\,\mathbf{J}, \tag{C5}$$

where we used the vector identity

$$\nabla \mathbf{x} \nabla \mathbf{x} \mathbf{E} = -\nabla^2 \zeta, \tag{C6}$$

since $\nabla \cdot \zeta = 0$ and $\nabla \mathbf{x} \nabla \mathbf{x} \nabla\varphi = \mathbf{0}$. The key idea behind the splitting of the electric field into curl free and divergence free projections is to deflate the null space of the curl-curl operator. When Krylov methods are applied directly to equation (C2), this null space is responsible for the poor convergence properties as frequency approaches the static limit. It is also responsible for the spurious mode problem, where the gradient of a scalar potential can be added to the electric field and still satisfy equation (C1), when the frequency is sufficiently small.

Approximate solutions at low frequencies

To develop an approximate finite difference solutions to equations (C1 and thus C2) at low frequencies we take the Euclidean norm of equation (C1) where

$$(1/\Delta^2 + \omega\,\mu_o\,\sigma)\,\|\mathbf{E}\|^2 \geq \|\,\nabla \mathbf{x} \nabla \mathbf{x} \mathbf{E} + i\omega\,\mu_o\,\sigma\,\mathbf{E}\,\|^2. \tag{C7}$$

Here Δ is the characteristic grid size employed in the finite difference mesh. Thus the following inequality is deduced from the first factor in equation (C7) as frequency falls and the grid size is reduced,

$$1 >> \Delta^2\,\omega\,\mu_o\,\sigma_{max}, \tag{C8}$$

where σ_{max} is the maximum conductivity in the mesh. When the finite difference grid is non-uniform, Δ should be replaced by Δ_{max}, the maximum grid size used to approximate equation (1). Note that the right hand side of equation (C8) is dimensionless number and its square root is an induction number, which is an invariant parameter for diffusive electromagnetic fields; when frequency falls we increase the scale length and/or conductivity accordingly to have the fields remain invariant. Thus it appears that the induction number is more important in determining when equation (C8) holds more so

than frequency alone. It is important to note that even at moderate frequencies equation (C8) may still hold if the grid size needed for the problem is sufficiently small. Now when equation (C8) is satisfied we can decouple equation (C5), such that

$$-\nabla^2 \zeta = -i\omega \mathbf{J}. \tag{C9}$$

Druskin et al., (1998), shows that the boundary conditions required to solve equation (C9) are a mixture of Dirichlet and Neumann types. Dirichlet conditions are applied to the tangential components of ζ on the mesh boundaries and Neumann conditions on the normal components.

ζ is not a complete solution to Maxwell's equations since it does not satisfy the auxiliary divergence conditions on the current density with in the earth and the divergence free conditions of the electric field in the air. To derive these conditions we take the divergence of equation (C1) and substitute in equation (C3) to arrive at

$$\nabla \cdot \sigma(\nabla\varphi) = -\nabla \cdot \sigma(\zeta) - \nabla \cdot \mathbf{J} \tag{C10}$$

for the current density in the earth. In the air, assuming $\nabla \cdot \mathbf{E} = 0$, the corresponding divergence condition becomes in the limit as $\sigma \rightarrow 0$,

$$\nabla \cdot \nabla\varphi = -\nabla \cdot \zeta. \tag{C11}$$

In equation (C4) we have assumed that $\nabla \cdot \zeta = 0$. However in the numerical realization of ζ it is in general not divergence free due to numerical round off errors. While this error is not critical in the earth it can be in the air. We therefore consider the right hand side in equation (C11) to be a correction term which is necessary to enforce the electric field to be divergence free in the air; namely $\nabla \cdot \mathbf{E} = 0$. Two types of boundary conditions apply to equation (C10) depending whether air is present. When it is not, we have the Dirichlet conditions, where φ=0 on the mesh boundaries. When the air-earth interface is present, however, we employ the Neumann condition, $\partial\varphi/\partial n = 0$, where n specifies the direction normal at the interface. Finally, the boundary conditions on equation (C11) are of the Dirichlet type, where φ=0 on the mesh boundaries and $\varphi = \varphi_{interface}$ at the air-earth interface. Note that $\varphi_{interface}$ is provided by the solution of equation (C10). It is noteworthy that when $\mathbf{J} = \mathbf{0}$ and $\zeta = \mathbf{E}$ as given in equation (C1), equations (C10) and (C11) replicate the static divergence correction of Smith (1996) that was applied to accelerate the convergence rate of equation (C1) for magnetotelluric applications at low frequencies.

Given equation (C8), approximate solutions of the full 3D EM wave equation (equation (C2)) can be obtained by first solving equation (C9) followed by equation (C10). Depending if air-earth interface is present, we would also solve equation (C11). Solution to these equations can be efficiently obtained using finite difference methods with conjugate gradient methods to iteratively solve the systems to predetermined errors.

Preconditioning

If it turns out that we cannot obtain a good approximate solution to equation (C2) with a reasonable number of Krylov subspace iterations, or if such an approximate

solution cannot be easily computed, we consider modifying the original problem to obtain a faster solution. This is the idea behind preconditioning, where we specify a preconditioning matrix, $\mathbf{M}$,and effectively solve the modified problem

$$\mathbf{M}^{-1}\mathbf{K}\,\mathbf{E}=\mathbf{M}^{-1}\mathbf{S}'. \qquad \text{(C12)}$$

At each step of the preconditioned algorithm, it is necessary to compute the product of $\mathbf{M}^{-1}$ with a vector, or, equivalently, to solve a linear system with the coefficient matrix $\mathbf{M}$, so $\mathbf{M}$ should be chosen so that such linear systems are much easier to solve than the original problem. Moreover, the properties we desire in a preconditioner for non-Hermitian matrix iterations, including qmr and other related methods, are that the preconditioned matrix should somehow approximate the identity (Greenbaum, 1997). It is therefore obvious that the approximate scheme discussed above could be very effective in preconditioning equation (C2) at moderate to low induction numbers. If this idea is to be practical, however, it will be necessary to find fast methods to solve the approximate equations. A good preconditioner is not simply based on a relatively low dimensional Krylov subspace, but on the time required to construct it.

Implementation of the low induction number (LIN) preconditioner is straight forward. We first convert equations (C9), (C10) and (C11) into discrete matrix equations via staggered finite differences. In the preconditioned qmr algorithm, at each iteration, we then substitute the source vector used to solve the linear system involving the coefficient matrix $\mathbf{M}$, into the right hand side of the discrete version of equation (C9). Equation (C9) is then solved followed by equations (C10) and (C11). Fast preconditioned conjugate gradient techniques employing incomplete Cholesky factorization have proven quite effective in solving these equations. Furthermore we have determined that it is not necessary to precisely solve these equations. It is only necessary to solve these equations approximately.

Measuring the effectiveness of the preconditioner

Equation (C8) provides only a rough measure on the effectiveness of the preconditioner. We need to estimate the largest and smallest non-zero eigenvalue of the discrete curl-curl operator to determine when the preconditioner will be the most and least effective. Consider the equation (C2), when $\sigma = 0$. We estimate the maximum row sum as

$$\lambda_{max} \approx 13/\Delta_{min}^{2}, \qquad \text{(C13)}$$

where Δ_{min} is the minimum grid size used in the mesh. The corresponding minimum eigenvalue is estimated in Appendix D, where

$$\lambda_{min} \approx 2\pi^{2}/L_{max}^{2}, \qquad \text{(C14)}$$

with L_{max} as the largest dimension of the prismatic modeling domain.

Given the largest eigenvalue, the inequality in equation (C8) becomes

$$1 >> \omega \mu_o \sigma_{max} \Delta_{min}^2 / 13, \qquad \text{(C15)}$$

which provides the optimistic case when the preconditioner will be most effective. In the worst case, which corresponds to the smallest non-zero eigenvalue, we have, however,

$$1 >> \omega \mu_o \sigma_{max} L_{max}^2 / 2\pi^2. \qquad \text{(C16)}$$

Unfortunately, equation (C16) shows that reducing the grid size (Δ) does not provide any additional benefit in accelerating the solution of equation (C12).

It is well known that Krylov methods tend to first resolve solution components related to eigenvectors with the largest eigenvalues of the finite-difference stiffness matrix **K**. As frequency falls these eigenvalues will correspond closely to those of the curl-curl operator. If only the large eigenvalues are needed to produce an accurate solution to the problem, then the inequality in equation (C15) will provide a good measure on the effectiveness of the preconditioner. On the other hand, if eigenvectors corresponding to the smallest non-zero eigenvalues are necessary to capture the solution, then equation (C16) would provide a better measure.

Demonstration of the preconditioner

In Figure. 34 we demonstrate the preconditioner effectiveness at 4 Hz for the test model shown in Figure 3. A speed up of more than a factor of ten is demonstrated compared to preconditioning employing simple Jacobi preconditioning. When the new preconditioning method is compared with the static-divergence correction procedure of Smith (1996), the solution time is still a factor of three faster. When the frequency is increased to 400 Hz, Figure 35 shows that the preconditioner is still effective, but its benefits are not nearly as great, as expected from our prior analysis.

APPENDIX D

Estimate of the smallest non-zero eigenvalue of the discrete curl-curl operator

First, consider the curl-curl operator in the continuous case,

$$\nabla \mathbf{x} \nabla \mathbf{x} \mathbf{v} = \lambda \mathbf{v}, \qquad \text{(D1)}$$

where $\mathbf{v}$ and λ are the corresponding eigenvector and eignevlaue pairs. If we apply the divergence operator to equation (D1) we immediately see that

$$0 = \lambda \nabla \cdot \mathbf{v}. \qquad \text{(D2)}$$

Since we are interested in the case where $\lambda \neq 0$, we conclude that

$$\nabla \cdot \mathbf{v} = 0. \qquad \text{(D3)}$$

Thus the eigenvalue problem can be simplified to

$$-\nabla^2 \mathbf{v} = \lambda \mathbf{v} \tag{D4}$$

where we seek solutions to this problem where the eigenvector **v** is divergence free. When we consider the discrete case, we need to impose boundary conditions on **v**, where its tangential components vanish on boundaries of the modeling grid. Specifically

$$\mathbf{n} \times \mathbf{v} = \mathbf{0}, \tag{D5}$$

where **n** is the unit outward normal. Candidate eigenfunctions that satisfy the boundary conditions requirements are

$$\begin{aligned} v_x &= A\cos(\alpha x)\sin(\beta y)\sin(\delta z), \\ v_y &= B\sin(\alpha x)\cos(\beta y)\sin(\delta z) \\ \text{and} \qquad & \qquad (D6) \\ v_z &= C\sin(\alpha x)\sin(\beta y)\cos(\delta z), \end{aligned}$$

where $\alpha = \pi/L_x$, $\beta = \pi/L_y$ and $\delta = \pi/L_z$ where L_x, L_y and L_z are the dimensions of the modeling domain in the x, y and z directions indicated in Figure 1. A, B and C are not arbitrary coefficients in equation (D6) because $\nabla \cdot \mathbf{v} = 0$. Thus, once two components of **v** are specified, the final component must be selected such that **v** is divergence free. For example, if $A=\beta\delta$ and $B=\alpha\delta$ then $C=-2\alpha\beta$.

If we consider the discrete version of equation (D4) on a mesh with uniform grid size Δ, one can show that with discrete version of equation (D6) that

$$\lambda = 4/\Delta^2(\sin^2(l\pi\Delta/2L_x) + \sin^2(m\pi\Delta/2L_y) + \sin^2(n\pi\Delta/2L_z)). \tag{D7}$$

The range of the indices l, m and n are

$$\begin{aligned} l &= 0,1,\ldots,N_x \\ m &= 0,1,\ldots,N_y \\ \text{and} \qquad & \\ n &= 0,1,\ldots,N_z, \end{aligned}$$

where $L_x = \Delta s\, N_x$, $L_y = \Delta s\, N_y$ and $L_z = \Delta s\, N_z$. To estimate the smallest non-zero value λ, we set L_x , L_y and L_z to the largest dimension of the prism in Figure 1; L_{max}. Now if we select one of the indices, l, m or n to be zero and the others to be one (here we arbitrarily set $l=0$, and $m=1$ and $n=1$) and employ a small argument expression for the sin function ($\sin(x) \approx x$, when $x \to 0$), we find an estimate of the smallest non-zero eigenvalue to be

$$\lambda_{min} \approx 2\pi^2 / L_{max}^2. \tag{D8}$$

Note that we can not set two of the indices to be zero in equation (D7) as this would result in a zero eigenvector, which is a trivial solution to the eigenvalue problem.

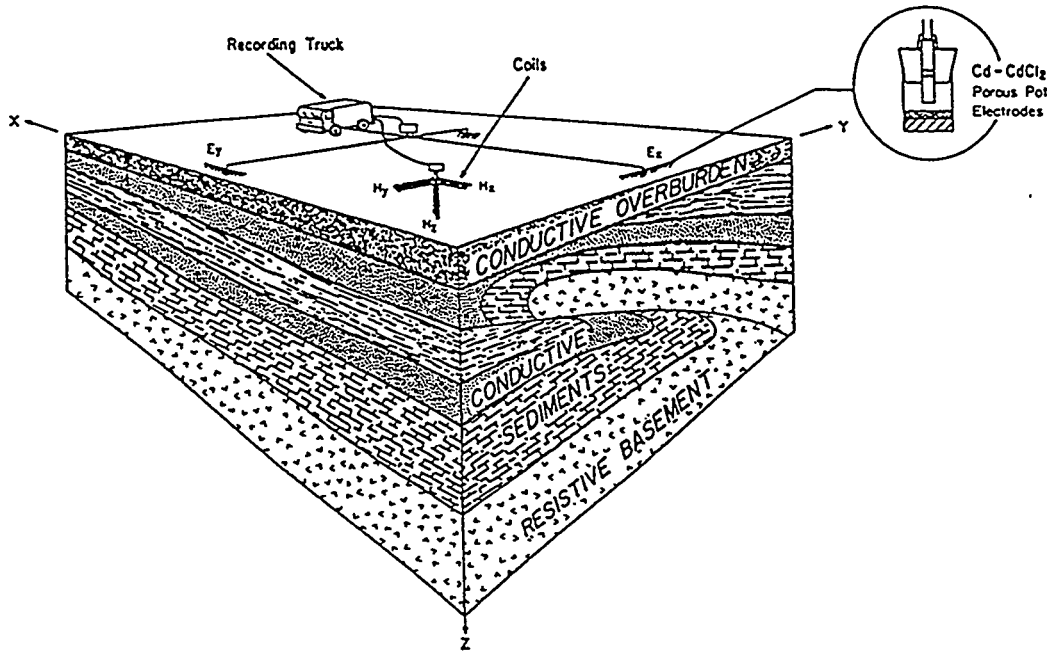
Recording Truck
Coils
Cd - CdCl2
Porous Pot
Electrodes
X
Y
Z
Ey
Ex
Hy
Hx
Hz
CONDUCTIVE OVERBURDEN
CONDUCTIVE SEDIMENTS
RESISTIVE BASEMENT

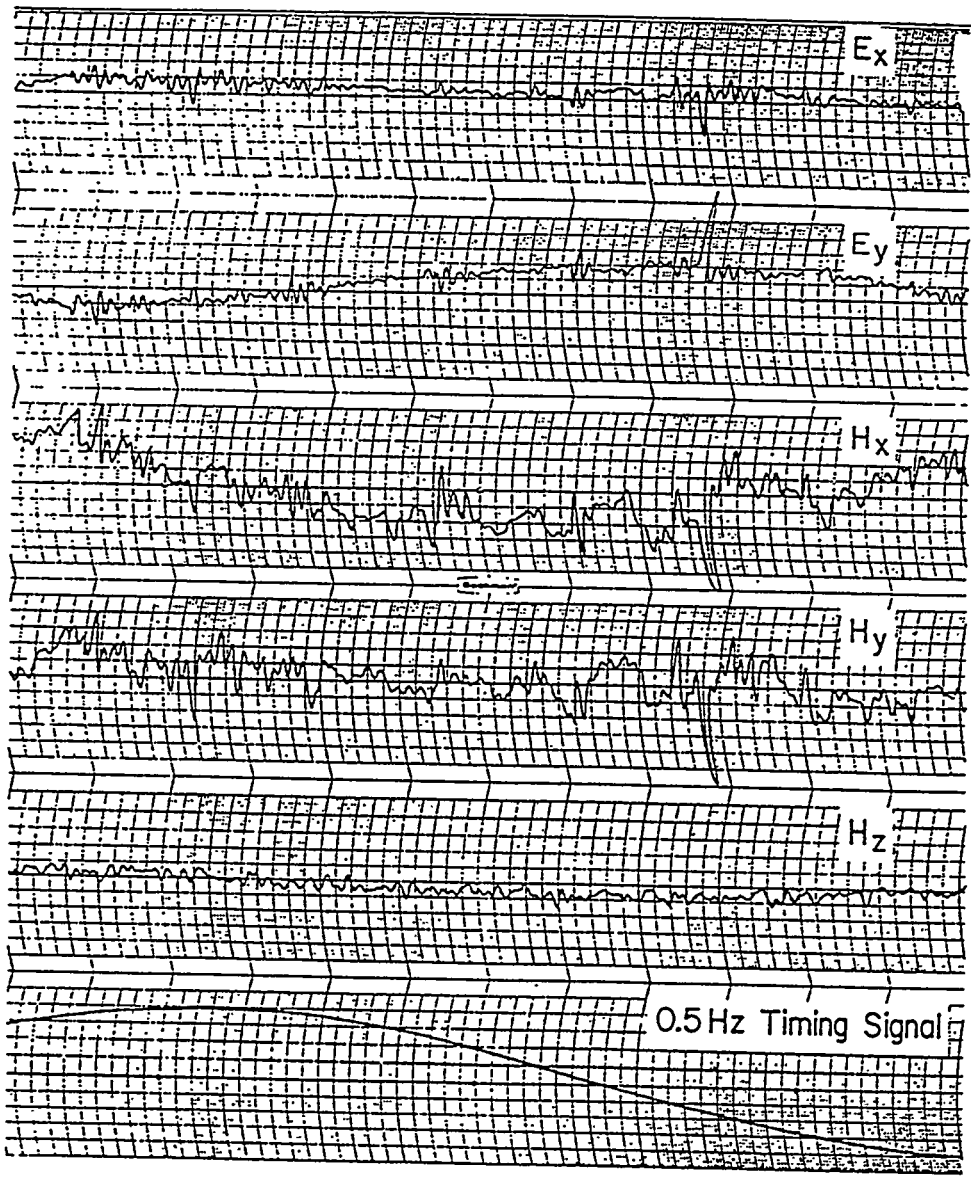
Ex
Ey
Hx
Hy
Hz
0.5 Hz Timing Signal

Figure 1

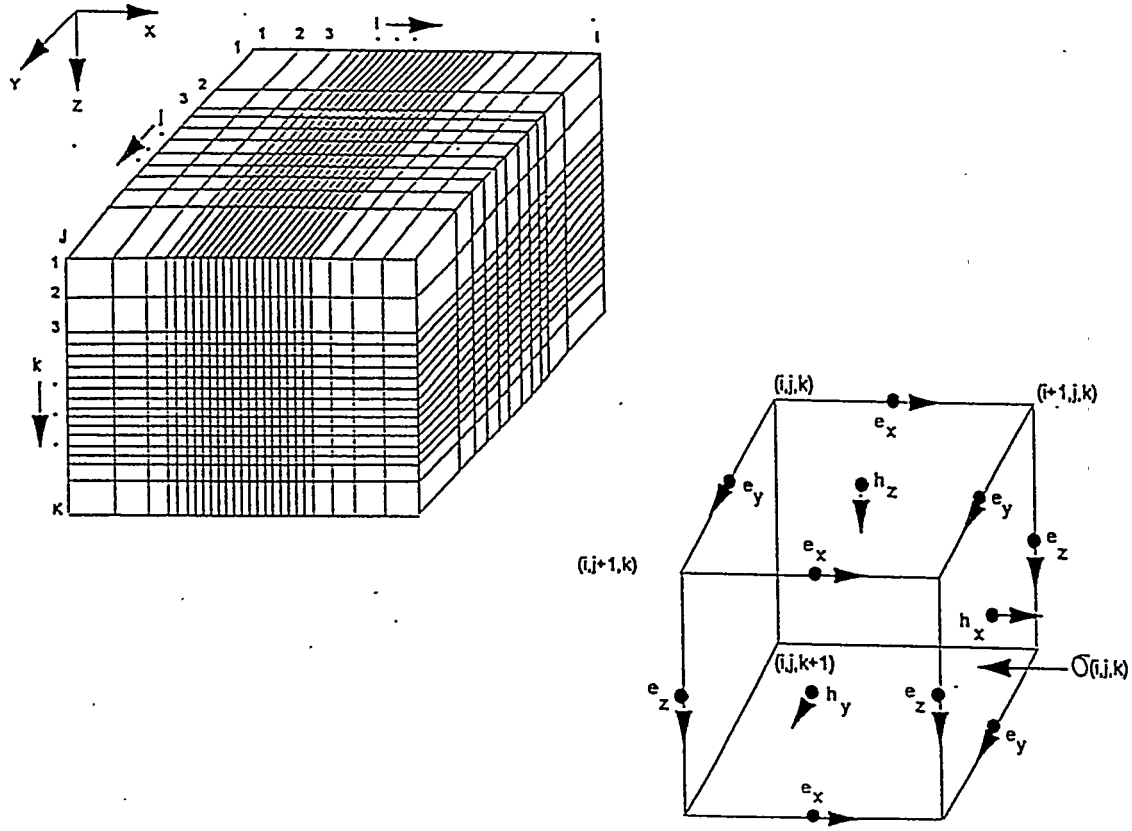

Figure 2

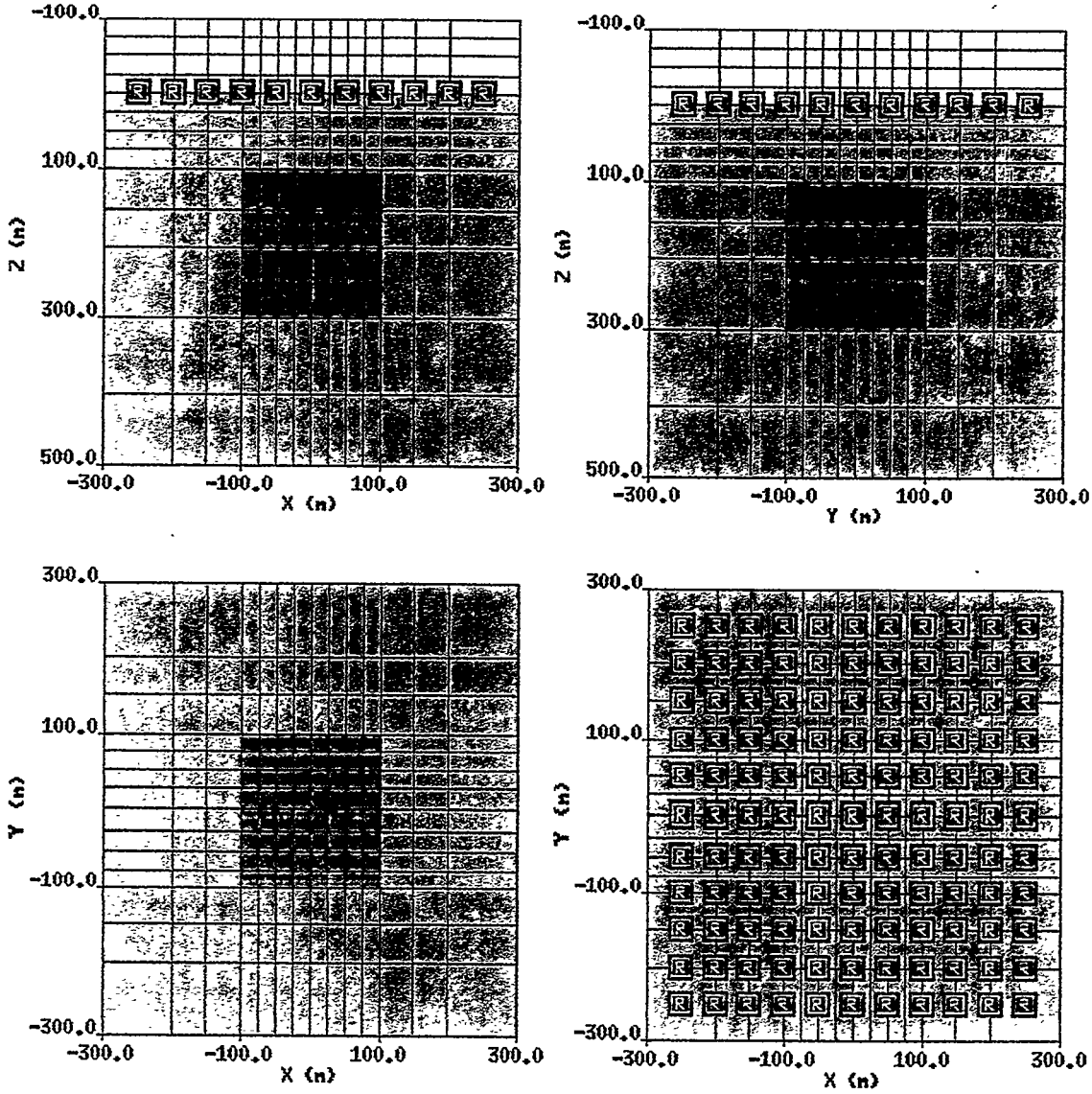

Figure 3

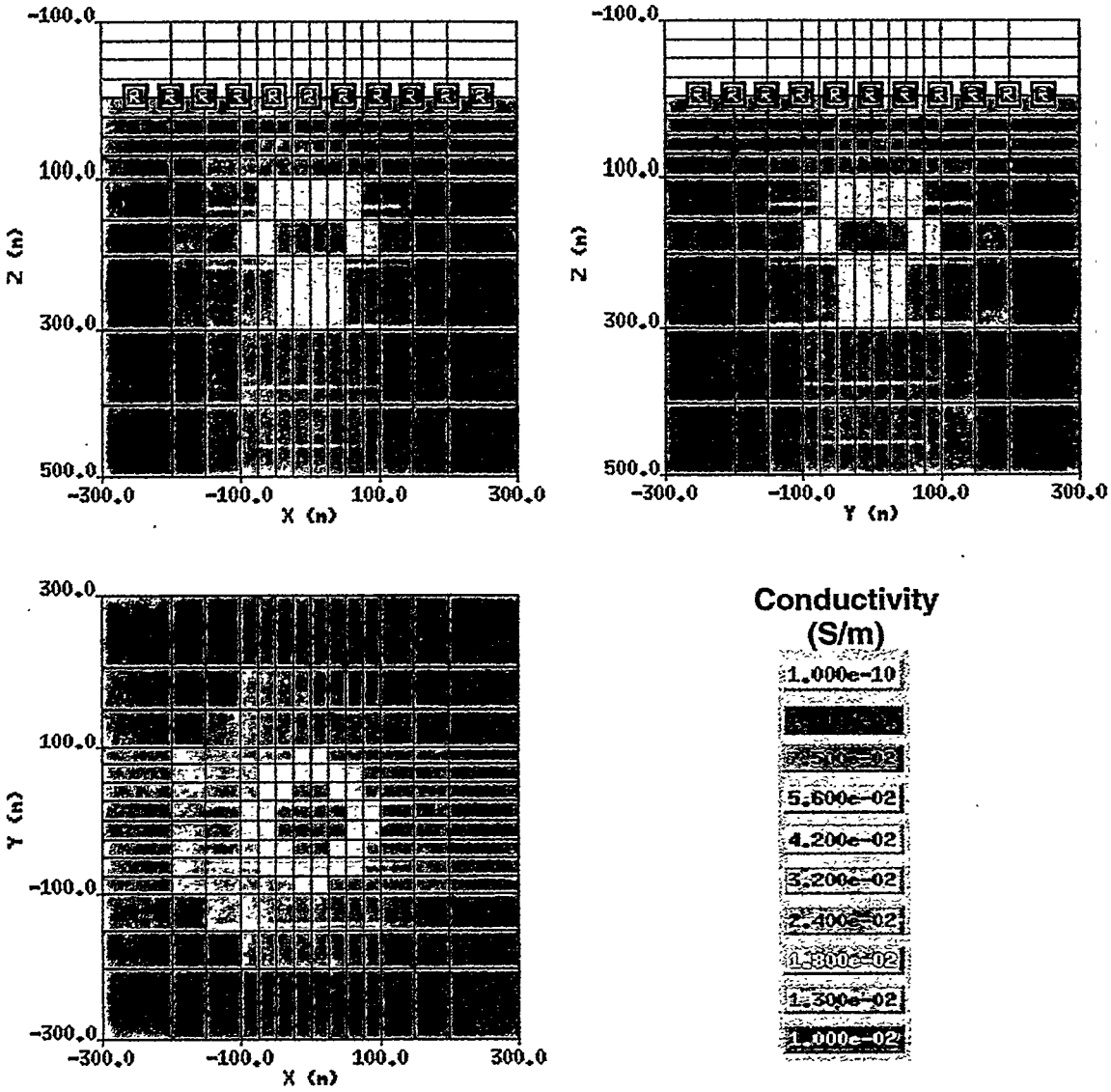
-100.0
100.0
300.0
500.0
Z (m)
-300.0
-100.0
100.0
300.0
X (n)
Y (n)
Conductivity
(S/m)
1.000e-10
5.600e-02
4.200e-02
3.200e-02
2.400e-02
1.800e-02
1.300e-02
1.000e-02

Figure 4

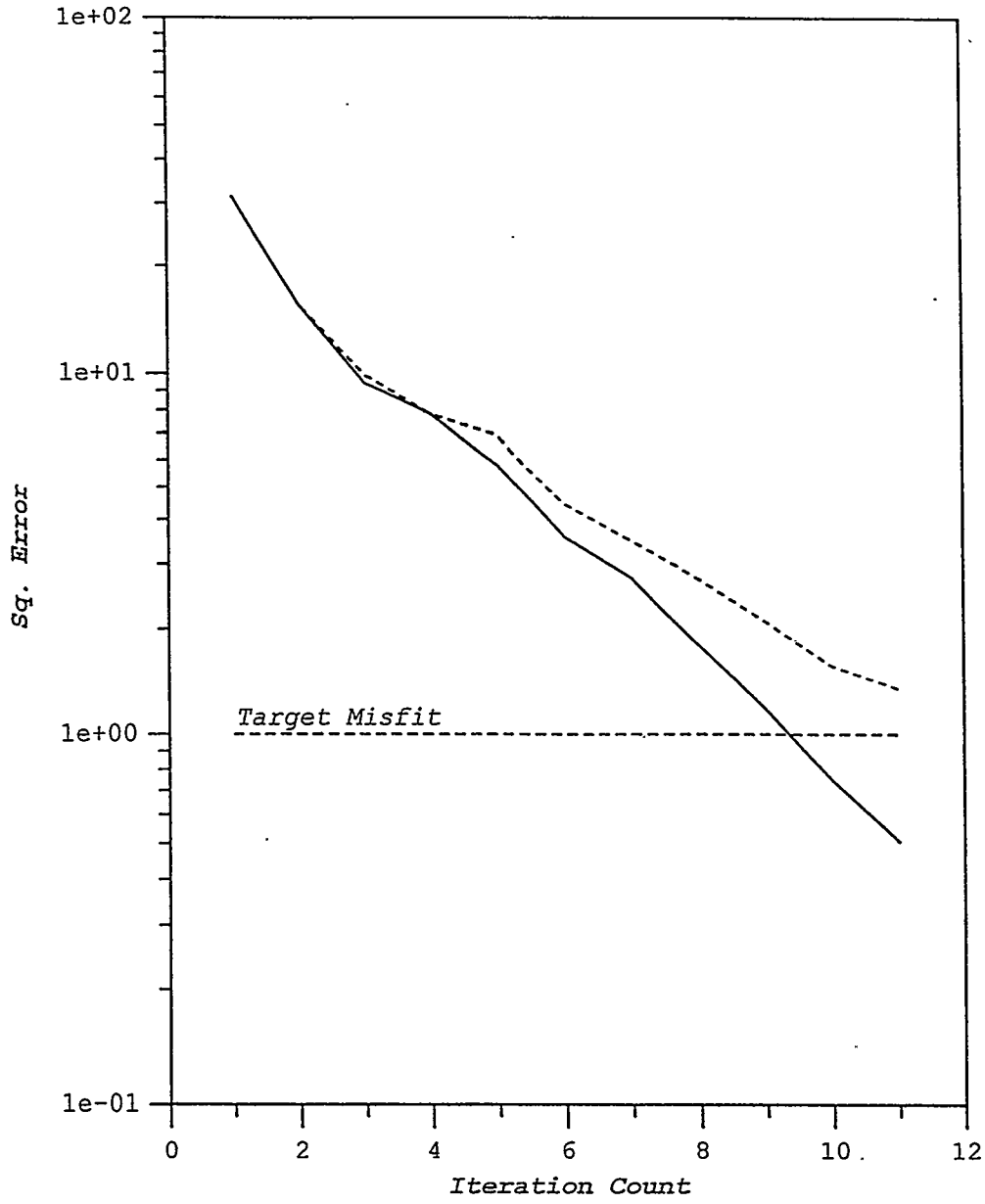
1e+02
1e+01
1e+00
1e-01
Sq. Error
Target Misfit
0
2
4
6
8
10
12
Iteration Count

Figure 5

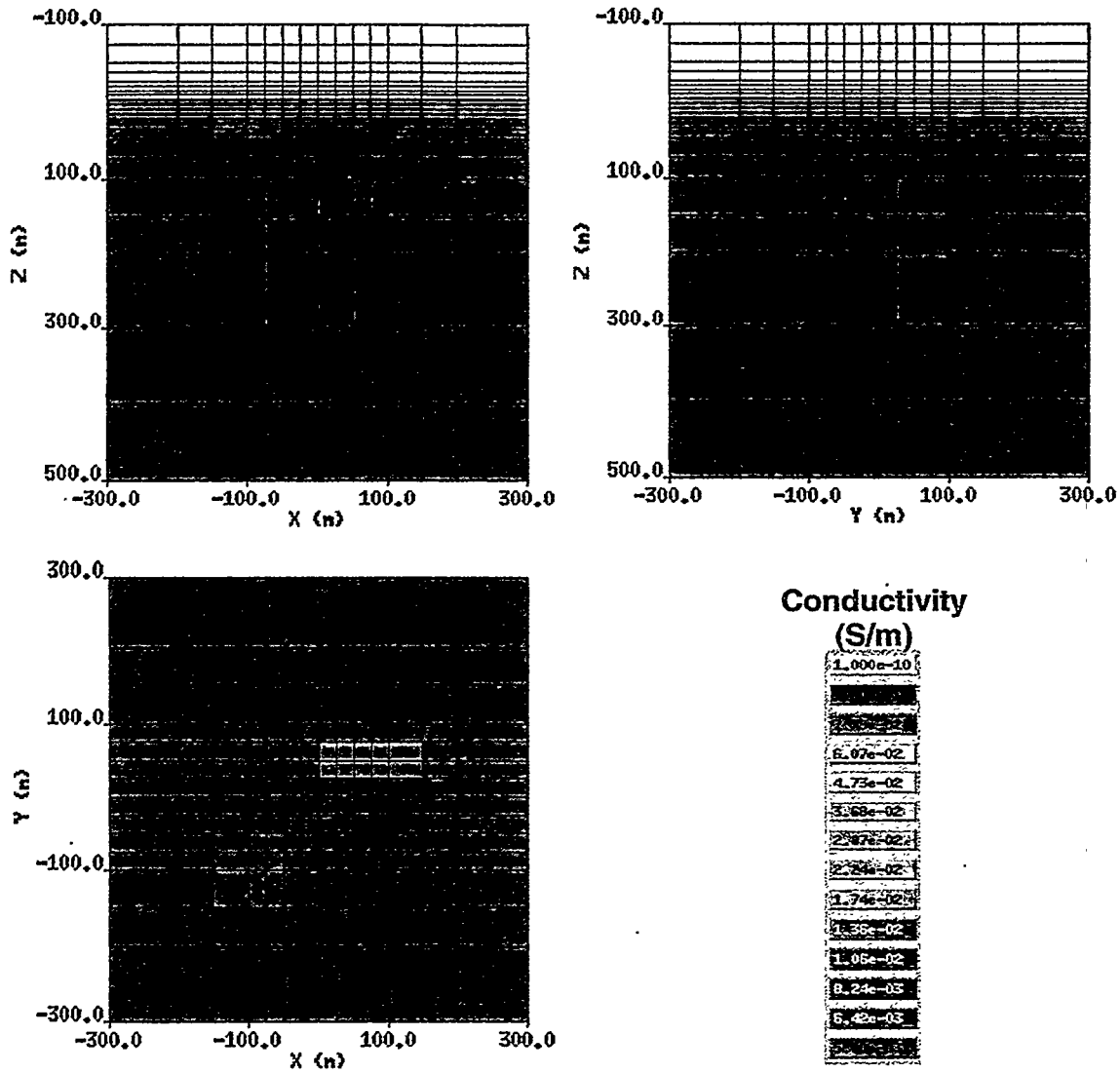
-100.0
100.0
300.0
500.0
Z (n)
-300.0
-100.0
100.0
300.0
X (n)
Y (n)
Conductivity
(S/m)
1.000e-10
6.07e-02
4.73e-02
3.68e-02
2.24e-02
1.74e-02
1.08e-02
8.24e-03
6.42e-03

Figure 6

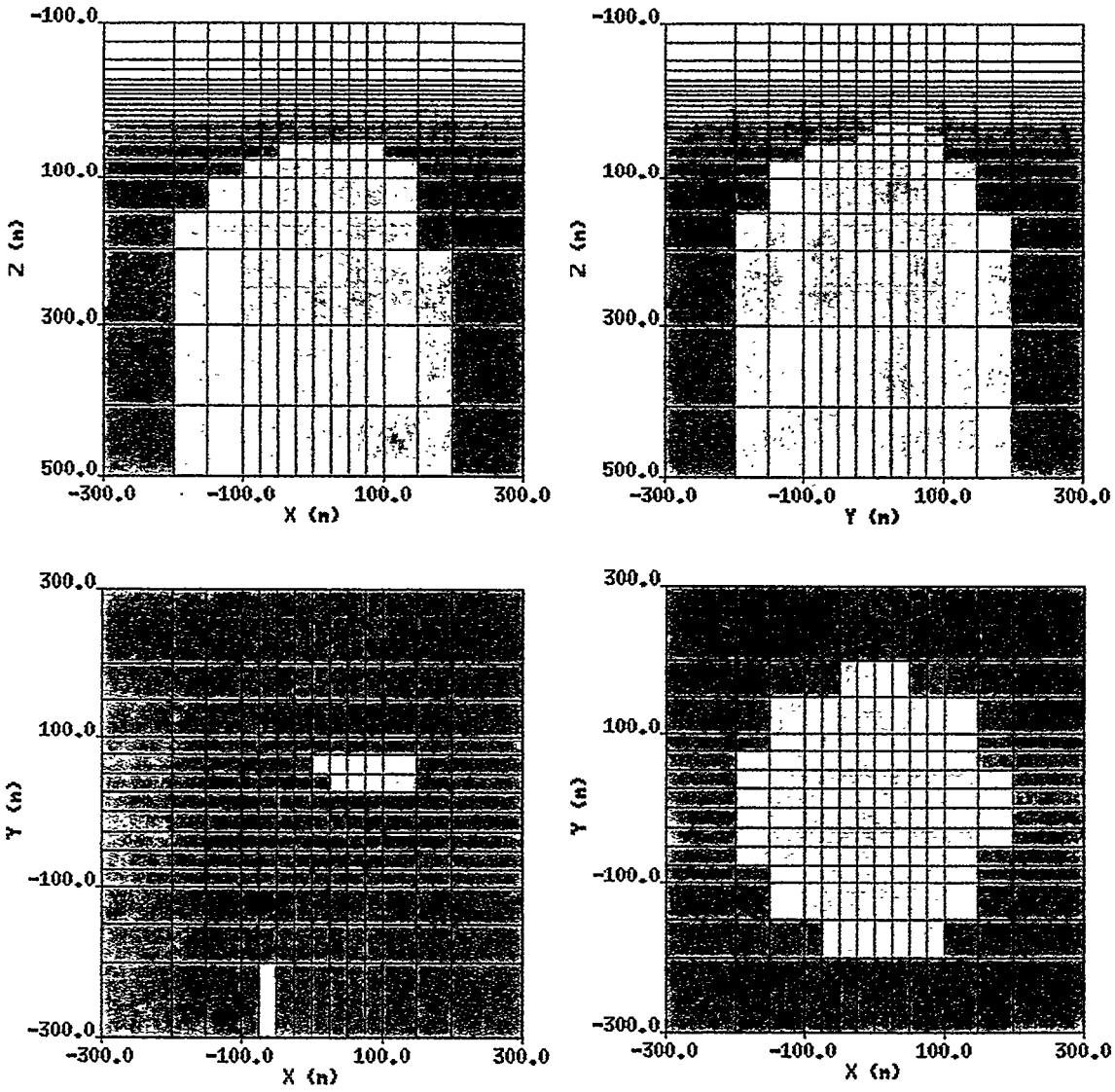
-100.0
100.0
300.0
500.0
Z (n)
-300.0
-100.0
100.0
300.0
X (n)
-100.0
100.0
300.0
500.0
Z (n)
-300.0
-100.0
100.0
300.0
Y (n)
300.0
100.0
-100.0
-300.0
Y (n)
-300.0
-100.0
100.0
300.0
X (n)
300.0
100.0
-100.0
-300.0
Y (n)
-300.0
-100.0
100.0
300.0
X (n)

Figure 7

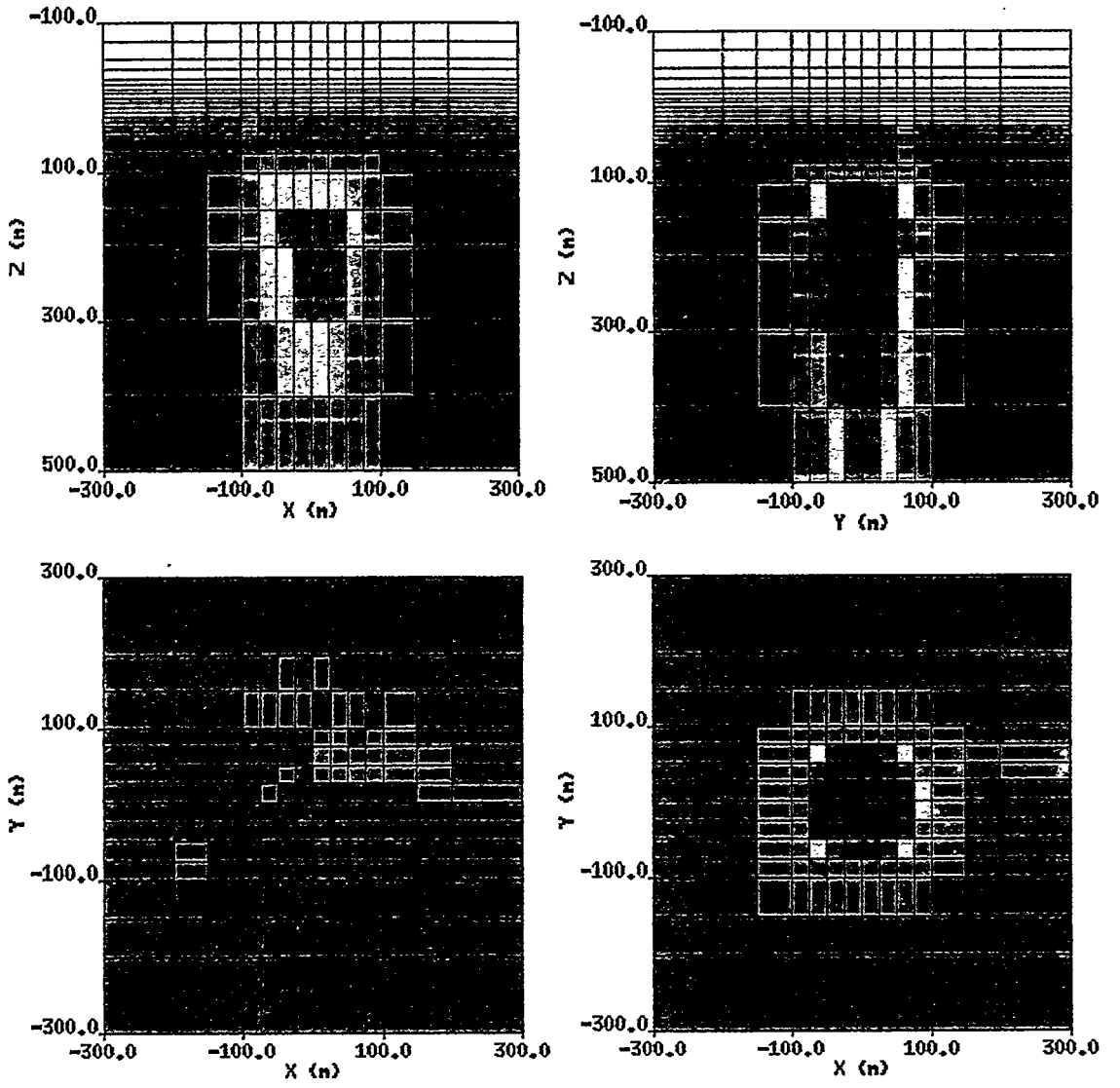

Figure 8

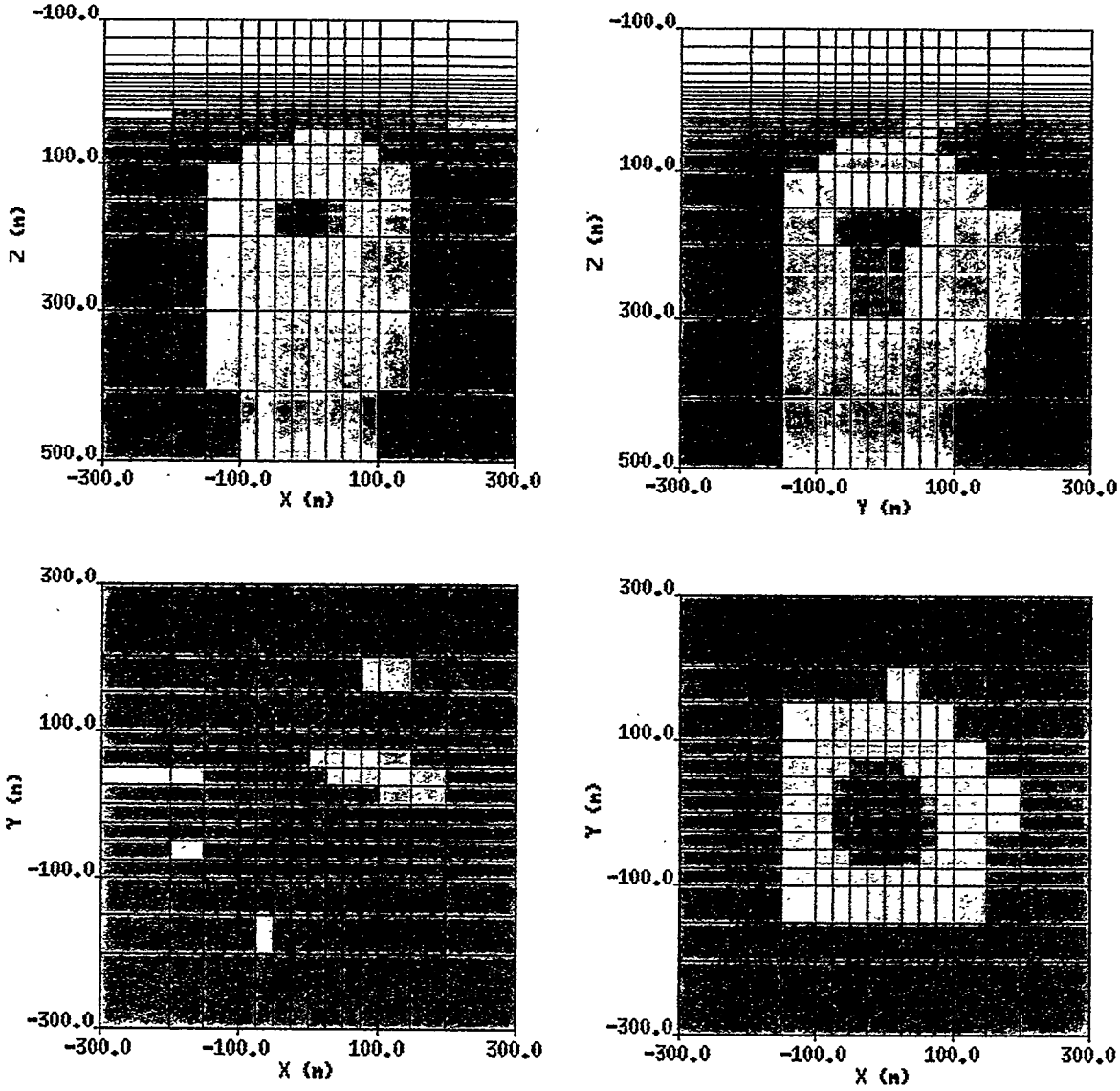

Figure 9

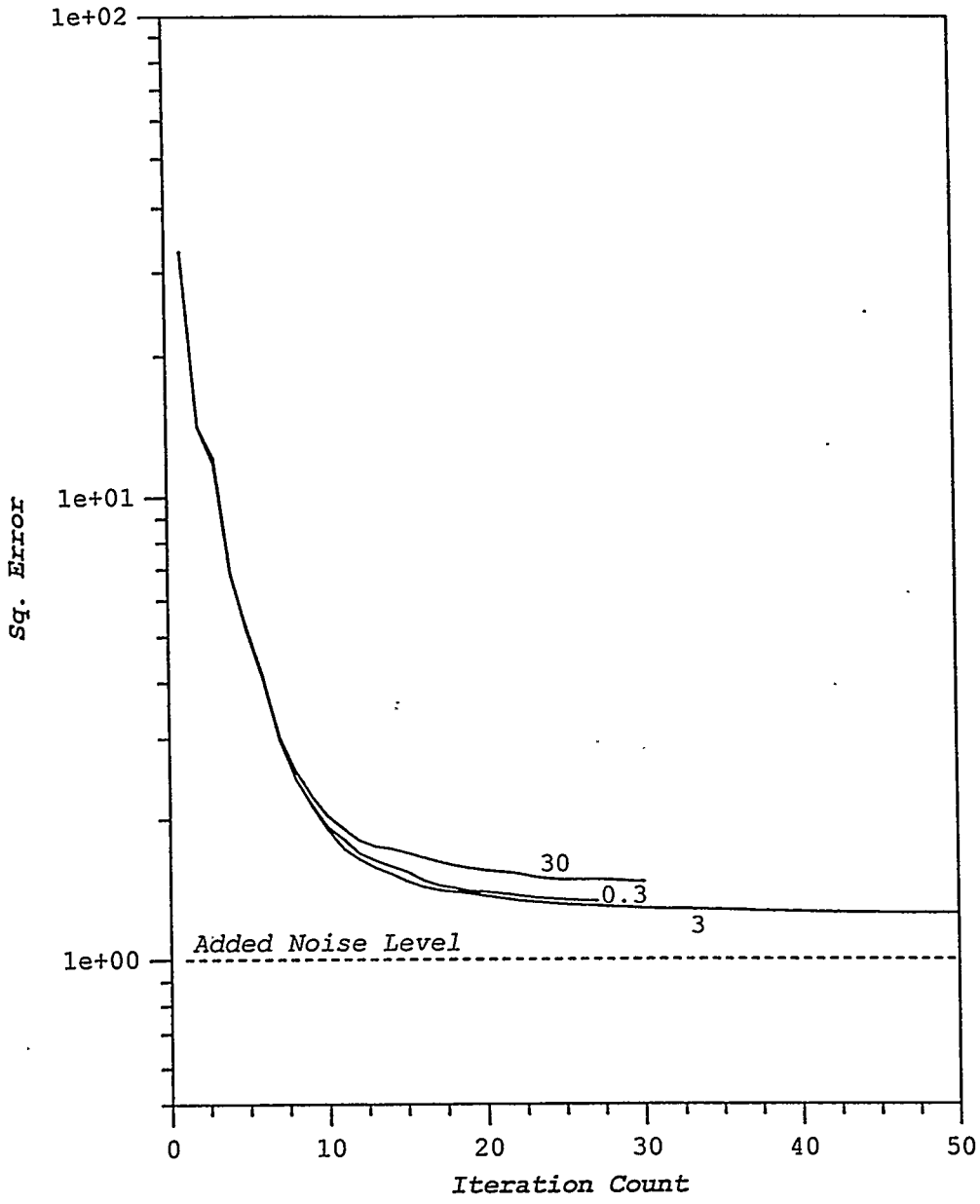
1e+02
1e+01
1e+00
Sq. Error
30
0.3
3
Added Noise Level
0
10
20
30
40
50
Iteration Count

Figure 10

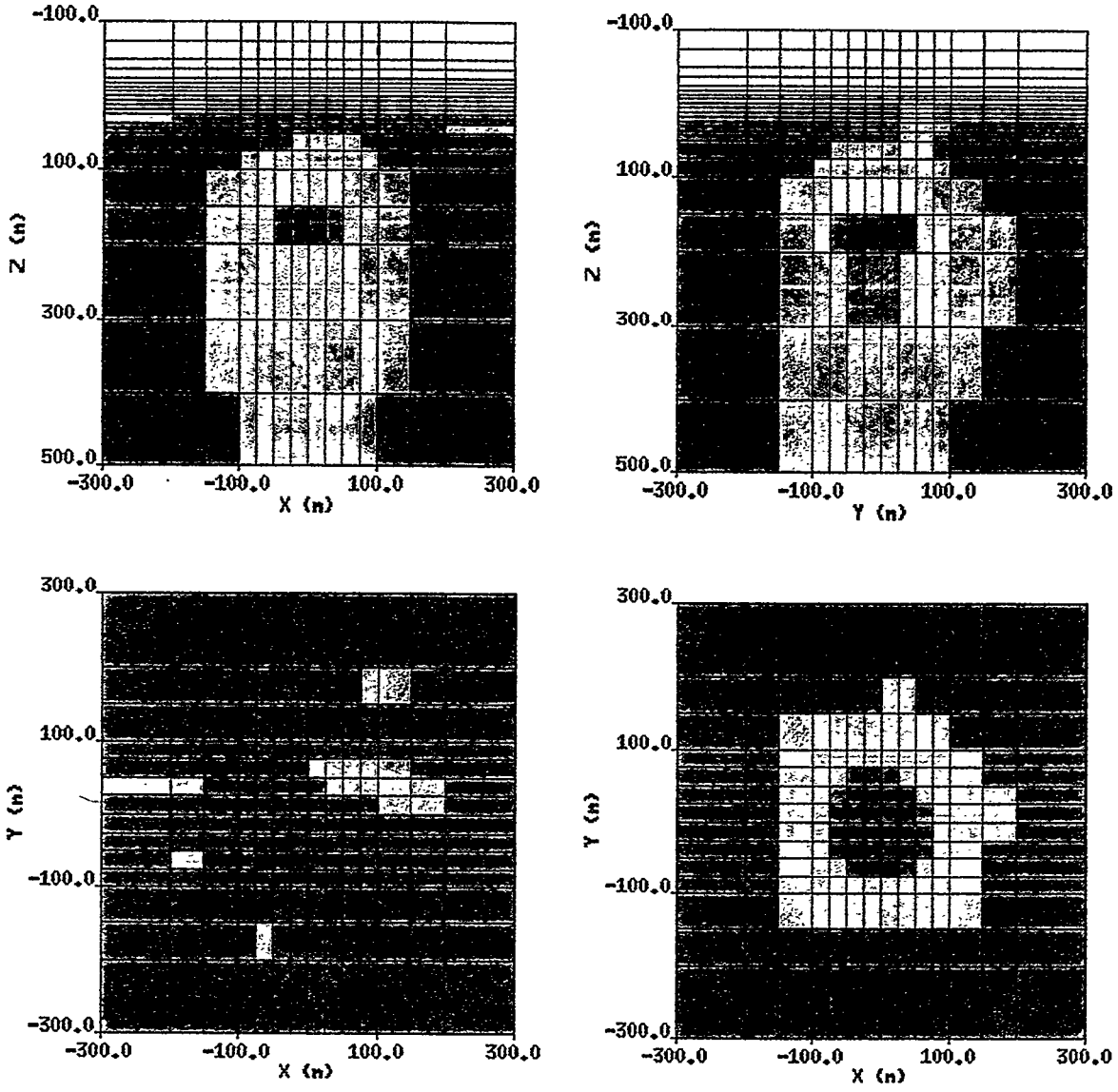
-100.0
100.0
300.0
500.0
Z (n)
-300.0
-100.0
100.0
300.0
X (n)
-100.0
100.0
300.0
500.0
Z (n)
-300.0
-100.0
100.0
300.0
Y (n)
300.0
100.0
-100.0
-300.0
Y (n)
-300.0
-100.0
100.0
300.0
X (n)
300.0
100.0
-100.0
-300.0
Y (n)
-300.0
-100.0
100.0
300.0
X (n)

Figure 11

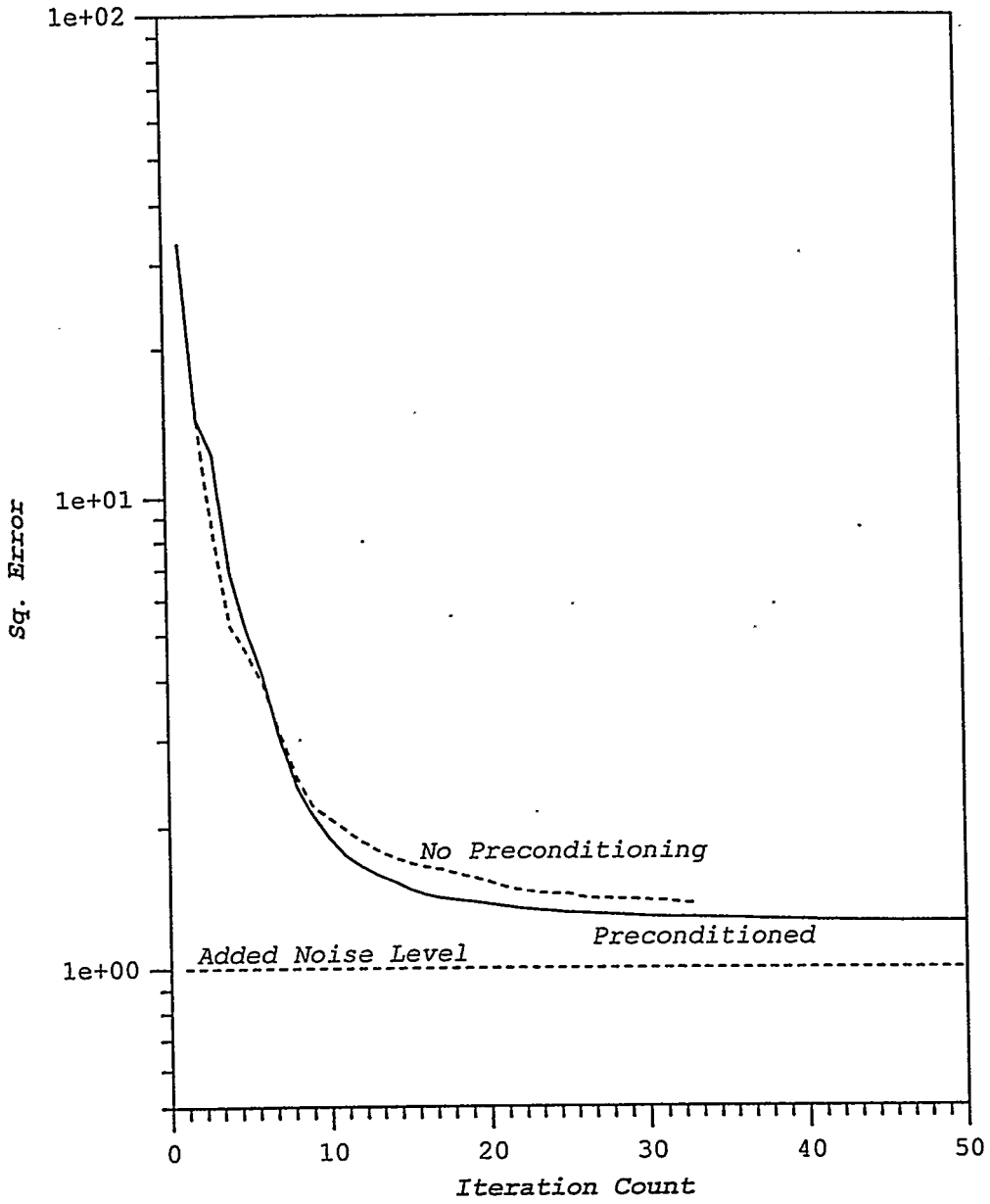
1e+02
1e+01
1e+00
Sq. Error
No Preconditioning
Preconditioned
Added Noise Level
0
10
20
30
40
50
Iteration Count

Figure 12

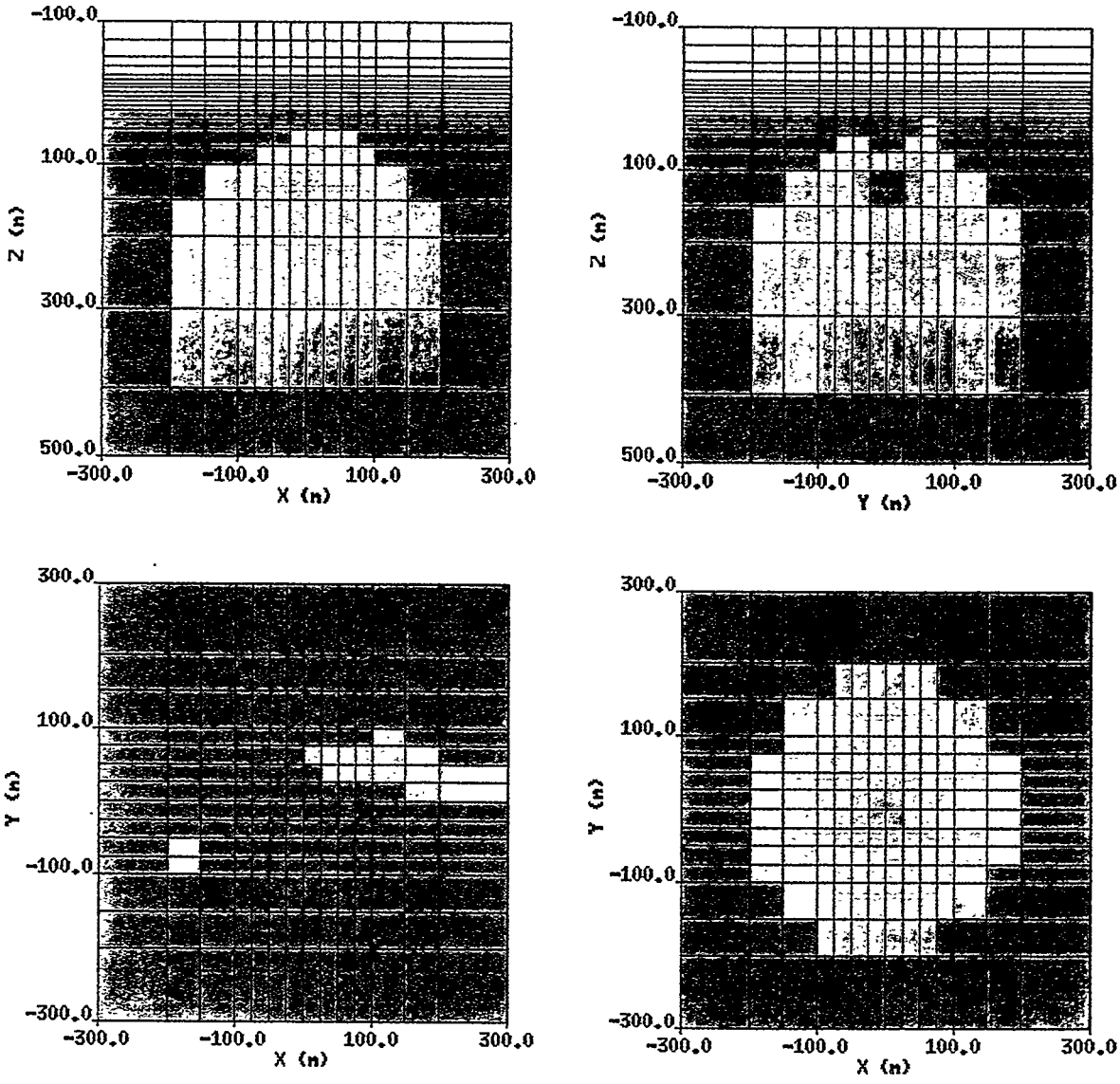
-100.0
100.0
300.0
500.0
Z (n)
-300.0
-100.0
100.0
300.0
X (n)
-100.0
100.0
300.0
500.0
Z (n)
-300.0
-100.0
100.0
300.0
Y (n)
300.0
100.0
-100.0
-300.0
Y (n)
-300.0
-100.0
100.0
300.0
X (n)
300.0
100.0
-100.0
-300.0
Y (n)
-300.0
-100.0
100.0
300.0
X (n)

Figure 13

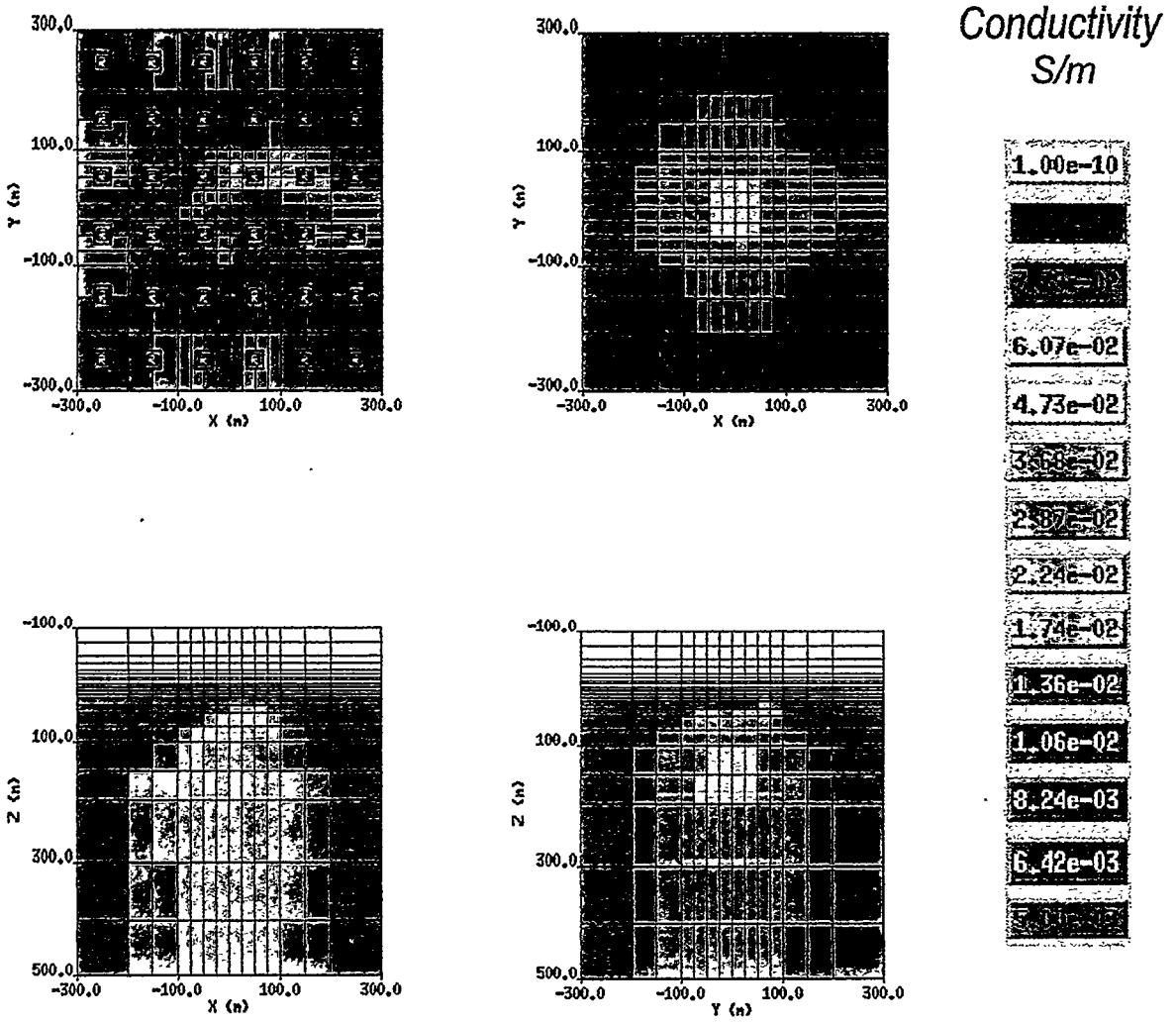
Conductivity
S/m
1.00e-10
6.07e-02
4.73e-02
2.24e-02
1.74e-02
1.36e-02
1.06e-02
8.24e-03
6.42e-03
300.0
100.0
-100.0
-300.0
Y (m)
X (m)
Z (m)
500.0

Figure 14

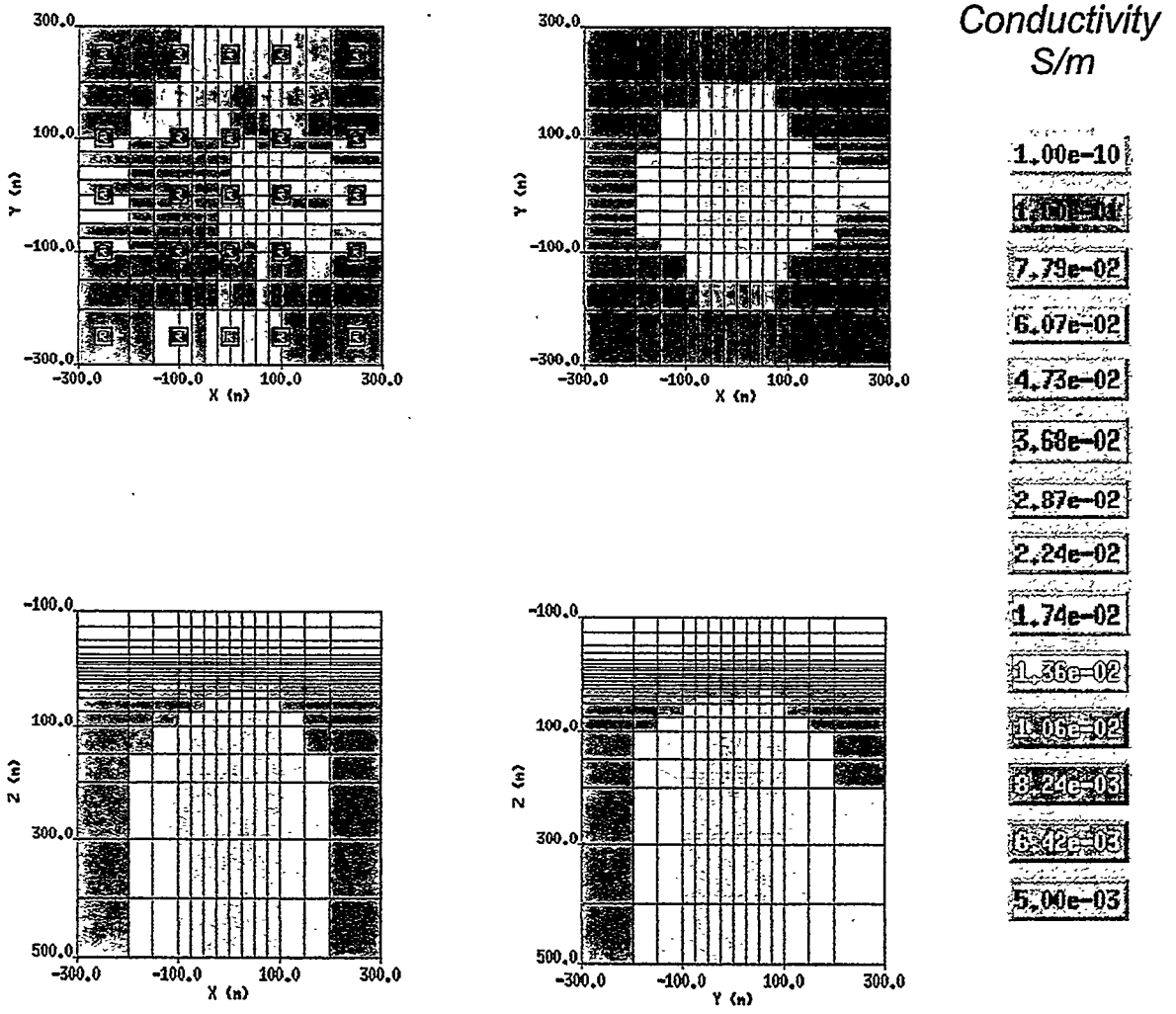
Conductivity
S/m
1.00e-10
7.79e-02
6.07e-02
4.73e-02
3.68e-02
2.87e-02
2.24e-02
1.74e-02
1.36e-02
1.06e-02
8.24e-03
6.42e-03
5.00e-03
300.0
100.0
-100.0
-300.0
Y (m)
X (m)
Z (m)
500.0

Figure 15

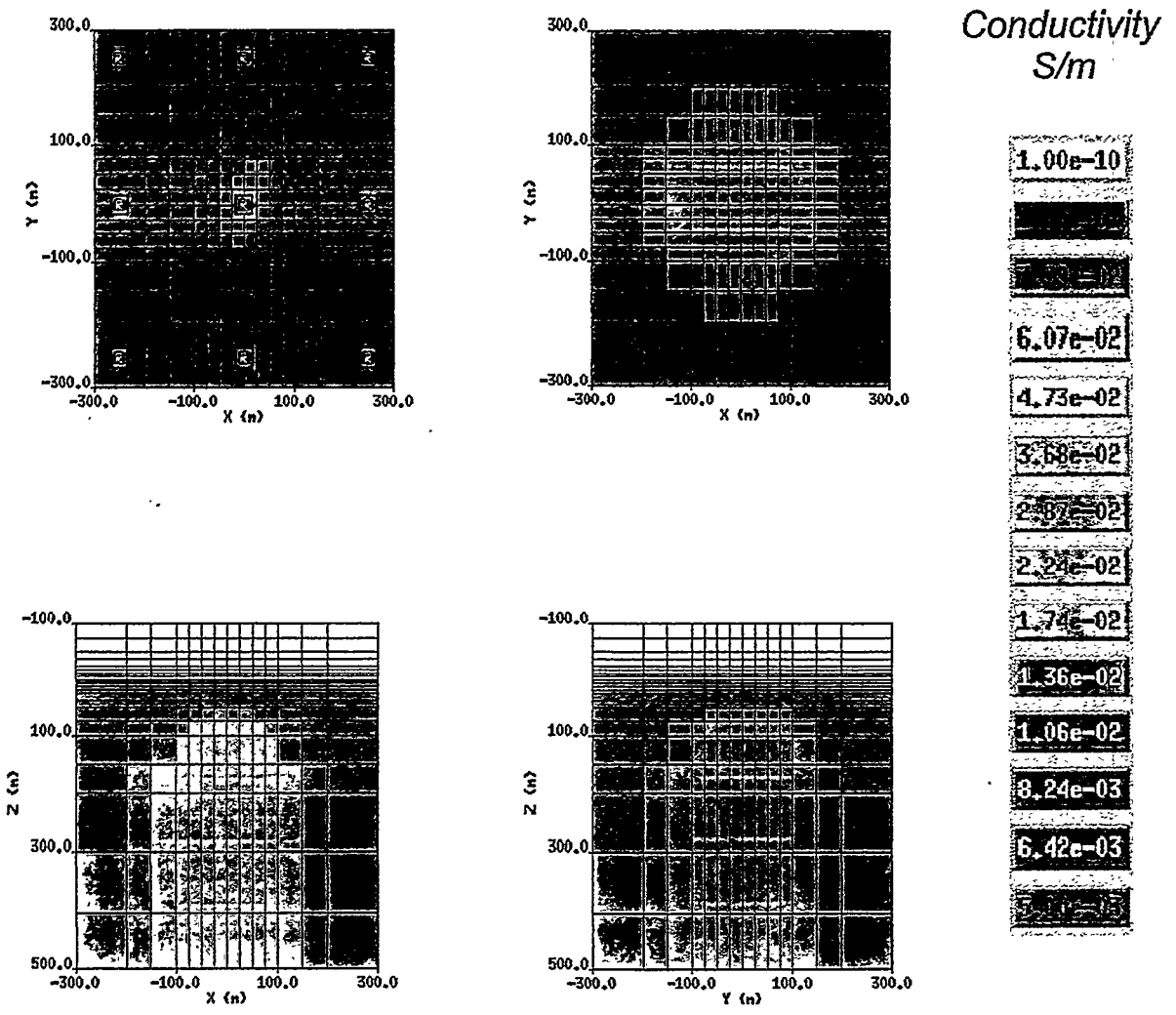
300.0
100.0
-100.0
-300.0
Y (n)
-300.0
-100.0
100.0
300.0
X (n)
Conductivity
S/m
1.00e-10
6.07e-02
4.73e-02
3.68e-02
2.87e-02
2.24e-02
1.74e-02
1.36e-02
1.06e-02
8.24e-03
6.42e-03
-100.0
100.0
300.0
500.0
Z (n)
Y (n)

Figure 16

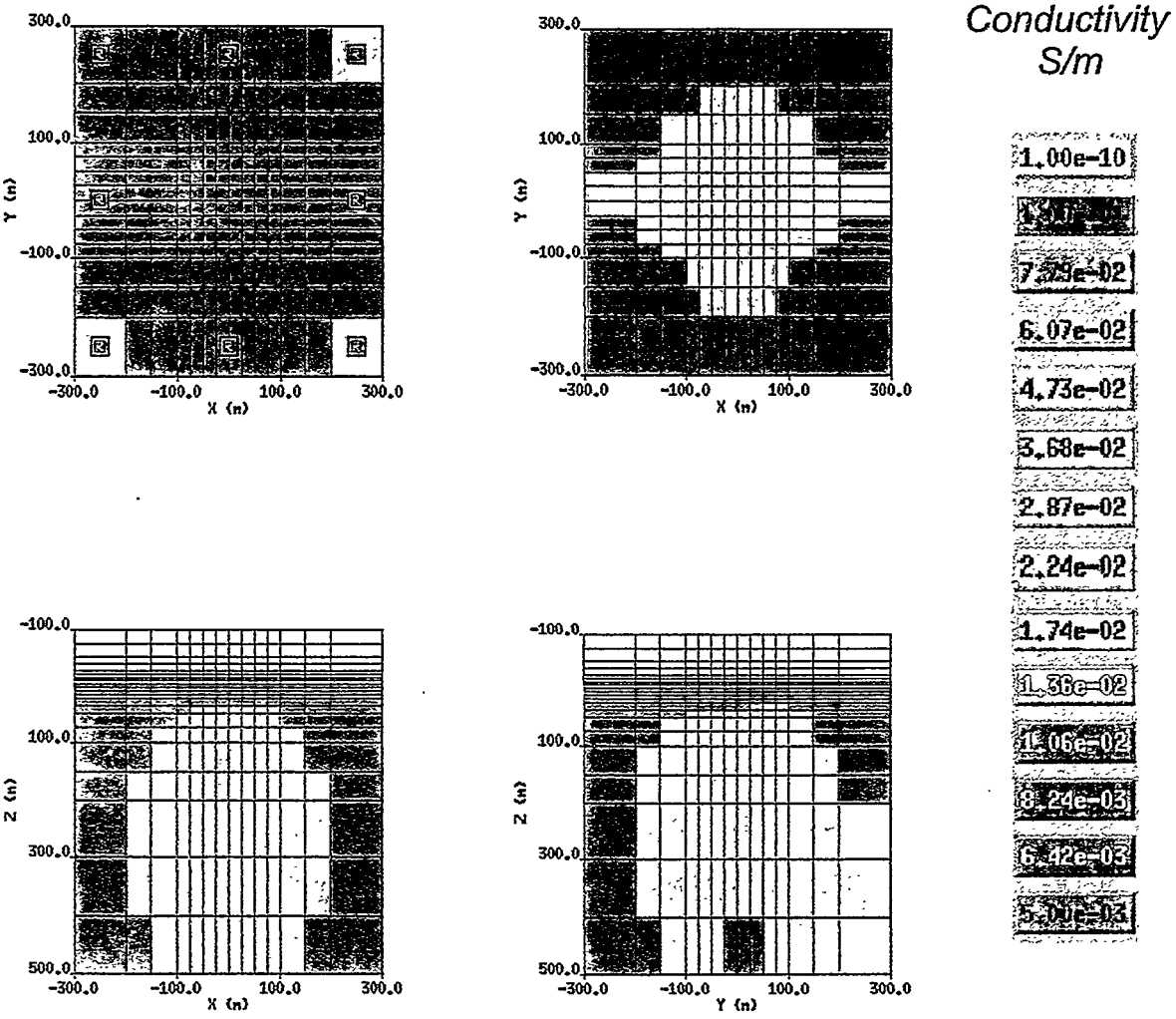
Conductivity
S/m
1.00e-10
7.29e-02
6.07e-02
4.73e-02
3.68e-02
2.87e-02
2.24e-02
1.74e-02
1.36e-02
1.06e-02
8.24e-03
6.42e-03
5.00e-03
300.0
100.0
-100.0
-300.0
Y (n)
X (n)
Z (n)
500.0

Figure 17

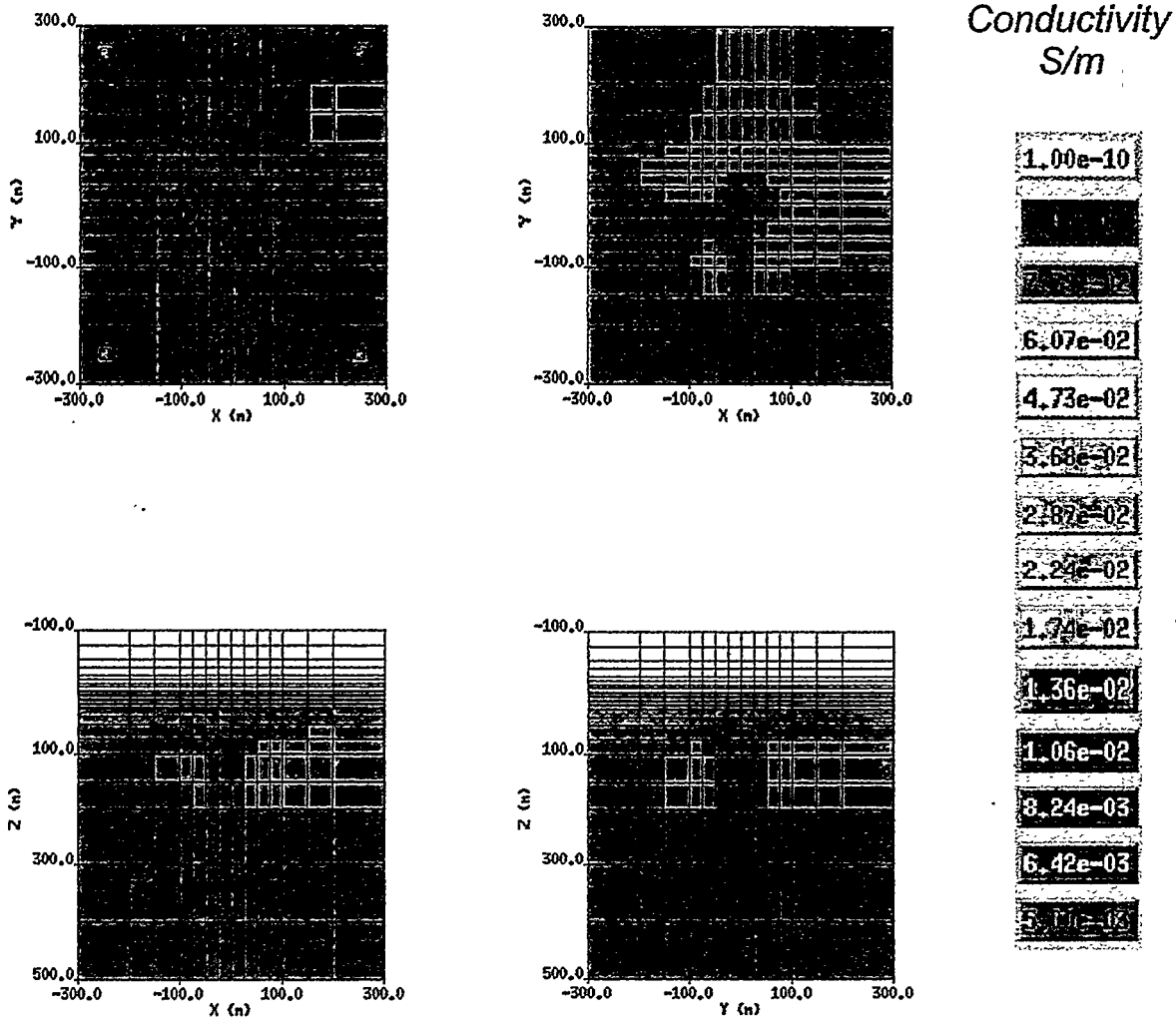
300.0
100.0
-100.0
-300.0
Y (n)
-300.0
-100.0
100.0
300.0
X (n)
Conductivity
S/m
1.00e-10
6.07e-02
4.73e-02
3.68e-02
2.87e-02
2.24e-02
1.36e-02
1.06e-02
8.24e-03
6.42e-03
-100.0
100.0
300.0
500.0
Z (n)
Y (n)

Figure 18

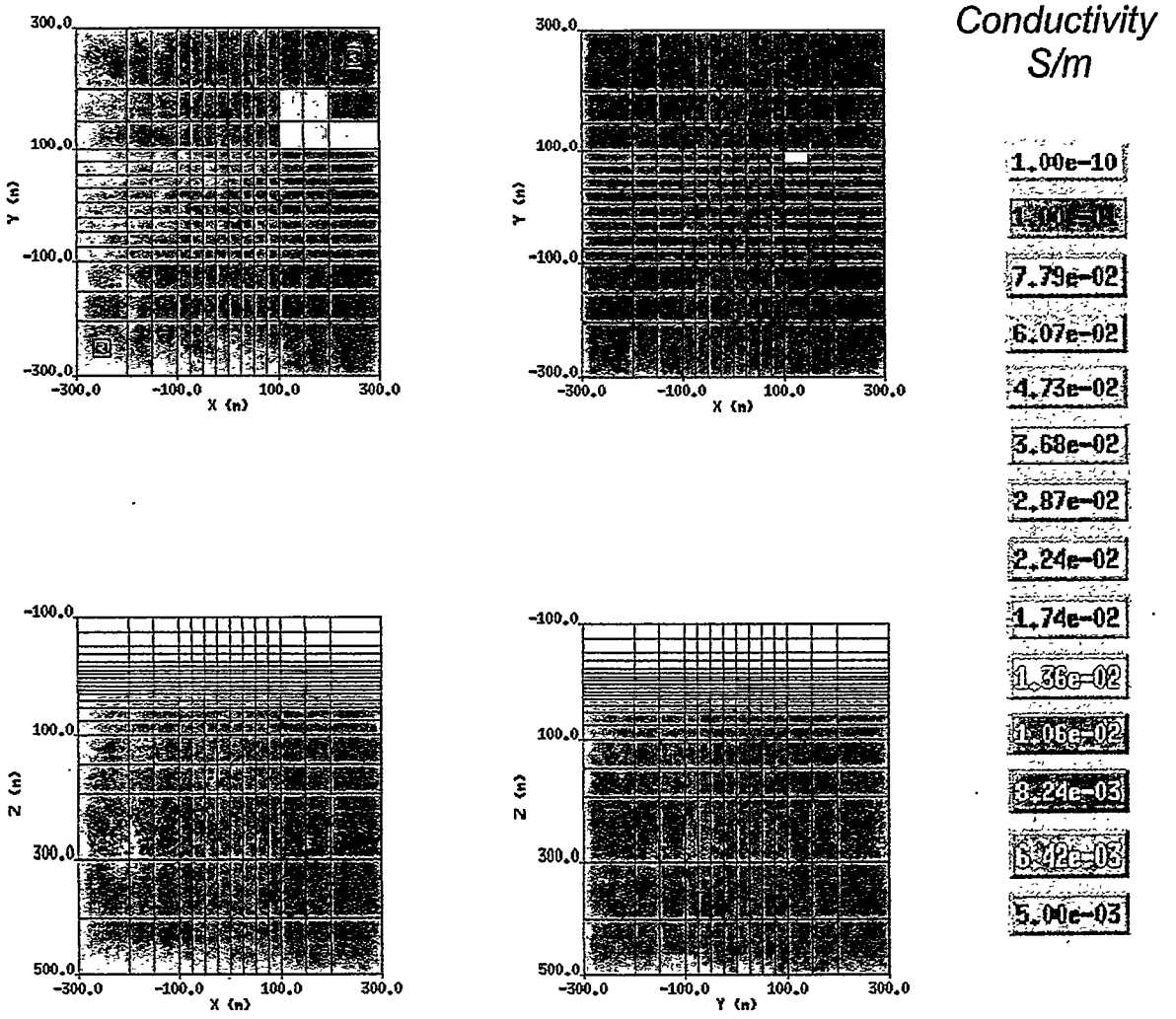
Conductivity
S/m
1.00e-10
7.79e-02
6.07e-02
4.73e-02
3.68e-02
2.87e-02
2.24e-02
1.74e-02
1.36e-02
1.06e-02
8.24e-03
6.42e-03
5.00e-03
300.0
100.0
-100.0
-300.0
Y (n)
X (n)
Z (n)
500.0

Figure 19

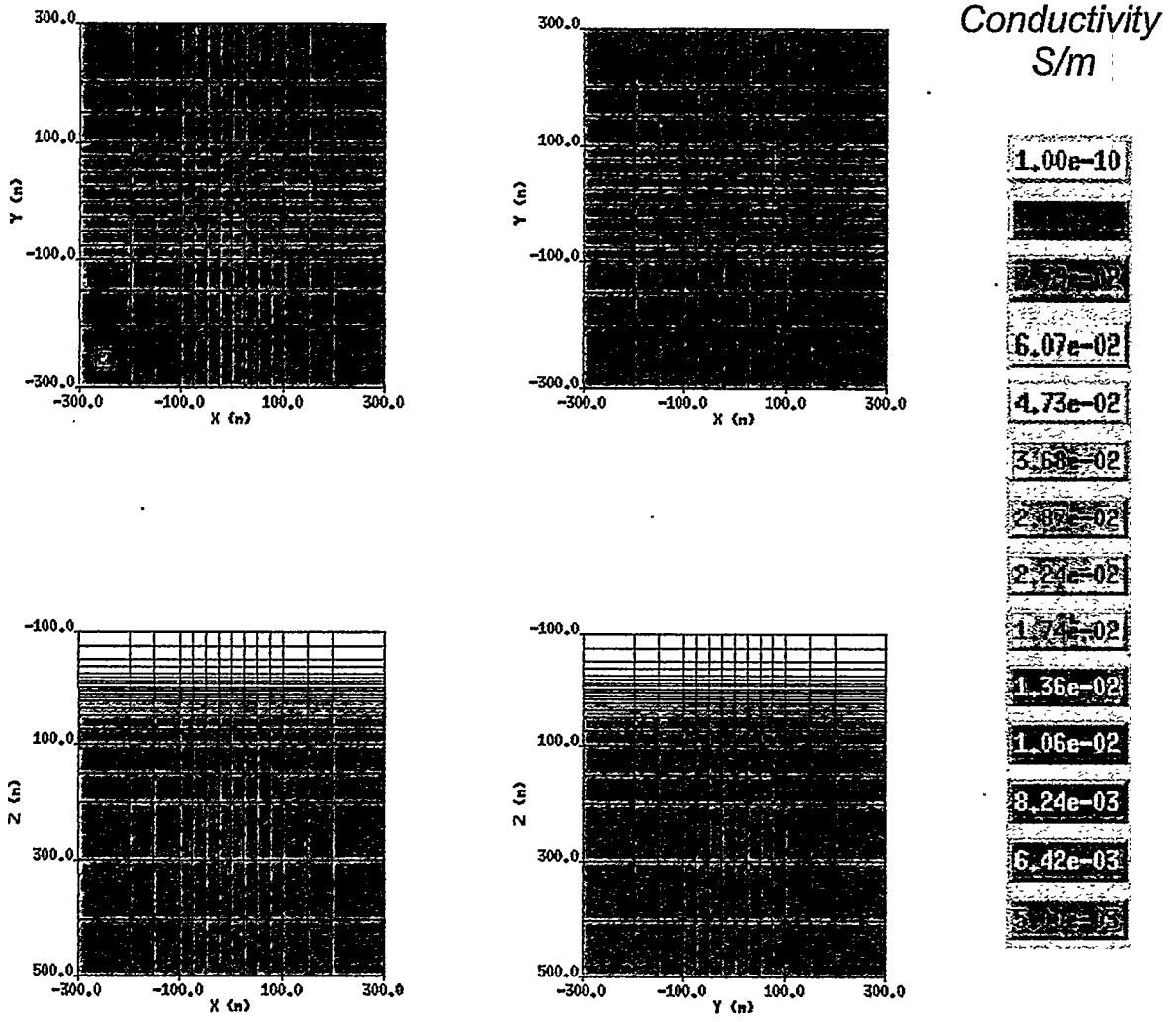
300.0
100.0
-100.0
-300.0
Y (n)
X (n)
Z (n)
500.0
Conductivity
S/m
1.00e-10
6.07e-02
4.73e-02
1.36e-02
1.06e-02
8.24e-03
6.42e-03

Figure 20

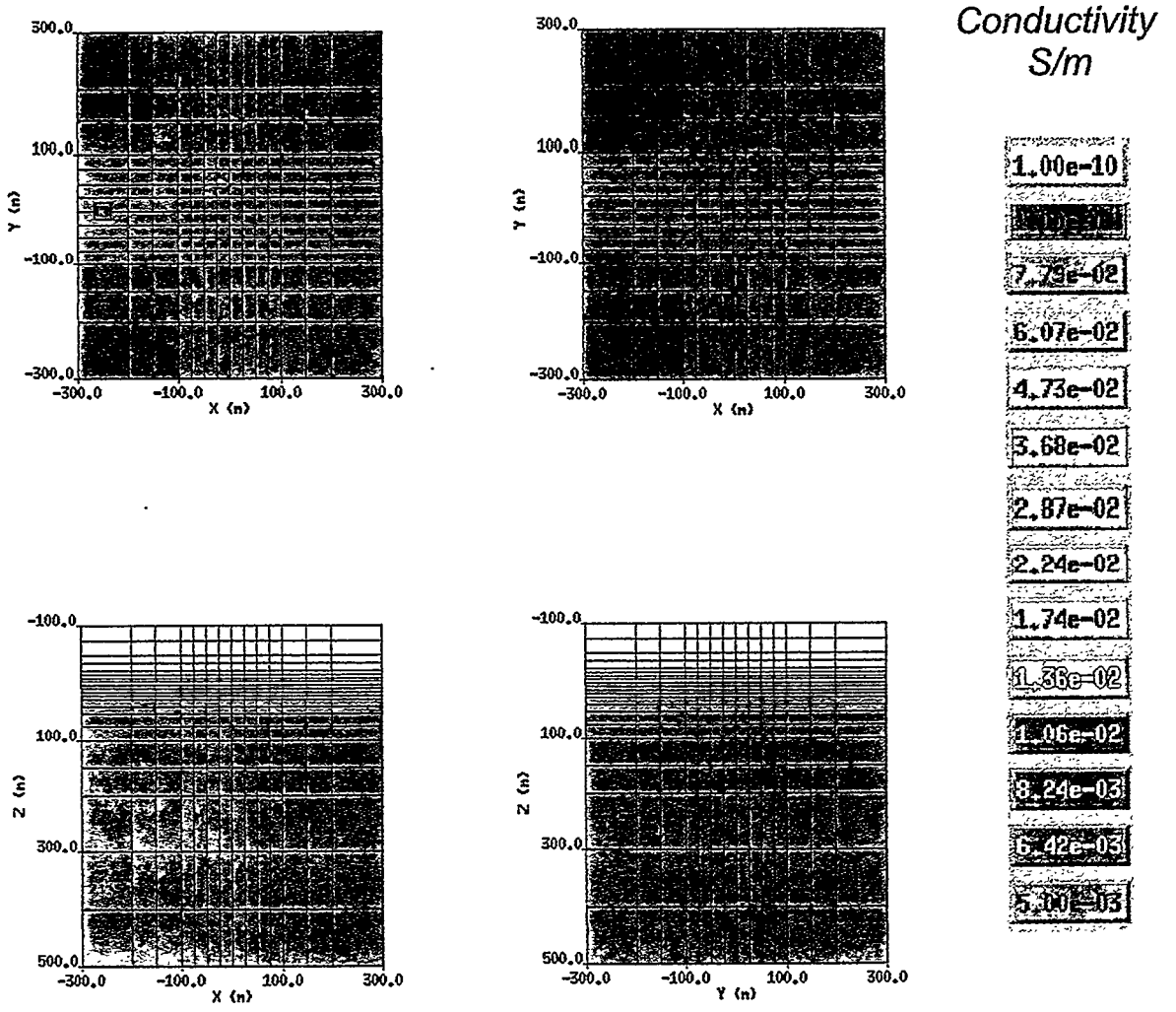
Conductivity
S/m
1.00e-10
7.79e-02
6.07e-02
4.73e-02
3.68e-02
2.87e-02
2.24e-02
1.74e-02
1.36e-02
1.06e-02
8.24e-03
6.42e-03
5.00e-03
300.0
100.0
-100.0
-300.0
Y (m)
X (m)
Z (m)
500.0

Figure 21

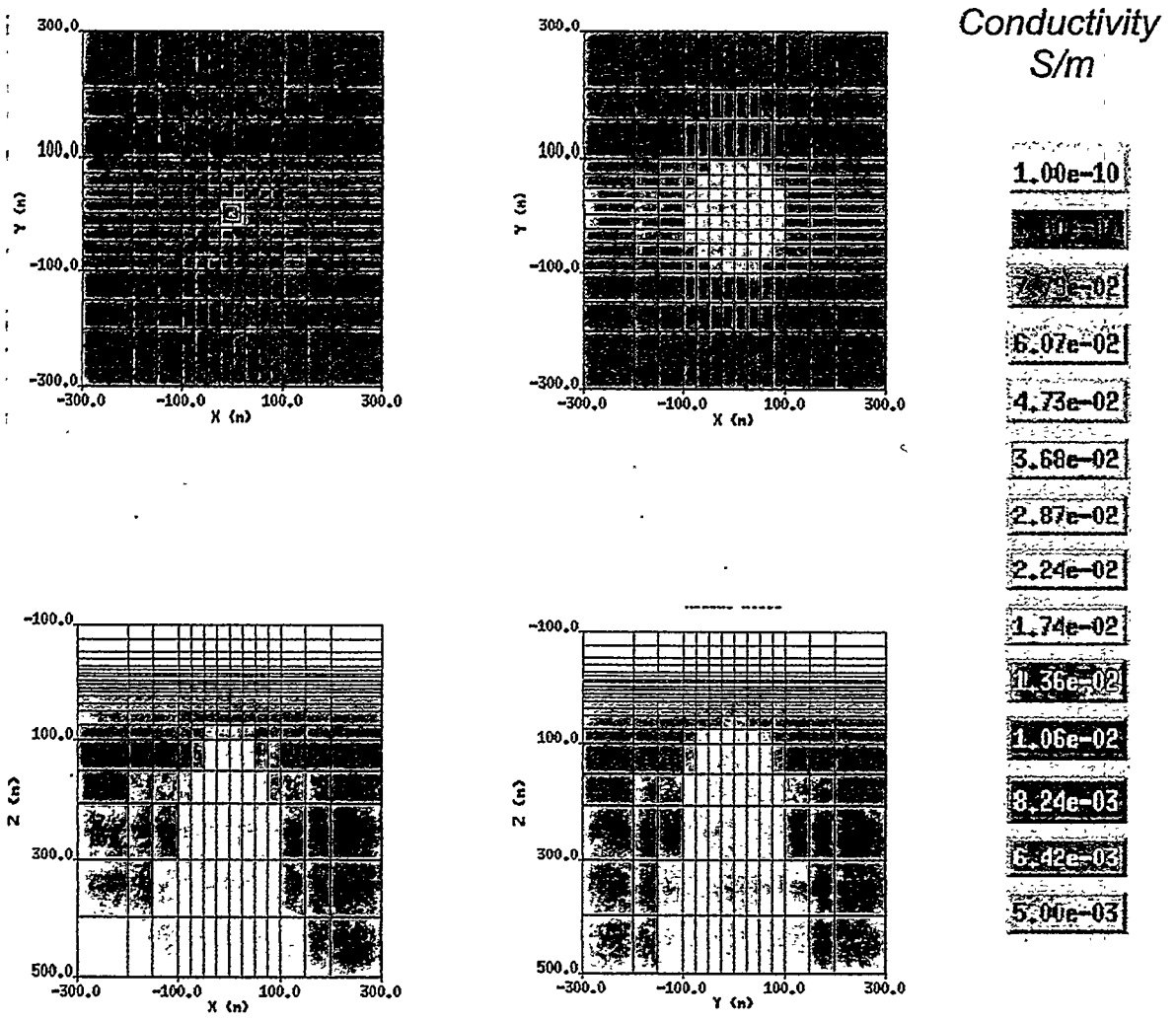
Conductivity
S/m
1.00e-10
6.07e-02
4.73e-02
3.68e-02
2.87e-02
2.24e-02
1.74e-02
1.36e-02
1.06e-02
8.24e-03
6.42e-03
5.00e-03
300.0
100.0
-100.0
-300.0
Y (n)
X (n)
Z (n)
-100.0
300.0
500.0

Figure 22

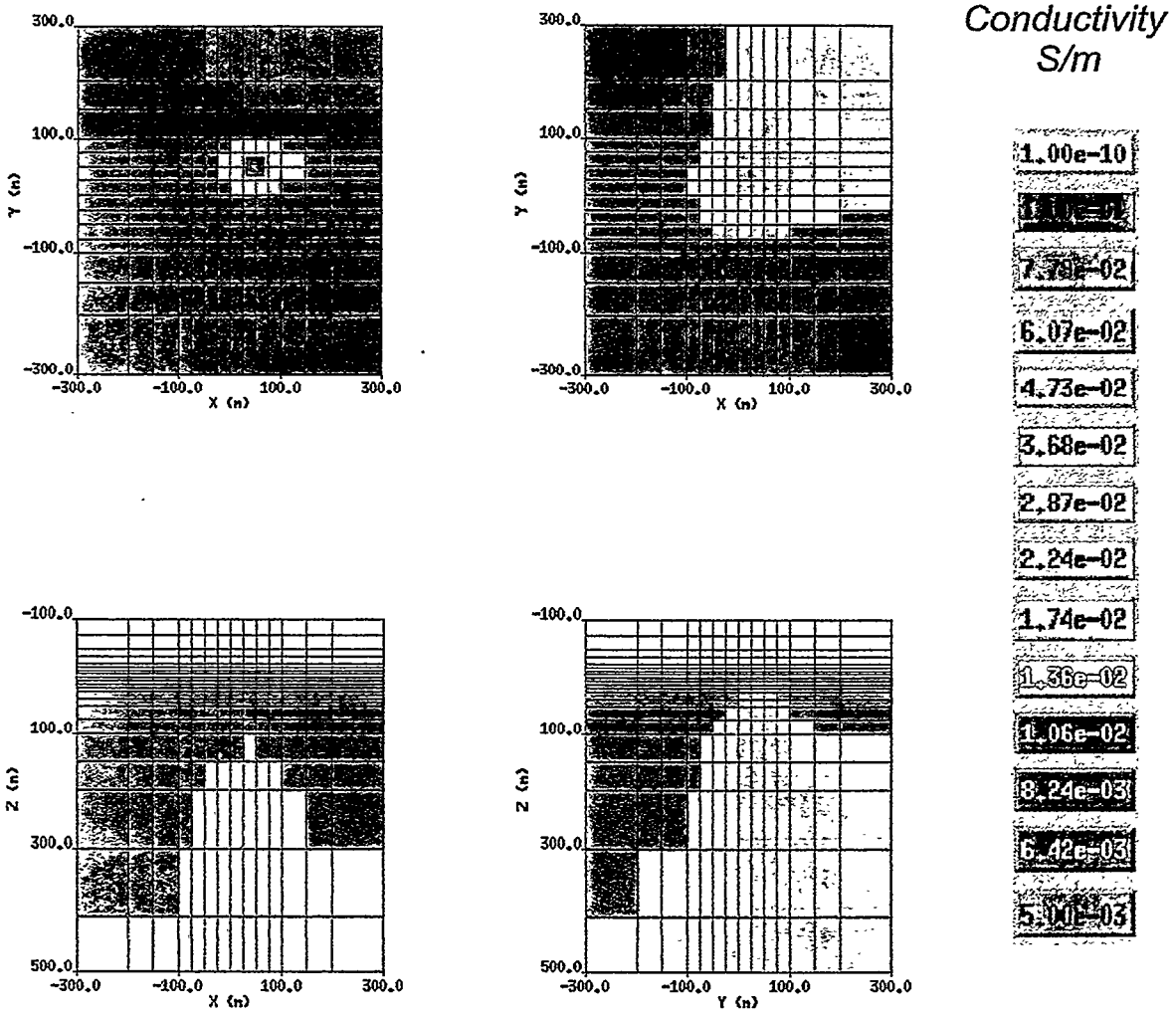
Conductivity
S/m
1.00e-10
7.78e-02
6.07e-02
4.73e-02
3.68e-02
2.87e-02
2.24e-02
1.74e-02
1.36e-02
1.06e-02
8.24e-03
6.42e-03
5.01e-03
300.0
100.0
-100.0
-300.0
Y (m)
X (m)
Z (m)
500.0

Figure 23

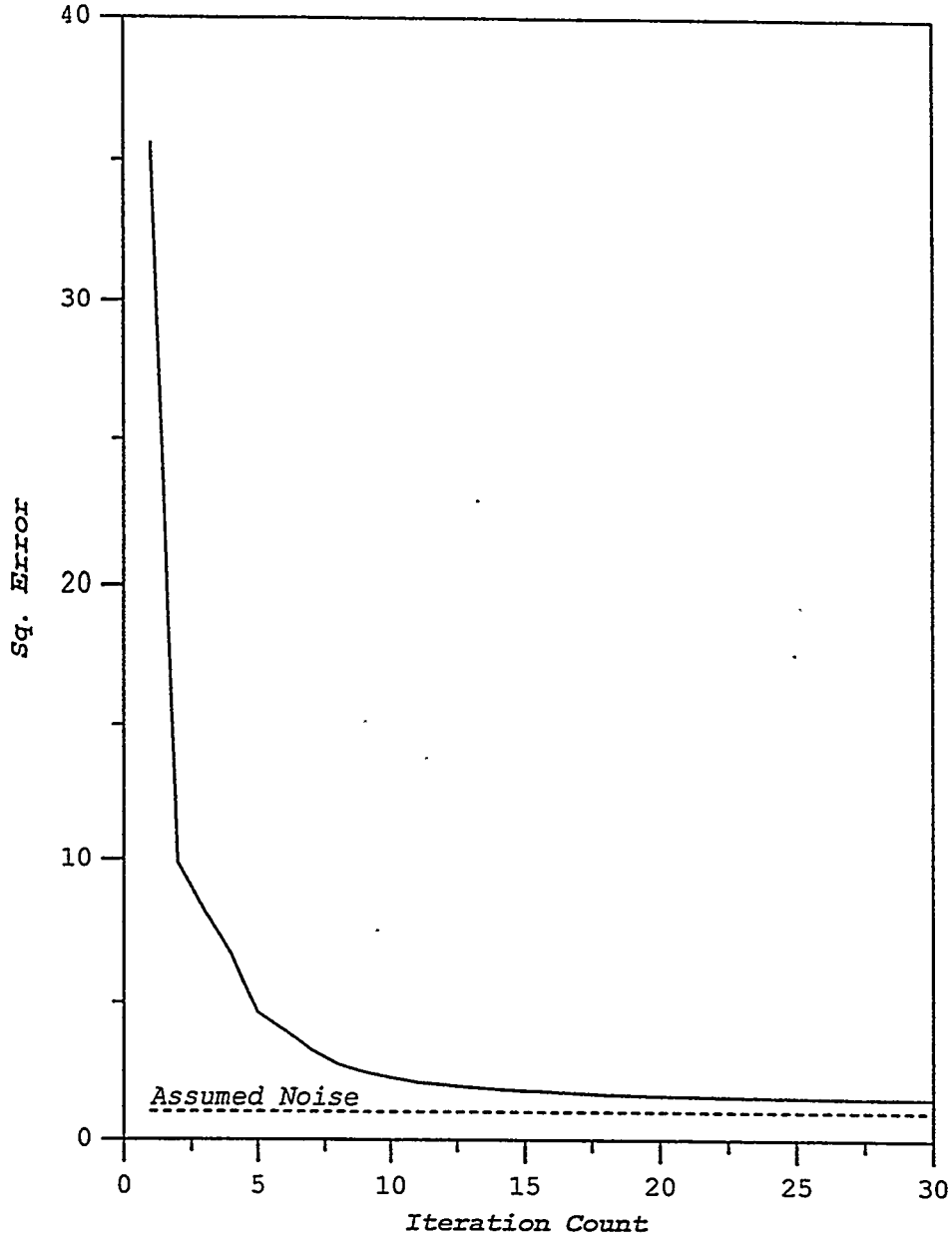
40
30
20
10
0
Sq. Error
Assumed Noise
0
5
10
15
20
25
30
Iteration Count

Figure 24

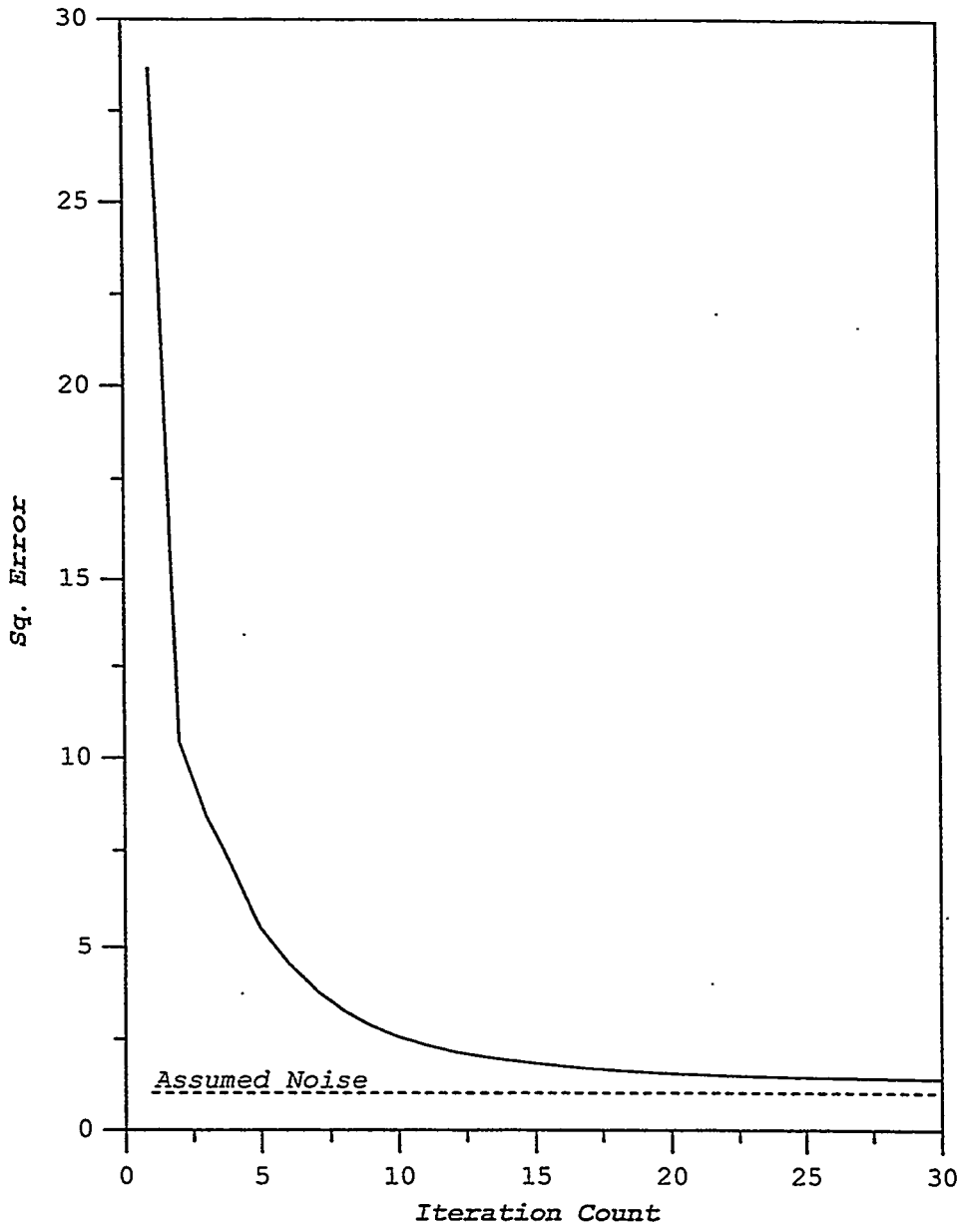
30
25
20
15
10
5
0
Sq. Error
Assumed Noise
0
5
10
15
20
25
30
Iteration Count

Figure 25

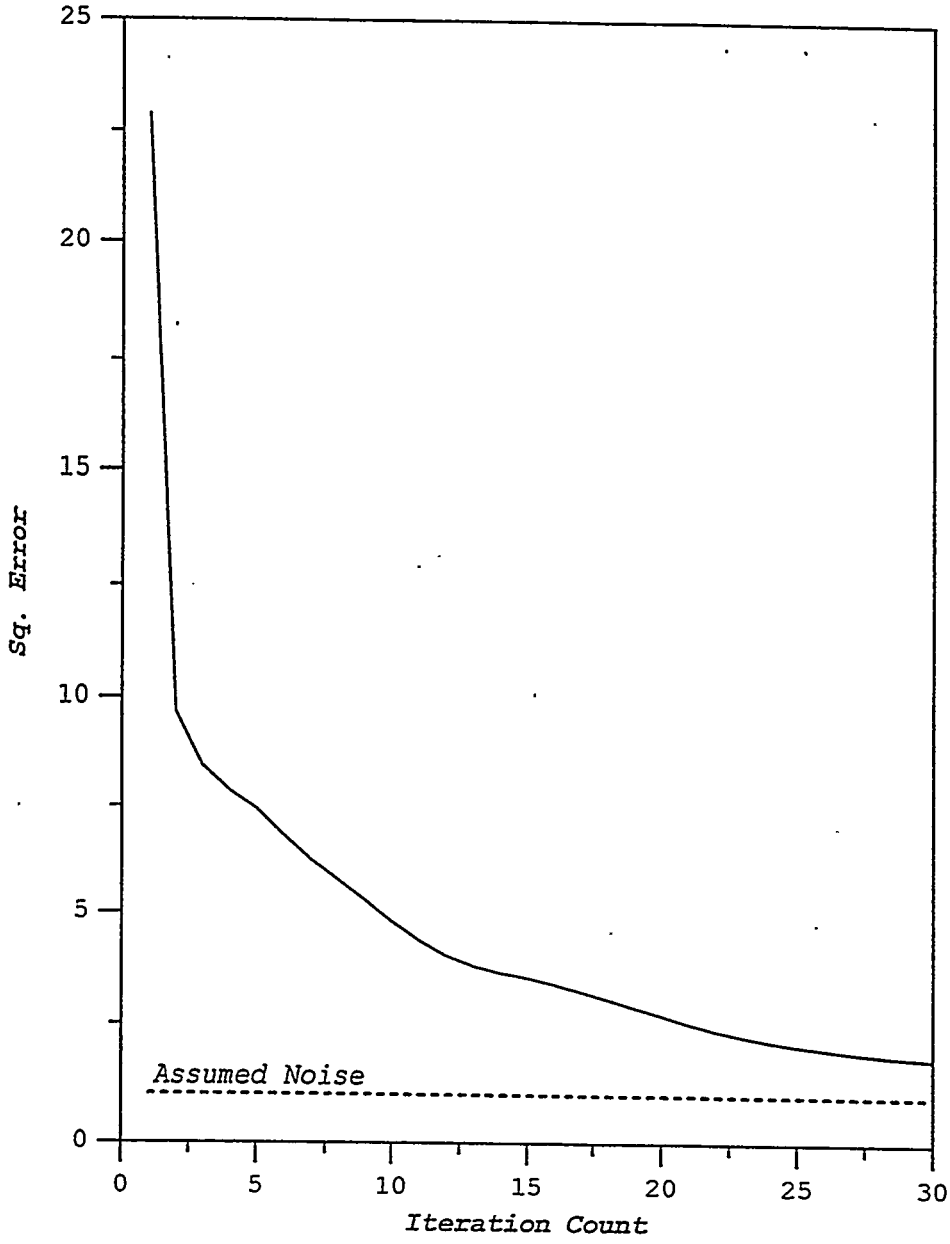
25
20
15
10
5
0
Sq. Error
Assumed Noise
0
5
10
15
20
25
30
Iteration Count

Figure 26

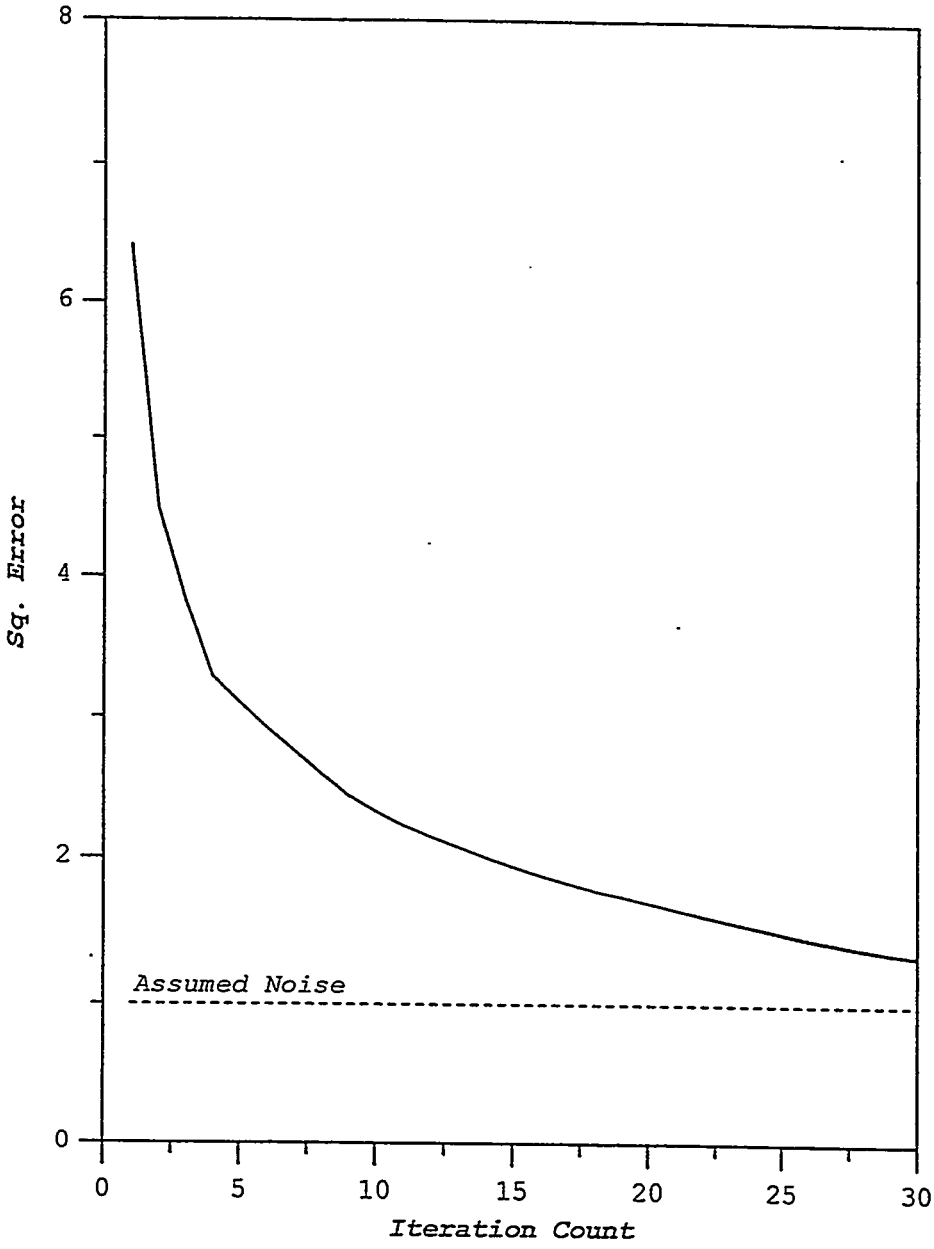
8
6
4
2
0
Sq. Error
Assumed Noise
0
5
10
15
20
25
30
Iteration Count

Figure 27

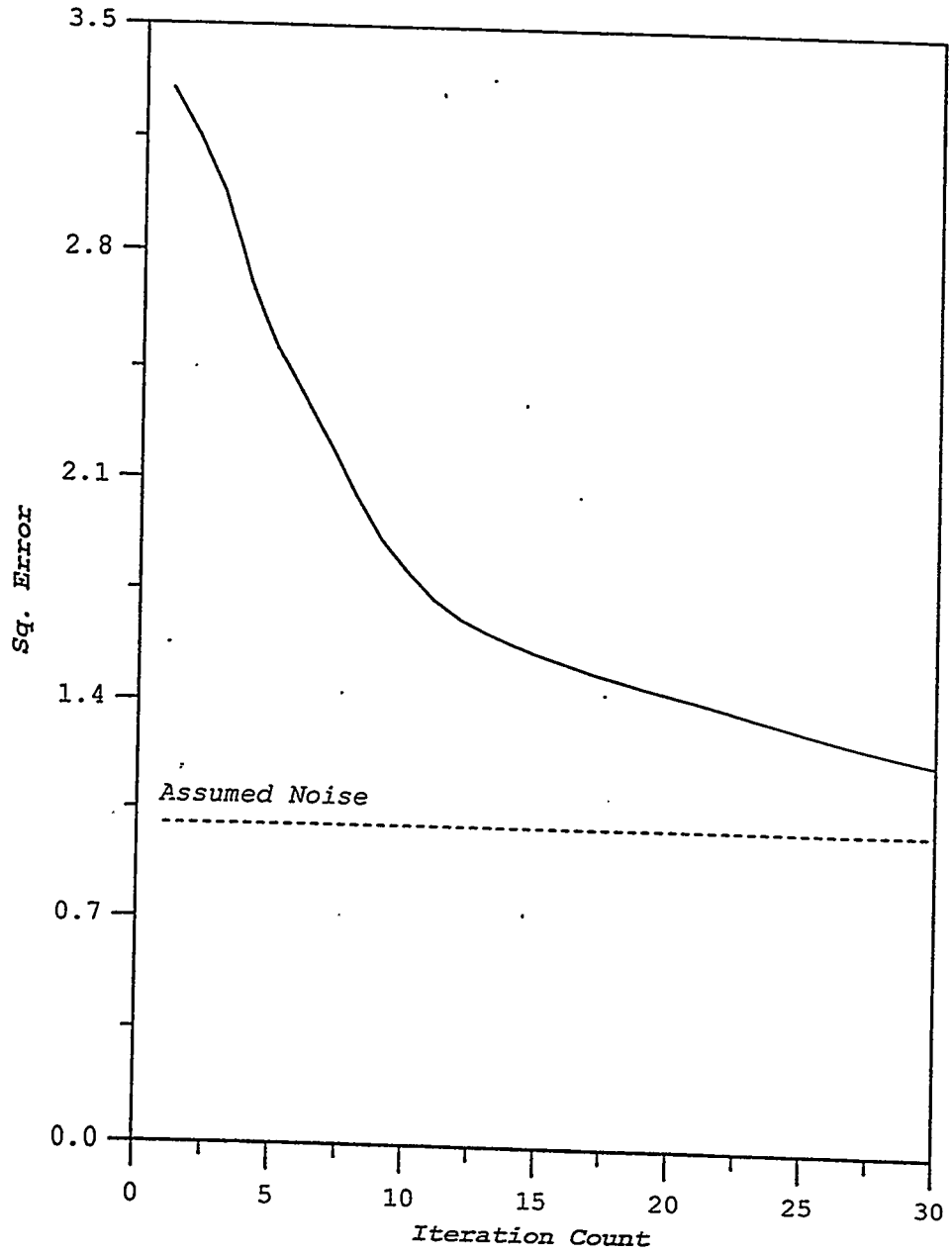
3.5
2.8
2.1
1.4
0.7
0.0
Sq. Error
Assumed Noise
0
5
10
15
20
25
30
Iteration Count

Figure 28

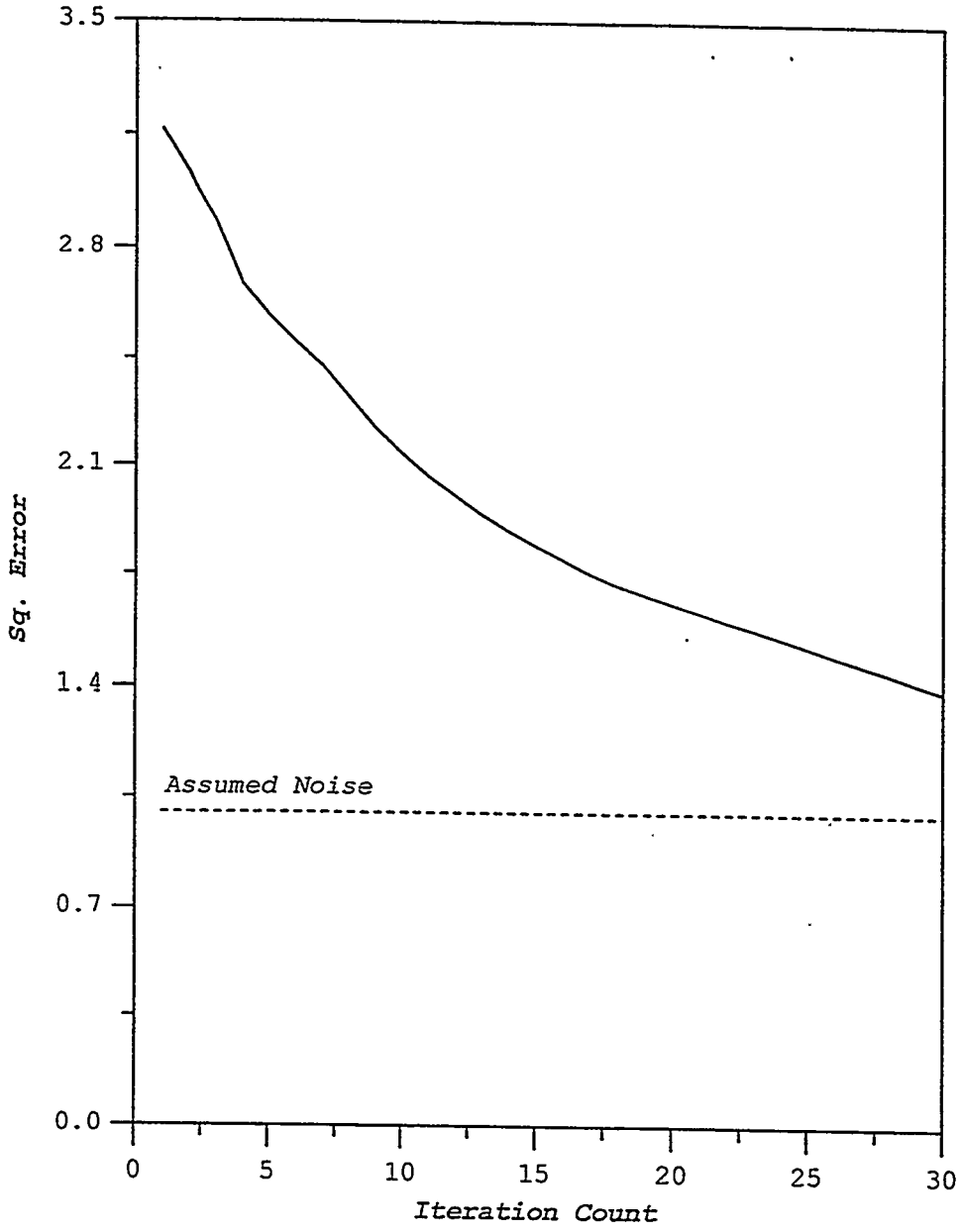
3.5
2.8
2.1
1.4
0.7
0.0
Sq. Error
Assumed Noise
0
5
10
15
20
25
30
Iteration Count

Figure 29

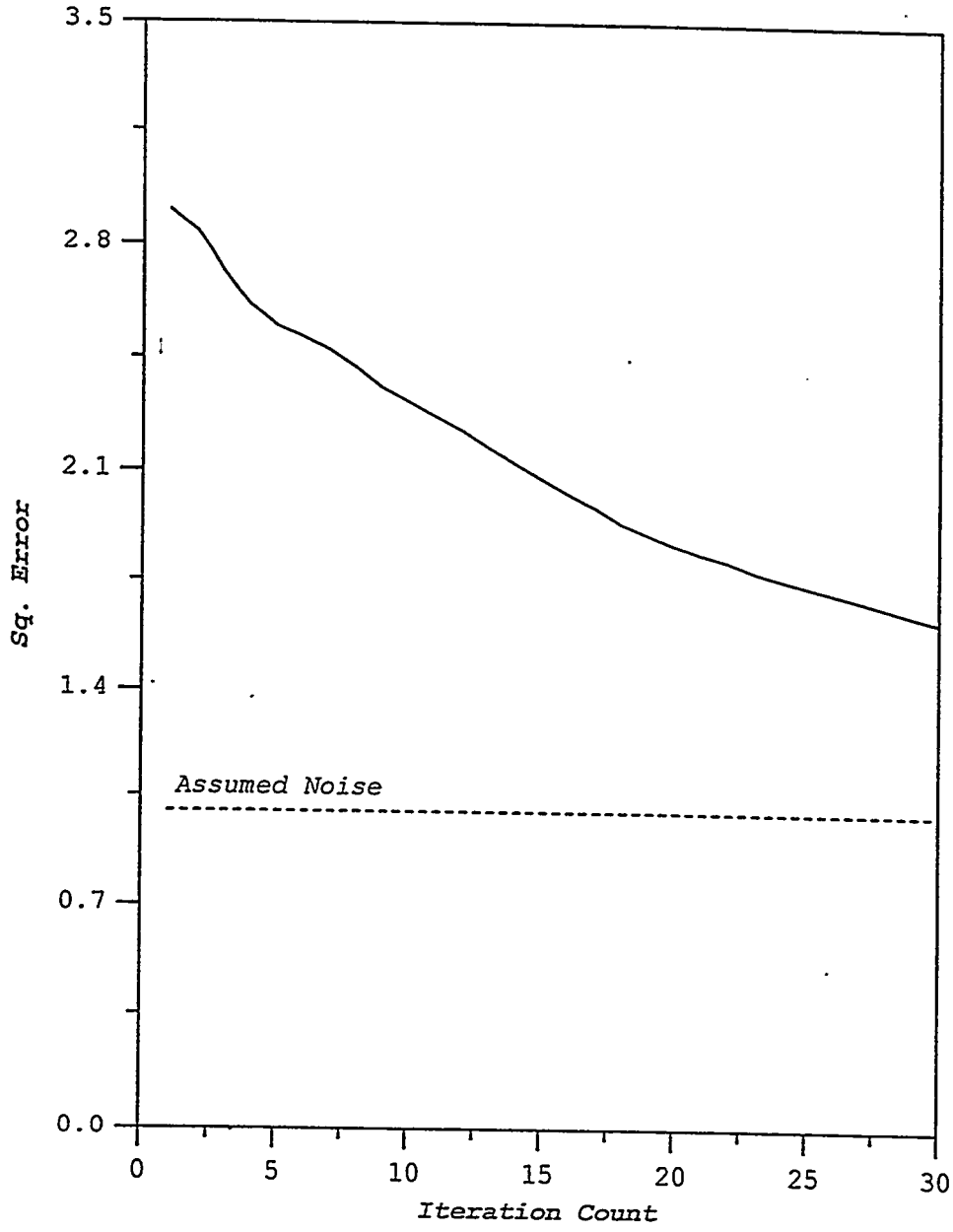
3.5
2.8
2.1
1.4
0.7
0.0
Sq. Error
Assumed Noise
0
5
10
15
20
25
30
Iteration Count

Figure 30

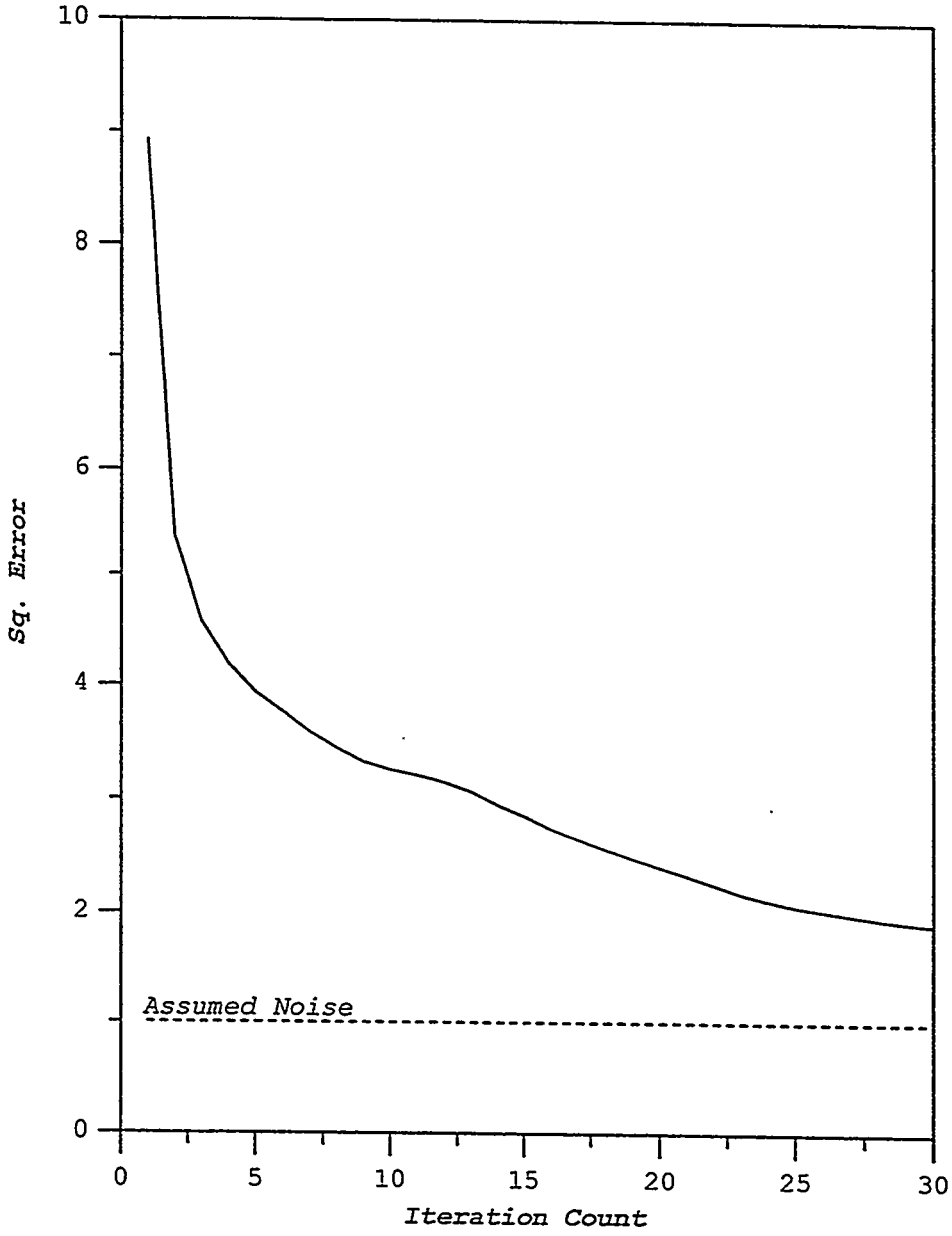
10
8
6
4
2
0
Sq. Error
Assumed Noise
0
5
10
15
20
25
30
Iteration Count

Figure 31

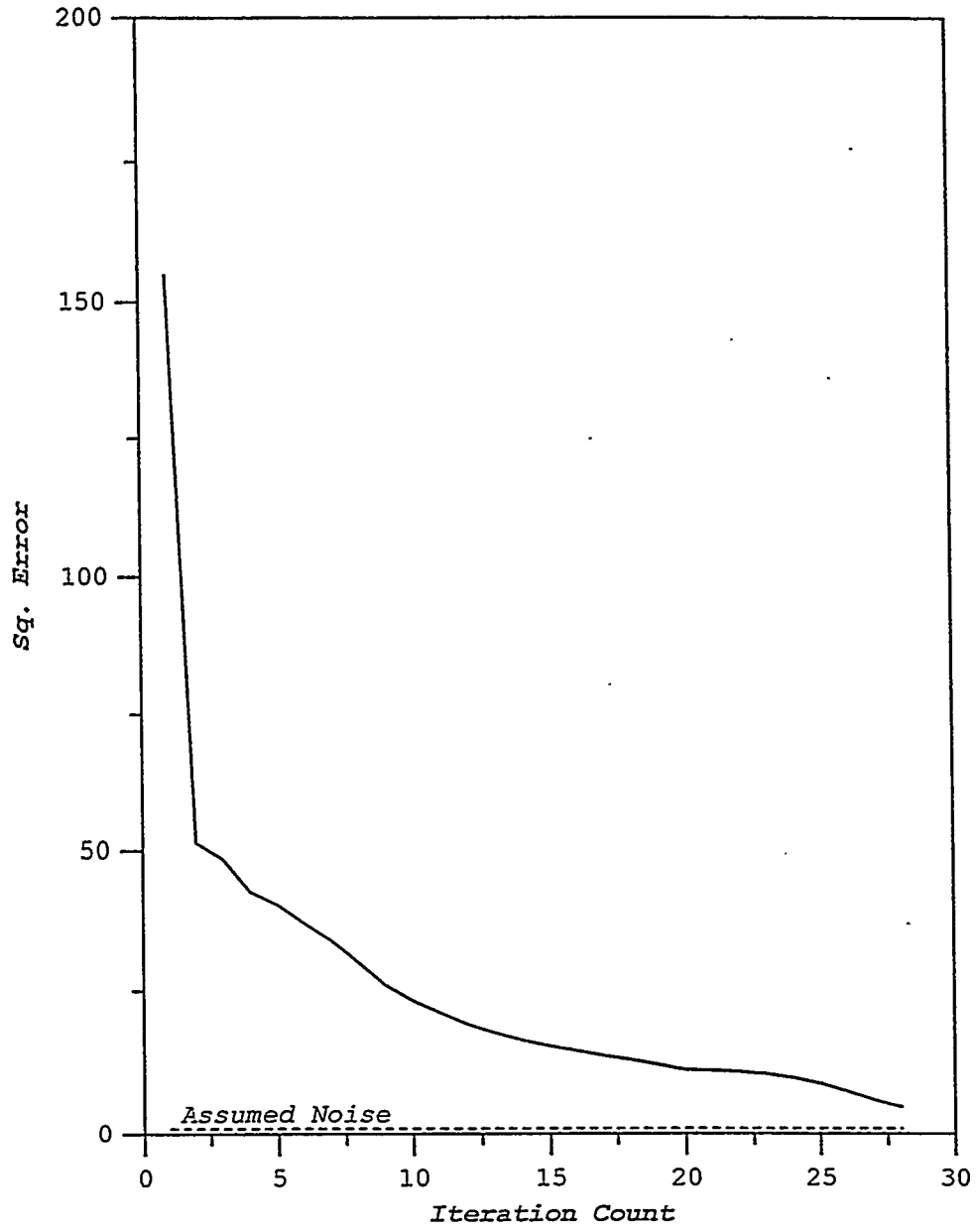
200
150
100
50
0
Sq. Error
Assumed Noise
0
5
10
15
20
25
30
Iteration Count

Figure 32

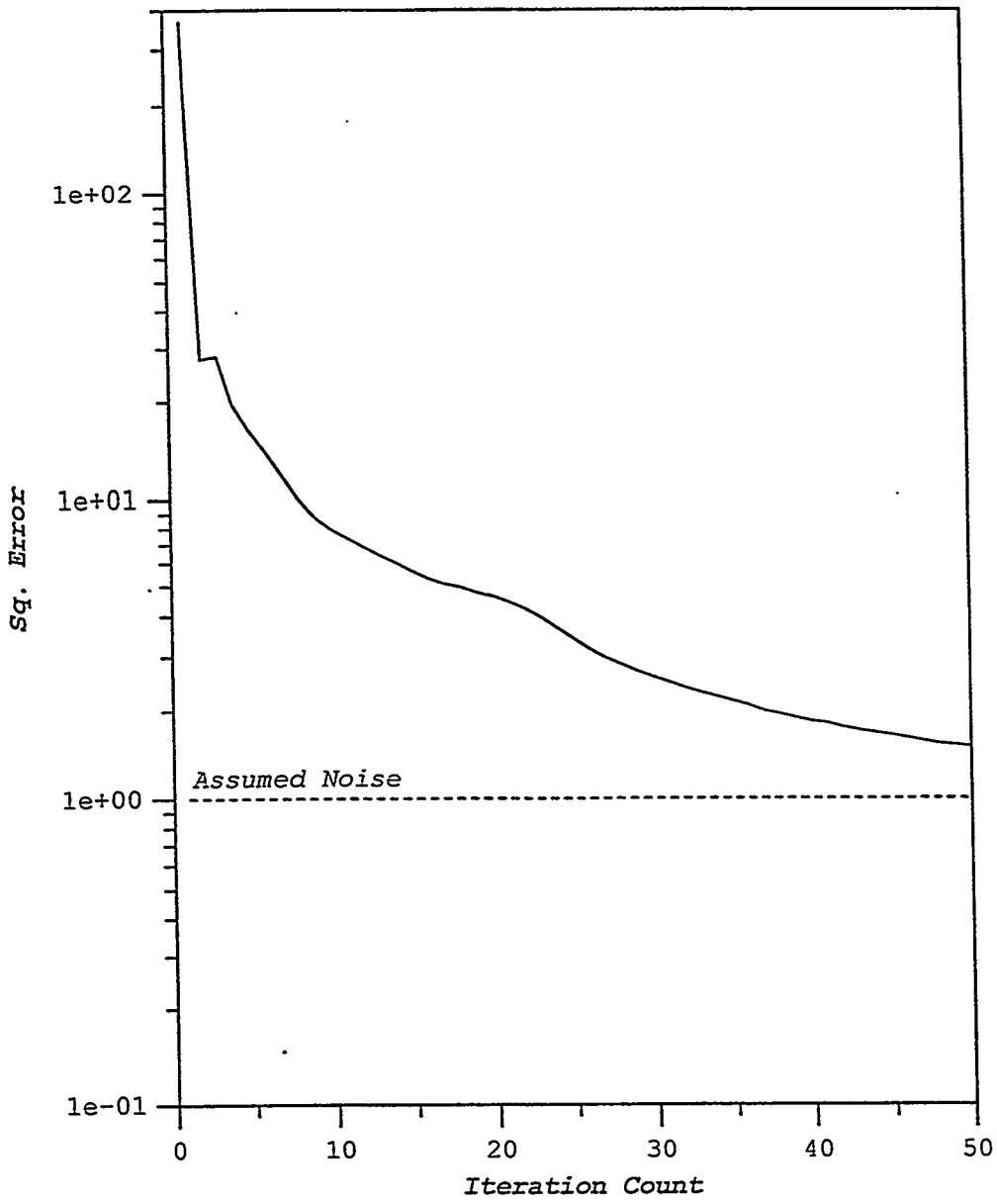
1e+02
1e+01
1e+00
1e-01
Sq. Error
Assumed Noise
0
10
20
30
40
50
Iteration Count

Figure 33

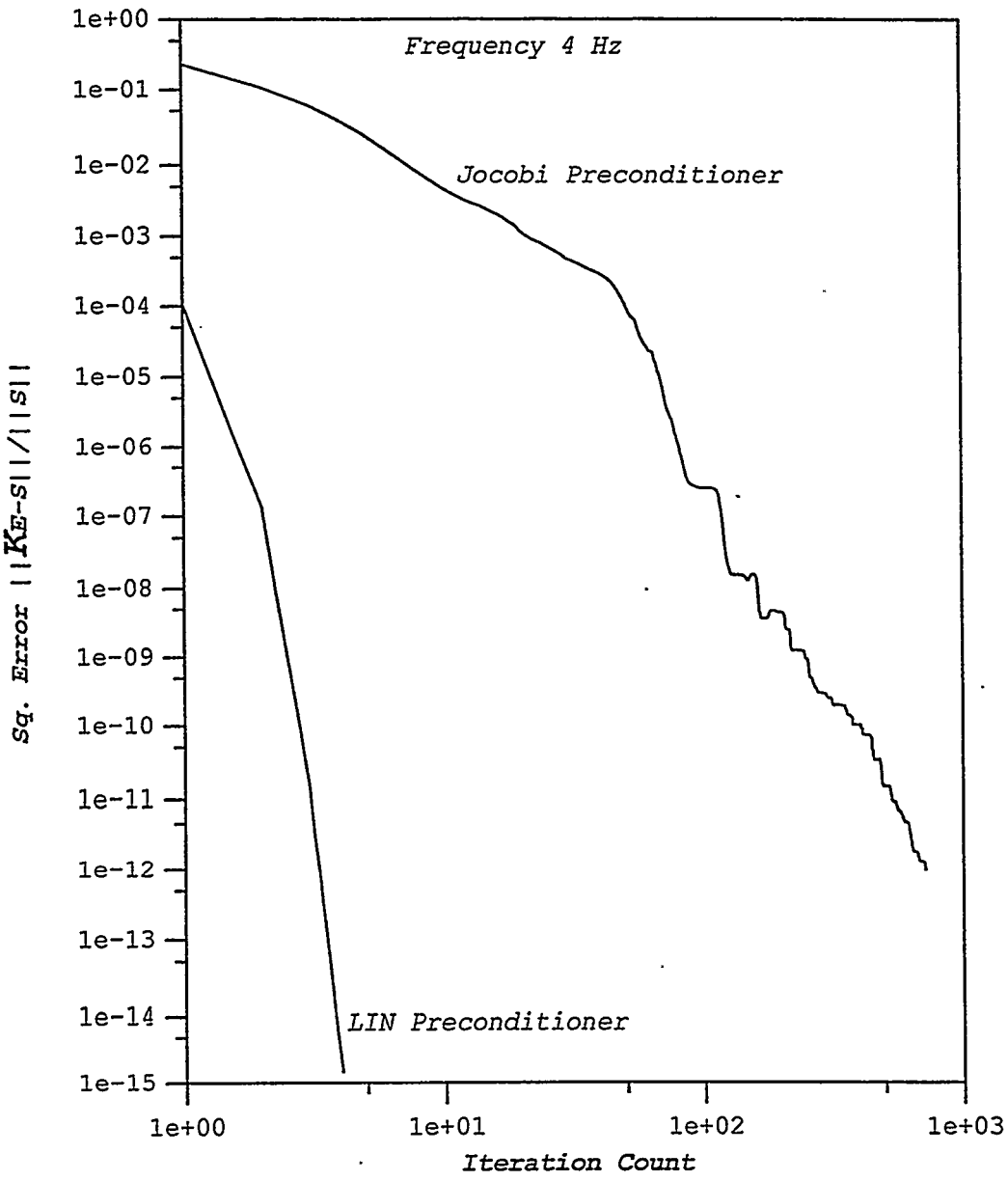
Frequency 4 Hz
Jocobi Preconditioner
LIN Preconditioner
Sq. Error ||K_E-S||/||S||
Iteration Count
1e+00
1e-01
1e-02
1e-03
1e-04
1e-05
1e-06
1e-07
1e-08
1e-09
1e-10
1e-11
1e-12
1e-13
1e-14
1e-15
1e+00
1e+01
1e+02
1e+03

Figure 34

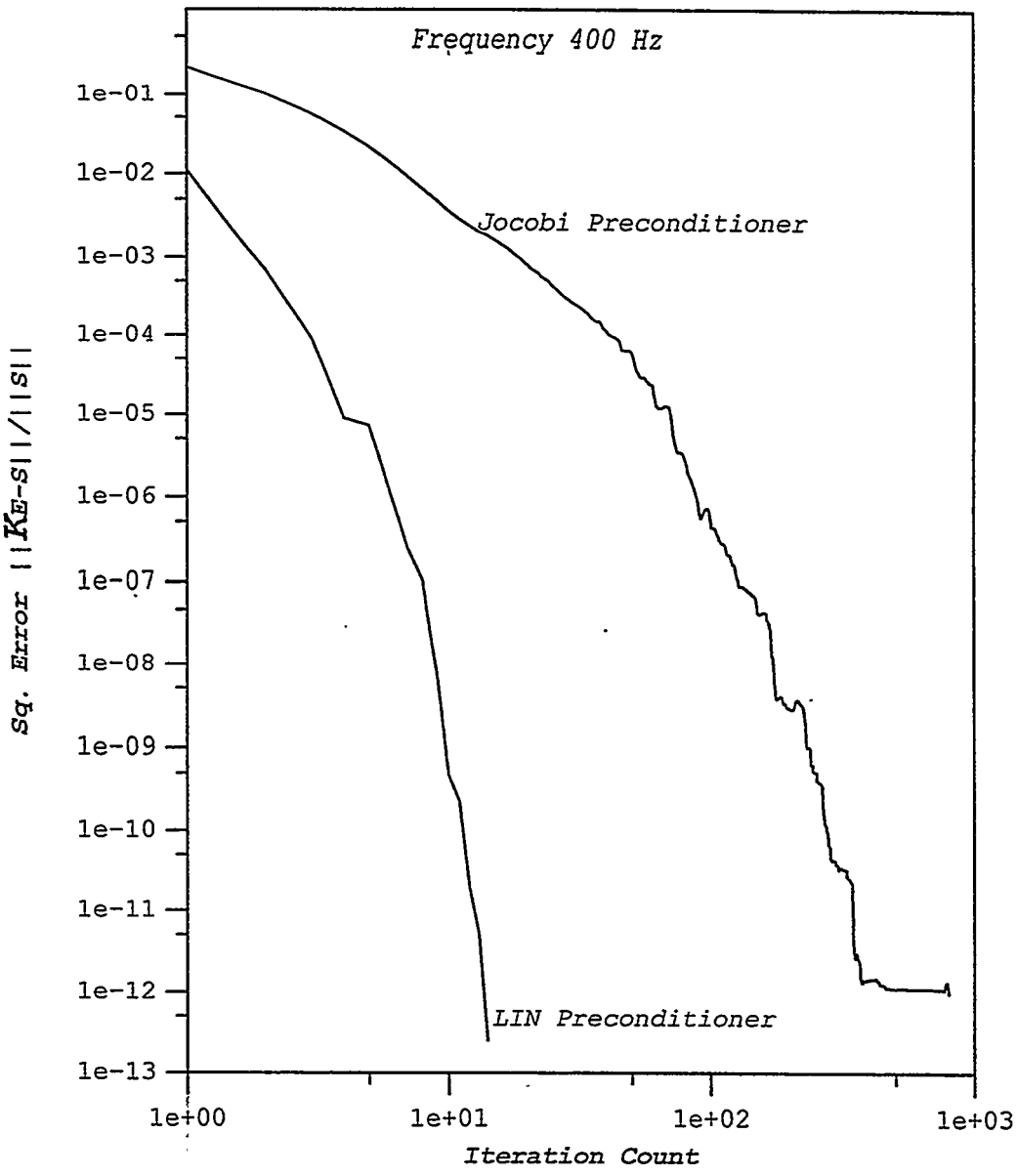
Frequency 400 Hz
Jocobi Preconditioner
LIN Preconditioner
Sq. Error ||KE-S||/||S||
1e-01
1e-02
1e-03
1e-04
1e-05
1e-06
1e-07
1e-08
1e-09
1e-10
1e-11
1e-12
1e-13
1e+00
1e+01
1e+02
1e+03
Iteration Count

Figure 35

Distribution

MS-0149	Chuck Meyers, 4000
MS-0701	Les Shephard, 6100
MS-0750	David Alumbaugh, 6116 David Aldridge, 6116 Greg Elbring, 6116 Gregory Newman, 6116 (5) Marianne Walck, 6116
MS-0859	Gerard Sleefe, 2693 Terry Stalker, 2693
MS-0151	Gerold Yonas, 9000
MS-1110	David Day, 9222 Louis Romero, 9222 David Womble, 9222
MS-1152	Mark Kiefer, 9542 Doug Riley, 9542
MS-9018	Central Technical Files, 8940-2
MS-0899	Technical Library, 4916 (2)
MS-0619	Review & Approval Desk, 15102
MS-0161	Patent & Licensing Office, 11500